
Wetting States of Droplets on Patterned Surfaces and in an Electric Field

Benetzungszustände von Tropfen auf gemusterten Oberflächen und im elektrischen Feld

Zur Erlangung des akademischen Grades Doktor-Ingenieur (Dr.-Ing.)

Genehmigte Dissertation von Maximilian Roland Hartmann aus Aschaffenburg

Tag der Einreichung: 13.10.2020, Tag der Prüfung: 08.12.2020

1. Gutachten: Prof. Dr. rer. nat. Steffen Hardt

2. Gutachten: Apl. Prof. Dr. Sc. Tatiana Gambaryan-Roisman

Darmstadt – D 17



TECHNISCHE
UNIVERSITÄT
DARMSTADT

Fachbereich Maschinenbau

Institut für Nano- und
Mikrofluidik

Prof. Dr. rer. nat. S. Hardt

Wetting States of Droplets on Patterned Surfaces and in an Electric Field
Benetzungszustände von Tropfen auf gemusterten Oberflächen und im elektrischen Feld

Accepted doctoral thesis by Maximilian Roland Hartmann

1. Review: Prof. Dr. rer. nat. Steffen Hardt
2. Review: Apl. Prof. Dr. Sc. Tatiana Gambaryan-Roisman

Date of submission: 13.10.2020

Date of thesis defense: 08.12.2020

Darmstadt – D 17

Bitte zitieren Sie dieses Dokument als:

URN: urn:nbn:de:tuda-tuprints-174209

URL: <http://tuprints.ulb.tu-darmstadt.de/17420>

Dieses Dokument wird bereitgestellt von tuprints,
E-Publishing-Service der TU Darmstadt
<http://tuprints.ulb.tu-darmstadt.de>
tuprints@ulb.tu-darmstadt.de



Die Veröffentlichung steht unter folgender Creative Commons Lizenz:

Namensnennung 4.0 International

<http://creativecommons.org/licenses/by/4.0/>

This work is licensed under a Creative Commons License:

Attribution 4.0 International

<https://creativecommons.org/licenses/by/4.0/>

Für meine Eltern

Helena und Andreas.

Acknowledgment

First of all, I would like to express my deep gratitude to my advisor Prof. Dr. rer. nat. Steffen Hardt. He provided me the opportunity to join the Institute for Nano- and Microfluidics (NMF) at the TU Darmstadt for doing my PhD. His guidance and deep understanding of the underlying physics, but also his support beyond the scientific work, have led me safely to the finalization of the present dissertation.

I am also very grateful for the close cooperation with my colleague Mathis Fricke. With his irrepressible curiosity and willingness to discuss, he helped me a lot with my promotion project. Furthermore I would like to thank Frank Plückebaum who is not only a great technician but also has a lot of skills as an experimenter. I also would like to express my gratitude to Dr. rer. nat. Tobias Baier and Dr.-Ing. Michael Eigenbrod for proofreading parts of the manuscript of the present dissertation and for scientific discussions. Moreover, I would also like to thank Dr.-Ing. Holger Marschall, who helped me to keep my head up during some more laborious times.

Referees for the Thesis I am very grateful to Prof. Dr. rer. nat. Steffen Hardt and Apl. Prof. Dr. Sc. Tatiana Gambaryan-Roisman for reviewing the present dissertation.

Colleagues within the NMF I would like to thank all my present and former colleagues of the Institute for Nano- and Microfluidics. Especially I would like to mention Dr. rer. nat. Tobias Baier, Assistant Prof. Dr. Aditya Bandopadhyay, Sebastian Dehe, Dr.-Ing. Michael Eigenbrod, Johannes Hartmann, Frank Plückebaum, Dr.-Ing. Tamal Roy, Maximilian Schür, Dr. rer. nat. Miklós Vécsei, and Dr. Sicheng Zhao who were not only colleagues but also good comrades.

Colleagues within the Collaborative Research Centre (CRC) 1194 Being part of the CRC 1194, I had the pleasure to work closely with Dr. rer. nat. Günter Auernhammer, Alena Bell, Prof. Dr. rer. nat. Dieter Bothe, Sebastian Brulin, Beatrice Fickel, Mathis Fricke, Felix Gerlach, Dr.-Ing. Dirk Gründing, Michael Heinz, Dr. Jonas Kind, and Mathias Zimmermann. I would also like to thank the organizers of the CRC 1194, Prof. Dr. Dieter Bothe, Dr.-Ing. Benjamin Lambie, Monika Medina Espana, and Prof. Dr.-Ing. Peter Stephan who put their effort in giving PhD students the opportunity to work in an interdisciplinary environment.

(Former) Students Besides the scientific and technical staff, I want to thank Cora Despot, Marcel Neu, and Lukas Weimar who also contributed in the succeed of the present dissertation.

Funding I kindly acknowledge the financial support by the German Research Foundation (DFG) within the Collaborative Research Centre 1194 "Interaction of Transport and Wetting Processes", subproject A02b.

Danksagung

Mein tiefer Dank gilt meinen Eltern Helena und Andreas, die mich in all meinem Tun unterstützt haben. Ich bin der festen Überzeugung, dass erst durch ihre bedingungslose Hilfe und Förderung sich mir die Möglichkeit eröffnet hat, eine Universität besuchen zu können. Auch die Unterstützung darüber hinaus hat dazu geführt, dass ich mich ohne Ablenkung auf das Studium und dessen erfolgreichen Abschluss fokussieren konnte und sich mir erst hierdurch die Möglichkeit einer Promotion eröffnet hat. Ich weiß, dass das nicht selbstverständlich ist, und dies vor allen Dingen durch ihr Zutun ermöglicht wurde.

Zuletzt möchte ich von ganzem Herzen meiner Verlobten Anna-Maria für all ihren Zuspruch und ihre Geduld danken. Sie zeigt mir, ohne es zu beabsichtigen, das wirklich Wesentliche auf, wodurch sich das Verfassen einer Dissertation mit einer gewissen Leichtigkeit ertragen lässt.

Zusammenfassung

Die Benetzung gemusterter Oberflächen durch Tropfen ist in der Natur allgegenwärtig. Beispielsweise wird sie vom Stenocara Wüstenkäfer in der Namib Wüste genutzt, um Feuchtigkeit aus der Luft zu sammeln. Aber auch in Ingenieur Anwendungen wie der Wassergewinnung, oder dem Tintenstrahldruck spielt sie eine wichtige Rolle. Des Weiteren ist der Transport von Tropfen über Substrate durch das Aufbringen von Benetzungsmustern möglich. Dieser kann auch mittels elektrostatischer Felder realisiert werden. Hierbei können Fluidstrukturen auftreten, die beispielsweise beim Elektrosponnen relevant sind.

In der vorliegenden Arbeit wird zunächst die Stabilität von Wassertropfen auf chemisch strukturierten Oberflächen, die aus abwechselnden hydrophilen und hydrophoben Streifen bestehen, experimentell, numerisch und basierend auf einem Skalierungsmodell untersucht. Die Grenze zwischen den Kontaktwinkelkontrasten, also der Differenz der Kontaktwinkel zwischen den hydrophilen und den hydrophoben Streifen, bei denen die Tropfen intakt (stabil) bleiben, und denen, die zum Aufbrechen der Tropfen führen (instabil), wird mit Surface Evolver, einem numerischen Tool zur Minimierung der Oberflächenenergie, berechnet. Die so ermittelte Stabilitätsgrenze zwischen instabilem und stabilem Regime wird experimentell bestätigt. Innerhalb des instabilen Regimes wird eine Tropfenform identifiziert, bei der eine Kapillarbrücke auf dem hydrophoben Streifen zwei auf den angrenzenden hydrophilen Streifen befindlichen Flüssigkeitsfinger verbindet. Bei durch Verdunstung abnehmendem Volumen nimmt die Breite dieser Kapillarbrücke ab, bis sie einen kritischen Wert erreicht, bei dem die Brücke instabil wird. Es wird ein einfaches Skalierungsmodell präsentiert, mit dem die kritische Breite vorhergesagt werden kann. Gemäß dem Modell wird ein Tropfen instabil, wenn der zunehmende Laplace-Druck innerhalb der Brücke nicht mehr durch den Druck innerhalb der Flüssigkeitsfinger auf den hydrophilen Streifen ausgeglichen werden kann. Dies wird durch einen Vergleich mit Experimenten und numerischen Berechnungen verifiziert.

Die Dynamik des im instabilen Bereich auf dem hydrophoben Streifen beobachteten Aufbruchs der Kapillarbrücke wird experimentell und numerisch untersucht. Durch Betrachten der Aufbruchgeschwindigkeit über der zugehörigen minimalen Kapillarbrückenbreite kann die Unsicherheit durch die Wahl des exakten Aufbruchzeitpunktes eliminiert werden. Die Simulation basiert auf der Volume-of-Fluid (VOF) Methode. Eine physikalisch realistische Anfangsbedingung für die VOF-Simulation wird mit Surface Evolver berechnet. Es zeigt sich, dass der Aufbruch der Kapillarbrücke nicht durch ein eindeutiges Skalierungsgesetz charakterisiert werden kann. Die Form der Brücke unterliegt qualitativen Änderungen und in verschiedenen Phasen des Aufbruchprozesses finden sich unterschiedliche Skalierungsexponenten. In der letzten Phase des Aufbruchs bildet die Kapillarbrücke einen flüssigen Faden, dessen Aufbruch mit der Rayleigh-Plateau Instabilität konsistent ist.

Experimentelle Untersuchungen zu Surface Taylor Cones (STCs) auf hydrophilen Substraten mit niedriger Kontaktwinkelhysterese werden präsentiert. STCs sind Strukturen analog zu klassischen Taylor-Cones, die sich entwickeln, wenn ein Bereich einer Flüssigkeitsoberfläche einem starken elektrischen Feld ausgesetzt wird. Im vorliegenden Fall befindet sich dieser an der Dreiphasenkontaktklinie. Die durch das elektrische Feld

resultierende Kraft ist parallel zur Oberfläche gerichtet. Im Vergleich zum Tropfen ohne elektischem Feld ist der Kontaktwinkel aufgrund der Maxwell Spannung zu Beginn des Experiments verringert, während die Tropfenform an sich unberührt erscheint. Im weiteren Verlauf bildet sich unter fortschreitender Abnahme des Kontaktwinkels eine Flüssigkeitszunge, die sich zu einer kegelförmigen Struktur mit zunehmend ausgeprägter Spitze entwickelt. Schließlich bricht die Flüssigkeitsoberfläche zusammen und es tritt von der Spitze des Kegels ein Jet aus, der auf die Elektrode gerichtet ist. Dieser Vorgang findet nur auf hydrophilen Substraten mit geringer Kontaktwinkelhysterese statt. Der STC wird charakterisiert und mit dem Taylor-Cone, sowie einer dem STC ähnlichen Tropfenform verglichen, die auf der entnetzenden Seite gleitender Tropfen auf einer schiefen Ebene beobachtet werden kann.

Abstract

In nature, wetting of patterned surfaces by droplets is omnipresent. For example, it is used by the *Stenocara* desert beetle in the Namibian desert to collect moisture from the air. However, it also plays a vital role in engineering applications such as water harvesting or inkjet printing. Furthermore, the transport of droplets over substrates is possible by chemically modifying its surface to create a wetting pattern. The movement of sessile droplets can also be achieved by the application of an electrostatic field. In this case, fluid structures can occur, which are relevant, for instance, in electrospinning.

In a first instance, the stability of water droplets on chemically patterned surfaces consisting of alternating hydrophilic and hydrophobic stripes is studied experimentally, numerically, and based on a scaling model. The boundary between the contact angle contrasts, leaving the droplets intact (stable) and those leading to droplet breakup (unstable), is computed numerically with the Surface Evolver, which is a numerical tool that minimizes the surface energy. The existence of a stable and unstable regime found with numerics is confirmed experimentally. In the unstable regime, when approaching droplet breakup, an H-shaped configuration with two liquid fingers on the hydrophilic stripes connected by a capillary bridge spanning the hydrophobic stripe is found. For decreasing volumes, the width of this capillary bridge decreases until a critical value is reached at which the droplet breaks up. A simple scaling model is presented, which predicts the critical bridge width. According to the model, the droplet becomes unstable when the increasing Laplace pressure inside the bridge can no longer be balanced by the pressure inside the liquid fingers on the hydrophilic stripes. The model is verified by the experiments and the Surface Evolver simulations.

The breakup dynamics of the capillary bridge observed on the hydrophobic stripe in the unstable regime is studied experimentally and numerically. By considering the breakup speed as a function of the minimum capillary bridge width, the breakup dynamics can be evaluated without the uncertainty in determining the precise breakup time. The simulations are based on the Volume-of-Fluid (VOF) method. In order to construct physically realistic initial data for the VOF-simulation, Surface Evolver is employed to calculate an initial configuration consistent with experiments. It is found that the breakup of the capillary bridge cannot be characterized by a unique scaling relation. Instead, different scaling exponents are found at different stages of the breakup process, accompanied by qualitative changes in the shape of the bridge. In the final stage of the breakup, the capillary bridge forms a liquid thread that breaks up consistently with the Rayleigh-Plateau instability.

Surface Taylor Cones (STCs) on hydrophilic substrates with low contact angle hysteresis are reported and investigated experimentally. STCs are structures analogous to the classical Taylor-Cones developing when a region of a liquid surface gets exposed to a strong electric field. In the present case, this region is located at the three-phase contact line, and the resulting force originating from the electric field is directed parallel to the surface. Initially, due to the Maxwell tension, only the contact angle is reduced compared to the drop without the electric field, while the drop shape itself appears to be not influenced. Subsequently, a liquid tongue is formed, which develops into a conical structure with an increasingly prominent tip, while the

contact angle progressively decreases during this process. Finally, the liquid surface breaks down, and a jet emerges from the liquid cone tip that is in contact with the substrate and directed towards the electrode. It is found that the STCs can only develop on hydrophilic, low contact angle hysteresis substrates. The STC is characterized and compared to the original Taylor-Cone and a similar shape that can be observed at the receding side of droplets sliding down an inclined surface.

Contents

1	Introduction	1
2	Theory - Capillarity and Wetting	5
2.1	Capillarity	5
2.1.1	Gibbs Dividing Surface and the Definition of the Surface Tension	5
2.1.2	Minimal Surfaces and some Examples	7
2.2	Wetting	9
2.2.1	The Contact Angle, Young's Equation, and its Application to Energy Minimization	9
2.2.2	Contact Angle Hysteresis	11
2.3	Influence of External Forces	12
2.3.1	Influence of Gravity: Bond Number and Capillary Rise Height	12
2.3.2	Influence of Electrostatic Forces: Maxwell-Tension and Taylor-Cone	14
3	Global Methods	17
3.1	Experimental Setup	17
3.1.1	Humidification	18
3.1.2	Droplet Dosing	20
3.1.3	Some Consequences from Optics	21
3.1.4	Alternate Experimental Setups	22
3.2	Data Evaluation	23
3.2.1	Used Software Tools	23
3.2.2	General Steps in Image Processing	23
3.2.3	Edge detection	24
3.3	Numerical Setup - The Surface Evolver	25
3.3.1	General Overview and Functionality	25
3.3.2	An Automatic Routine	26
4	Surface Modification Techniques	29
4.1	Introduction	29
4.2	Chemically Patterned Substrates	30
4.2.1	Photolithography	30
4.2.2	Silanization	32
4.2.3	Used Material and Substrate Preparation	37
4.2.4	Characterization	38
4.3	Hydrophilic Substrates with Low Contact Angle Hysteresis	41
4.3.1	Used Material and Substrate Preparation	42
4.3.2	Characterization	43

5	Stability of Droplets on Chemically Patterned Surfaces	45
5.1	Introduction	45
5.2	Experimental Procedure and Data Evaluation	48
5.2.1	Experiments	48
5.2.2	Evaluation of Primary Data	48
5.2.3	Code Validation	49
5.3	Numerical Procedure	51
5.3.1	Model and Geometry	51
5.3.2	Parameters and Algorithm	52
5.3.3	On the No-Breakup Criterion	54
5.4	Results and Discussion	54
5.4.1	Critical Contact Angle Contrast	56
5.4.2	Critical Bridge Width	57
5.5	Summary and Conclusion	64
6	Breakup Behavior of Droplets on Chemically Patterned Surfaces	65
6.1	Introduction and Literature	65
6.2	Experimental Details and Data Evaluation	67
6.2.1	Experiments	67
6.2.2	Data Evaluation	68
6.3	Numerical Methods	69
6.4	Results	71
6.4.1	Breakup Dynamics	72
6.4.2	Rayleigh-Plateau Instability	74
6.5	Summary and Conclusion	77
7	Surface Taylor-Cones	79
7.1	Introduction	79
7.2	Methods	81
7.2.1	Samples and Setup	81
7.2.2	Experimental Procedure	83
7.2.3	Data Evaluation	83
7.3	Results and Characterization	84
7.3.1	Opening Angles	86
7.3.2	Contact Angles	87
7.3.3	Tip Radius	88
7.4	Conclusion and Outlook	91
8	Concluding Remarks	93

List of Figures

2.1	The dividing surface in the Gibbs model.	6
2.2	Sketch to derive the Laplace pressure.	8
2.3	Sketch for the derivation of Young's equation.	10
2.4	The contact angle hysteresis.	11
2.5	The capillary rise height.	13
3.1	Overview of the central experimental setup.	18
3.2	Humidification of the atmosphere inside the climate chamber	19
3.3	Sketch of the droplet dosing unit.	20
3.4	Visual description of the main steps of image detection.	24
4.1	Sketch of photolithography steps when using a positive photoresist.	31
4.2	General chemical structure of perfluorinated trichlorosilanes.	32
4.3	Sketch of the chemical reactions which lead to the silane monolayer on hydrolyzed substrates.	33
4.4	Schematics of the CVD-chamber.	36
4.5	Dimensionless width from different parameters α and w_{phil}	38
4.6	Contact angle and dimensionless diameter of evaporating water droplets on three different surfaces PFDTs, TFPTS and glass as a function of the dimensionless evaporation time.	40
4.7	Measured water contact angles versus contact angles from Kaneko et al.	43
5.1	Breakup of an evaporating water droplet on a chemically patterned striped surface with a hydrophilic stripe width of 25 μm and $\alpha = 0.5$	46
5.2	Overview of the stability problem.	47
5.3	Structogram of the image evaluation algorithm.	49
5.4	Comparison between the simulated breakup of a capillary bridge, and the evaluated images from the image data originating from simulations.	50
5.5	Initial and final geometries for two different configurations of the Surface Evolver model.	51
5.6	Overall Surface Evolver algorithm.	53
5.7	Validation of the no-breakup criterion.	54
5.8	Water droplets on a striped surface at different stages of evaporation.	55
5.9	Phase diagram of the stability of droplets wetting three stripes, one hydrophobic one between two hydrophilic ones.	56
5.10	Influence of the hydrophilic stripe width on the breakup behavior for different values of α	58
5.11	Shape of a droplet as it is assumed in the model, together with relevant model parameters.	59
5.12	Dimensionless curvature of the capillary bridge perpendicular to the stripe orientation.	60
5.13	Inverse widths of the liquid bridge as a measure for the pressure obtained from the model.	62
5.14	Comparison of the critical bridge width obtained from the model with Surface Evolver calculations and the experiments.	63

6.1	Illustration for the choice of breakup time for $w_{\text{phil}} = 500 \mu\text{m}$ and $\alpha = 1$	68
6.2	Qualitative comparison between experiment and simulation for $w_{\text{phil}} = 500 \mu\text{m}$ and $\alpha = 1$	71
6.3	Breakup behavior of the capillary bridge for $\alpha = 1$	72
6.4	Image sequence corresponding to the last eight experimental data points in figure 6.3(a).	73
6.5	Breakup behavior of the capillary bridge for $\alpha = 0.5$	74
6.6	Breakup behavior of the capillary bridge for $\alpha = 1.5$	75
6.7	Qualitative analysis of the final breakup behavior of the capillary bridge.	75
6.8	Quantitative analysis of the final breakup behavior.	76
7.1	Droplets merging at the three-phase contact line and droplet "Ping-Pong".	80
7.2	Schematics of the experimental setup.	82
7.3	To the droplet shape fitted hyperbola and the resulting tip radius in the moment the surface Taylor-Cone has formed.	84
7.4	Typical evolution of the liquid surface in an electric field on a low contact angle hysteresis substrate.	85
7.5	Typical evolution of the liquid surface in an electric field on an uncoated glass surface.	85
7.6	Opening angles β of the STC as a function of the distance b_0 between the tip of the cone and the electrode.	86
7.7	Contact angle Θ_{STC} at the moment of the appearance of the STC over the initially measured contact angle Θ_{init}	87
7.8	Evaluation of the tip radius of the STC.	88
7.9	Comparison of the experimental data to the model of Peters et al. [143] and the offset model.	90

List of Tables

3.1	Important properties of the used cameras.	21
3.2	Optical properties of the available objective combinations for minimum (low) and maximum (high) magnification	22
4.1	Comparison of three different silanization techniques.	34
4.2	Process parameters for two different silanes.	37
4.3	Advancing and receding contact angles of DI-water droplets on used surfaces.	41
5.1	Parameters used in the model.	61
6.1	Contact angles and wetted length on the hydrophilic stripe as observed in the experiments and used in the Surface Evolver calculations.	70
7.1	Fitting parameters from the model by Peters et al., an extended one (offset model), and their reference values.	90

List of Symbols

Latin	Symbols	
<i>a</i>	distance between electrode and fluid outlet	m
<i>A</i>	area	m ²
<i>b</i>	distance between contact line and reference point	m
<i>B</i>	Binning	-
<i>Bo</i>	Bond number	-
<i>c</i>	concentration	kg m ⁻³
<i>C</i>	constant in scaling relations	-
<i>Ca</i>	Capillary Number	-
<i>d</i>	minimum bridge width	m
<i>D</i>	dimensionless minimum bridge width	-
<i>D</i>	diffusion coefficient	m ² s ⁻¹
<i>e</i>	mesh size	m
<i>E</i>	electric field	V m ⁻¹
<i>f</i>	frequency	s ⁻¹
<i>F</i>	force	N
<i>ℱ</i>	Helmholtz free energy	J
<i>g</i>	gravity	m s ⁻²
<i>G</i>	Gibb's free energy	J
<i>h</i>	height	m
<i>H</i>	length scale / humidity	m / %rh
<i>k</i>	form factor	-
<i>K</i>	dimensionless curvature	-
<i>l</i>	length	m
<i>L</i>	length scale	m
<i>M</i>	magnification	-
<i>n</i>	amount of substance	mol
<i>N</i>	number of stripes	-
<i>NA</i>	numerical aperture	-
<i>o</i>	offset parameter	m ⁻¹
<i>Oh</i>	Ohnsorg Number	-
<i>p</i>	pressure	N m ⁻³
<i>q</i>	charge	C
<i>r</i>	radius of curvature	m
<i>R</i>	radius / radial length scale	m
<i>s</i>	unit-length	m
<i>S</i>	entropy	J K ⁻¹
<i>t</i>	time	s

T	temperature / dimensionless time	K, °C / -
\mathcal{T}	Maxwell stress tensor	N m^{-2}
u	velocity	m s^{-1}
U	Voltage	V
\mathcal{U}	inner energy	J
v	pixel value	-
V	volume	m^3
w	stripe width	m
Greek Symbols		
α	stripe width ratio	-
β	opening angle	°
γ	exponential factor	-
Δi	difference between two i	unit of i
ϵ	electirc permittivity	$\text{C V}^{-1} \text{m}^{-1}$
η	dynamic viscosity	Pa s
Θ	contact angle	°
κ	curvature	m^{-1}
λ	wavelength	m
μ	chemical potential	J mol^{-1}
ν	scaling coefficient	-
ξ	optical resolution	m
ρ	density	kg m^{-3}
σ	surface tension	N m^{-1}
τ	(capillary) time scale	s
v	relative error	rel%
ψ	fraction of liquid in cell	-
χ	direction Bildverarbeitung	-
ω	angular velocity	$^{\circ} \text{s}^{-1}$

Indices

adv	advancing
air	air
at	lens attachment
c	capillary
cell	cell
con	contrast
conv	convergence
crit	critical
C	cylinder
D	droplet
dof	depth of field
el	electrostatic / electrical
eq	equilibrium
evap	evaporation
f	film
hd	hydrodynamic
H ₂ O	water
in	in
initi	initial
l	liquid
LA	lateral adhesion
lg	liquid-gas
mac	macroscopic
max	maximum
mic	microscopic
min	minimum
mount	mounting
os	offset
out	out
PDFTS	PDFTS (see abbreviations)
phil	hydrophilic
phob	hydrophobic
pic	picture
px	pixel
react	reaction
rec	receding
sg	solid-gas
silane	silane
sl	solid-liquid
sphere	sphere
start	start
STC	Surface Taylor-Cone
target	target
thread	thread
thresh	threshold
tot	total

w	working
	parallel
⊥	perpendicular
*	timepoint after pinch-off
0	reference

Abbreviations

AP	atmospheric pressure
B	bubbler
CAS	Chemical Abstracts Service
CCA	constant contact angle
CCR	constant contact radius
CFD	Computational Fluid Dynamics
CRC	Collaborative Research Centre
CVD	chemical vapor deposition
DENIISE	Droplet Evolution: Impact, Spreading, Evaporation
DI	de-ionized
FC	flow controller
FEP	Perfluor(ethylen-propylen)
fps	frames per second
FS3D	Free Surface 3D
LP	low pressure
PDMS	Polydimethylsiloxane
PEG-M	2-[Methoxy(ethyleneoxy)10 propyl]trimethoxysilane, Dynasylan 4148
PFDTs	1H,1H,2H,2H-Perfluorodecyltrichlorosilane
PTFE	Polytetrafluoroethylen
rh	relative humidity
ROI	Region of Interest
Rx	reaction
SE	Surface Evolver
SLIPS	slippery lubricant-infused surfaces
SMCI	Surface-Cell Mesh Intersection
STC	Surface Taylor-Cone
stl	standard triangulated language
TIRF	total internal reflection
TEOS	Tetraethoxysilane
TFPTS	(3,3,3-Trifluoropropyl)trichlorosilane
V	valve
VOF	Volume-of-Fluid

1 Introduction

The present lines would never have been written if humankind had not always felt obliged and the need to preserve knowledge and pass it on to future generations, who again used this knowledge as a foundation to build on. Since about 5000 years the pre-dominant way of archiving this information is based on the transfer of a fluid from a reservoir to a solid underground. The demonstrably first to use this process were the Egyptians, who, around 3000 BC, used a chiseled reed pen to transfer some ink onto papyrus [1]. Over the following few thousand years, this technique stayed the same. Of course, the reed pen eventually was substituted by a feather shaft, the papyrus by some paper, and the ink might have been improved over the millennia. Nevertheless, the actual process with its underlying physics did not change: The tip of a capillary, let us call it pen for simplicity, is dipped into an ink reservoir. Then, capillary forces originating from the liquid and the material of the pen lead to the rise of ink inside of the latter. When lifting the pen out of the ink bath, it is held inside the capillary due to lateral adhesion forces originating from contact angle hysteresis, until the pen tip touches the medium on which the written information is intended to be stored. Preferably, this is a hydrophilic, porous solid, like papyrus, or paper, among others. What happens then depends on the person who holds the pen in his hand. Although the process of writing is thousands of years old, it seems that the first ones who systematically investigated the hydrodynamics of writing were Kim et al. in 2011 [2]. Ink is transferred from the capillary towards the solid due to the hydrophilic and porous nature of the substrate. The thickness of the drawn line depends on the speed of the pen, with which it is led above the substrate. The ink is held inside of the porous substrate by capillary forces until it has dried. When an author has finished writing his thoughts onto the substrate, he or she lifts the pen, eventually leading to a small blob that can be investigated at the position where the pen touched the solid last. This blob has its origin from a capillary bridge formed by the ink between the tip of the pen, and the solid that breaks up after it is lifted sufficiently high. Even today, pupils learn writing by using fountain pens that follow the same principle as the Egyptians exploited 5000 years ago, though the ink reservoir is part of the writing system and clipped at one end of the capillary.

In Europe, the writing, as described above, was the main duplication method of information until Johannes Gensfleisch zum Gutenberg developed the first printing press around 1450 AD in Mainz, Germany, which was the first movable type printing system. However, Gutenberg was not the *inventor* of this particular printing process, i.e., the block-printing itself. The first woodblock-printed book, which is still preserved for posterity, is dated from 868 AD and was printed in China. What Gutenberg's development made superior over other printing technologies were his inventions of replica-casting, with which he accomplished to produce any number of an exact copy of any letter in the inverse, from which a matrix could be created, and ink that adhered well to metal (all information are taken from [1], pp. 265 - 272). Nevertheless, the underlying physics of fluid transfer in the case of the printing press and more modern printing technologies is based on capillarity and wetting principles. While the printing press is primarily used to produce replicas of the written word on paper, other techniques can also be used to produce devices repeatably, e.g., printed electronics [3]. Today's common printing techniques based on fluid transfer can be summarized in five different categories [4]: Relief printing, intaglio printing, lithographic and electrophotographic printing,

screen or stencil printing, and inkjet printing. While in relief printing, the fluid transfer is accomplished from raised regions covered with ink (similar to Gutenberg's printing press), in intaglio printing, ink is transmitted onto substrates (or an intermediate surface) from cavities. In lithographic and electrophotographic printing, oil-based ink is printed from pre-patterned hydrophobic regions, while hydrophilic areas are covered with an aqueous solution preventing the ink from wetting also these regions. Screen or stencil printing uses meshes or holes through which the ink is squeezed onto the substrate, and in inkjet printing, ink is jetted from a nozzle as small droplets onto a surface. Of course, this list covers not the entire range of printing technologies. However, in addition to the above-mentioned methods, two specialized processes originating from these are mentioned. The first one is multilayer inkjet printing, in which a large number of layers of different inks are jetted onto a substrate [5]. This might lead to surface inhomogeneities from the printing process itself. On the other hand, substrates to be printed on might already be chemically pre-patterned to guide ink towards desired areas (see, e.g., [6]). In both cases, a liquid is transported on patterned surfaces and evaporates there.

On the other hand, inkjet printing can also be used to actively create surfaces with a wettability pattern that might be of interest for certain engineering applications. For instance, Zhang et al. were able to exploit this particular printing technology to micropattern a superhydrophobic surface with superhydrophilic patches [7]. When the substrates are exposed to an atmosphere in order to collect moisture from it, these show an increased capability to extract water from air compared to surfaces with a uniform wettability. In particular, the patterned surfaces collect up to approximately four times more water than a hydrophilic and twice as much water as a hydrophobic surface per unit area. The idea for these surfaces, however, is based on the outstanding water collection capacity of the *Stenocara* desert beetle in the Namib desert, which exploits this type of wetting pattern to collect water from the atmosphere of one of the driest areas on earth [8, 9]. However, not only for fog harvesting applications, these kinds of surfaces are suitable. They are also useful in chemical and process engineering. For instance, patterned surfaces can be used to increase the efficiency of heat exchangers [10]. Moreover, in purification applications, it can be used to treat, e.g., water-oil emulsions [11]. Even in microfluidic biomedical applications, such as high-throughput screening, chemically patterned surfaces are of interest [12].

The present work deals with sessile droplets on chemically patterned surfaces as they might appear during modern printing processes, or in water harvesting applications, among others (Chapters 5 and 6). Besides this topic, a different way that might be useful to transfer liquid from a reservoir to a substrate, exploiting electrostatic forces, is described and characterized (chapter 7). It is based on the principle of electrospinning, but the thread is guided above the surface of a hydrophilic substrate. This might be useful to improve electrospinning processes since it reduces the degrees of freedom by one dimension and, therefore, might lead to a better controllable process. Methods had to be developed, and surfaces produced that allow to investigate the briefly sketched topics. In all the cases, capillary forces and wetting play the predominant role. The present work is structured as follows:

Chapter 2 gives an overview of capillarity and wetting, focusing on the thermodynamic derivation of the governing equations. The last section of this chapter describes how, for the present dissertation, relevant forces lead to a deformation of capillary surfaces.

Chapter 3 gives an overview of the methods used throughout the present work. The first part describes relevant parts of the experimental setup that has been build up. Then the essential tools of experimental evaluation are described, before the numerical tool Surface Evolver and the developed automatic routine

are presented. These methods represent the available fundamental tools. Based on this, additional features or modifications are discussed in each chapter, if they are necessary.

Chapter 4 deals with the implemented surface modification techniques. The focus lies on the photolithography supported low-pressure chemical vapor deposition silanization, the construction of a reaction chamber for that purpose, and the preparation of hydrophilic surfaces with low contact angle hysteresis. A literature overview is provided for both techniques, and the manufactured substrates are characterized in their specific surface properties.

Chapter 5 presents the investigations on the stability of evaporating water droplets on chemically striped patterned surfaces prepared with the silanization technique described in chapter 4. Stability limits are examined using experiments, numerical calculations with the Surface Evolver, and a simple scaling model. The focus of this study lies in the identification of critical surface parameters, as well as on the prediction of the critical droplet configuration.

Chapter 6 focuses on the breakup dynamics of the droplets having reached their critical shape. Governing forces and different scaling relations are identified during the shape transition towards the next stable liquid configuration. Special attention is paid to the description of remaining satellite droplets.

Chapter 7 deals with the deformation of sessile droplets within an electric field directed parallel to the surface. The focus lies on the characterization of striking aspects of the liquid shape that is called the Surface Taylor-Cone, and the comparison to ordinary Taylor-Cones and a hydrodynamic model.

Chapter 8 summarizes the present work, including its conclusions, and gives an outlook on future work.

2 Theory - Capillarity and Wetting

This chapter gives a short introduction to the topics wetting and capillarity. By no means it is meant to give a complete overview of the broad field of capillarity and wetting. Instead, it is written to illustrate the underlying physics of the present simulations and experiments. Much more insight is given in textbooks such as the ones by deGennes et al. [13] or Butt et al. [14]. Láng gives a comprehensive summary of the thermodynamics of interfaces [15]. In the case of electro-capillary effects, Mugele and Heikenfeld give an extended insight in [16]. The reader is referred to these and many other sources for a more detailed understanding.

2.1 Capillarity from a Thermodynamic Perspective

The internal energy \mathcal{U} of a system can be expressed as a function of its extensive variables entropy S , volume V and the amount of its components i , n_i . This instance can be expressed in mathematical form as

$$\mathcal{U} = \mathcal{U}(S, V, n_i), \quad (2.1)$$

which is the fundamental equation of thermodynamics for a one-phase system. Often, it is more convenient to write this equation in its differential form

$$d\mathcal{U} = \left[\frac{\partial \mathcal{U}}{\partial S} \right]_{V, n_i} dS + \left[\frac{\partial \mathcal{U}}{\partial V} \right]_{S, n_i} dV + \sum_i \left[\frac{\partial \mathcal{U}}{\partial n_i} \right]_{S, V} dn_i \quad (2.2)$$

that contains the thermodynamic definitions of temperature T , pressure p , and chemical potential μ_i of the i th component, i.e.,

$$T = \left[\frac{\partial \mathcal{U}}{\partial S} \right]_{V, n}, \quad p = - \left[\frac{\partial \mathcal{U}}{\partial V} \right]_{S, n}, \quad \mu_i = \left[\frac{\partial \mathcal{U}}{\partial n_i} \right]_{S, V}. \quad (2.3)$$

Setting out from the above equations, it is possible to give a thermodynamic definition of the surface tension.

2.1.1 Gibbs Dividing Surface and the Definition of the Surface Tension

Imagine a closed vessel as sketched in figure 2.1(a). This vessel is filled up to a certain height y_Σ with fluid α , and above this fluid, there is a second fluid β . Then it is possible to describe the inner energy of each fluid j and its extensive variables as

$$\mathcal{U}^j = \mathcal{U}^j(S^j, V^j, n_i^j). \quad (2.4)$$

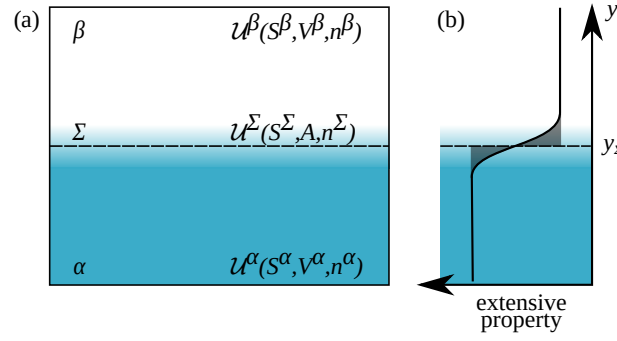


Figure 2.1: The dividing surface in the Gibbs model. (a) shows a closed system with two phases α and β with their internal energies $\mathcal{U}^j = \mathcal{U}^j(S^j, V^j, n_i^j)$. In the Gibbs model, a location of the dividing, two-dimensional interface Σ can be defined such that the absolute of an extensive property of a phase is equal on both sides of the interface (b).

In the real world, there exists a volume with a finite small thickness around y_Σ , where these two phases cannot be distinguished, i.e., there exists *no* sharp interface between them. This is indicated in figure 2.1(a) and (b) by the blue color of phase α that vanishes for larger y .

Josiah Willard Gibbs suggested a model with a dividing surface Σ that has *no* volume, in particular, Σ is infinitely thin [17]. The location y_Σ of Σ is chosen in such a way that the integral along y of some extensive property of the system is zero, i.e., the grey areas above and below the dividing surface in figure 2.1(b) have the same size. Note that with the above-described definition, there is some dis-ambiguity with respect to the exact position y of the interface, as it depends on the extensive property chosen for the integral. However, just as with the two phases α and β , this concept allows to assign the surface entropy S^Σ , the surface area A , and the amount of substances n_i to the dividing surface Σ such that

$$\mathcal{U}^\Sigma = \mathcal{U}^\Sigma(S^\Sigma, A, n_i^\Sigma). \quad (2.5)$$

The internal energy \mathcal{U} of the entire system as sketched in figure 2.1 consists of the sum of the internal energies of the phases α and β and the dividing surface Σ , and therefore it can be written

$$\mathcal{U} = \mathcal{U}^\alpha + \mathcal{U}^\beta + \mathcal{U}^\Sigma, \quad (2.6)$$

or in its differential form, assuming that all intensive variables except for p are equal in all phases and the surface, taking into account equations (2.2) and (2.3)

$$\begin{aligned} d\mathcal{U} &= TdS^\alpha - p^\alpha dV^\alpha + \sum_i \mu_i dn_i^\alpha \\ &+ TdS^\beta - p^\beta dV^\beta + \sum_i \mu_i dn_i^\beta \\ &+ TdS^\Sigma + \sigma dA + \sum_i \mu_i dn_i^\Sigma. \end{aligned} \quad (2.7)$$

Note that in equation (2.7), $\left[\frac{\partial \mathcal{U}^\Sigma}{\partial A} \right]_{S, n_i^\Sigma}$ is substituted by σ , the surface tension. In a closed system, the change in internal energy due to an increase in entropy can be integrated. Moreover, $dV^\beta = dV - dV^\alpha$. For

simplicity, it is assumed that each phase α and β consists of only one component that cannot react with each other. Additionally, these phases are assumed to be insoluble. Then equation (2.7) becomes

$$d\mathcal{U} = TdS - p^\beta dV + (p^\beta - p^\alpha)dV^\alpha + \sigma dA. \quad (2.8)$$

In experiments, it is impossible to control the entropy, and therefore the temperature T is preferred as an independent variable. Furthermore, in some cases, it is more convenient to control the pressure instead of the volume. With the Legendre transformations

$$\mathcal{F} = \mathcal{U} - TS \quad (2.9)$$

$$\mathcal{G} = \mathcal{U} + pV - TS, \quad (2.10)$$

the inner energy \mathcal{U} can be expressed in terms of the Helmholtz free energy \mathcal{F} , which subsequently will be simply called *free energy*, and in terms of the Gibbs free energy, also denoted as Gibbs energy, \mathcal{G} . Substituting the differential of equation (2.9) into equation (2.8) yields

$$d\mathcal{F} = -SdT - p^\beta dV + (p^\beta - p^\alpha)dV^\alpha + \sigma dA. \quad (2.11)$$

Assuming an isothermal system and constant volumes V and V^α , from equation (2.11) follows that

$$\sigma = \left[\frac{\partial \mathcal{F}}{\partial A} \right]_{T, V, V^\alpha} \quad (2.12)$$

in the present case. More generally, it can be shown that in a multicomponent system, equation (2.11) is still valid, when additionally to all other above made assumptions, the amount of substance i is kept constant (see e.g. Butt et al. [14]). This is the definition of the surface tension σ in terms of the free energy. As already mentioned above, it is often more convenient to have constant pressure instead of a constant volume. Then the surface tension can be defined similarly as above by exploiting equation (2.10) instead of equation (2.9) and the surface tension reads

$$\sigma = \left[\frac{\partial \mathcal{G}}{\partial A} \right]_{T, p, n_i}. \quad (2.13)$$

In the present work, it is more convenient to use the definition in equation (2.12) for phases containing only one component. Therefore this equation is written in such a prominent way.

2.1.2 Minimal Surfaces and some Examples

When a mathematician talks about a minimal surface, he or she means some surface of zero mean curvature. In particular, the two radii of curvature perpendicular to each other at every point on the surface add up to 0. A famous example is the soap film which spans between two circular rings. It has a catenoid shape, which is one of only a few minimal surfaces in the mathematical sense for which formulas are known [18].

More generally, and that is the definition used in the present work, a minimal surface is a surface of minimal energy constraint to some boundary. It is convenient to minimize the free energy when the volume is a global constraint and the Gibbs energy when the pressure is known. Some examples for minimal surfaces obtained from energy minimization and a direct consequence from it are presented in the following.

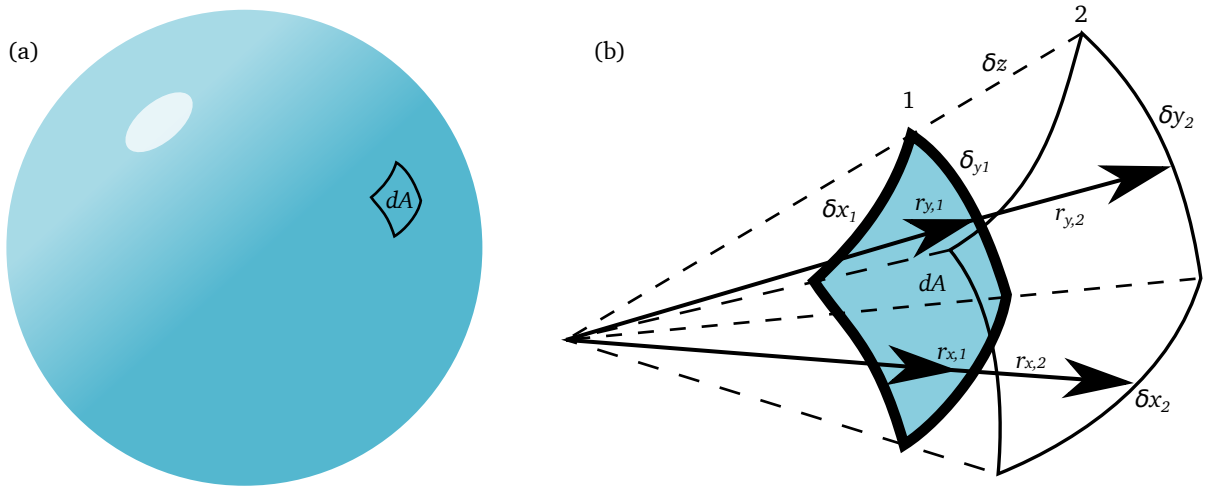


Figure 2.2: Sketch to derive the Laplace pressure. (a) shows a capillary body with a surface element dA . (b) is a sketch of a perturbation of dA by δz with all relevant parameters, similar to [19].

The Laplace Pressure Figure 2.2(a) shows a capillary body, e.g., a soap bubble or a water droplet in the absence of gravity in its equilibrium shape. Its surface area A consists of the sum of all infinitesimally small surface elements dA as it is sketched in black lines on the surface of the capillary body and figure 2.2(b). When $dA = dA_1 = \delta x_1 \cdot \delta y_1$ at position 1 with its two perpendicular radii of curvature $r_{i,1}$, where $i = x, y$, is displaced by δz in the normal direction from its equilibrium to position 2, the radii are $r_{i,2} = r_{i,1} + \delta z = (1 + \delta z/r_{i,1})r_{i,1}$. The area at 2 is then $dA_2 = \delta x_2 \cdot \delta y_2 = (1 + \delta z/r_{x,1})\delta x_1 \cdot (1 + \delta z/r_{y,1})\delta y_1$, which can be easily calculated using the intercept theorem. Now the change in area $\delta A = dA_2 - dA_1$ due to the displacement can be estimated. Some calculus yields $\delta A \approx (1/r_{x,1} + 1/r_{y,1})\delta z dA$, in which higher-order terms are neglected. According to equation (2.11), and presupposing that the total volume, as well as the temperature, stays constant, the change in free energy can be calculated as

$$\delta \mathcal{F} = (p^\beta - p^\alpha)(\delta z dA) + \sigma \delta A, \quad (2.14)$$

in which $\delta z dA = \delta V$. Equation (2.14) equals 0 in the equilibrium state, and with $(p^\beta - p^\alpha) = -\Delta p$ the pressure drop over the free interface can be written as

$$\Delta p = \sigma (\kappa_x + \kappa_y), \quad (2.15)$$

with $\kappa_i = 1/r_{i,1}$, being the curvature associated with the radius of curvature in direction i at position 1, $r_{i,1}$. In general, it does not matter if the radius of curvature r is oriented along with x or y , but they must be considered in directions perpendicular to each other.

In the case of a sphere of radius r , as it is sketched in 2.2(a), $\kappa_x = \kappa_y = 1/r$, and the pressure jump over the interface is $\Delta p_{\text{sphere}} = 2\sigma/r$. On the other hand, when the body is a cylinder, one of the curvatures is 0 and $\Delta p_C = \sigma/r$, with r being the radius of the cylinder. Now reconsider the soap film that is spanned between two circular rings. Since the rings are open, the pressure on every side of the soap film is the same, and therefore, the radii of curvature at every point are 0. This shape is a minimal surface.

The Rayleigh-Plateau Instability The Rayleigh-Plateau instability [20, 21] can be observed every time a water tap is opened. A liquid column of water emerges from the opening of the tap and then spontaneously falls apart into droplets. This effect is a direct result of minimizing the surface area constraint to a constant volume. The derivation can be found in many textbooks, such as the one from Tabeling or DeGennes et al. [22, 13]. The surface free energy of a liquid column \mathcal{F}_C , which is a cylinder with a radius R , constant volume V , and length L , can be expressed as the product of the surface tension σ of the fluid and its surface area A_C

$$\mathcal{F}_C = \sigma A_C = \sigma 2\pi R L = \sigma \frac{2V}{R}. \quad (2.16)$$

This column falls apart into N (spherical) droplets with the surface energy

$$\mathcal{F}_D = \sigma A_D = N \sigma 4\pi R_D^2 = \sigma \frac{3V}{R_D}. \quad (2.17)$$

Following the principle of energy minimization, the liquid column becomes unstable as soon as $\mathcal{F}_D \leq \mathcal{F}_C$ is fulfilled, and therefore

$$R_D \geq \frac{3}{2}R. \quad (2.18)$$

In fact, from an instability analysis (see e.g. Drazin [23]), the wavelength λ belonging to the fastest growing mode can be determined to be $\lambda \approx 2\sqrt{2}R\pi$, assuming that the viscosity can be neglected.

2.2 Wetting

Up to now, the physics of interfaces between two fluids has been discussed. When a third phase is present, and a line is formed where these three phases meet each other, this is called wetting. Wetting can be observed, for instance, during a walk on a spring morning, when dew is sitting on a leaf, where the leaf is the third phase. Since only flat solids are relevant as the third phase in this work, the wetting of soft substrates is not considered. Note that external energies, such as gravity, are not taken into account in the following considerations.

2.2.1 The Contact Angle, Young's Equation, and its Application to Energy Minimization

Figure 2.3(a) shows the sketch of a liquid droplet sitting on a solid. The line (in this two-dimensional case, it is a point) where the three phases gas (g), liquid (l) and solid (s) meet each other is called the three-phase contact line, or simply contact line. Between the solid/liquid and the liquid/gas interface, it is possible to measure a contact angle Θ . With the help of the contact angle, it is possible to characterize surfaces. In general, surfaces are called lyophilic (hydrophilic in the case of water) when Θ is smaller than 90° , and lyophobic (hydrophobic in the case of water) when Θ is larger than 90° . Since only water is used as the liquid in the present work, the terms for water are preferred (as it is done in most literature for other liquids than water). In the following, it is shown that the contact angle in the case of a droplet in its equilibrium state can be calculated from the surface tensions denoted to all interfaces between the different phases, which are σ_{lg} , σ_{sg} , and σ_{sl} at the liquid-gas, solid-gas and solid-liquid interfaces.

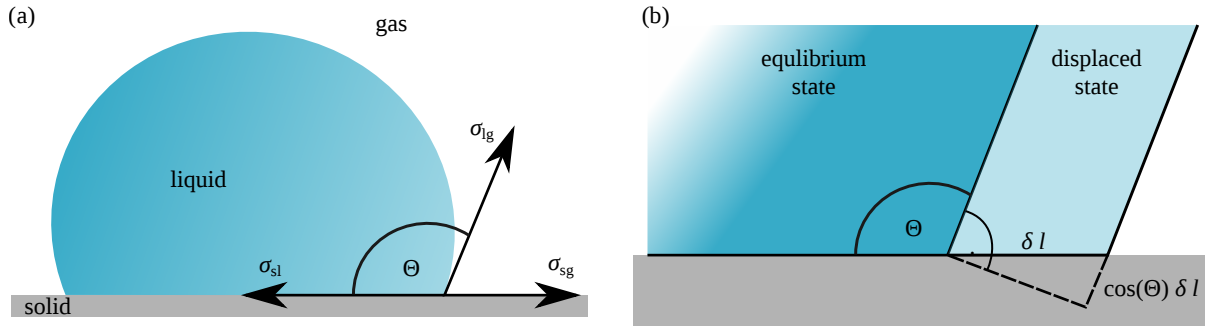


Figure 2.3: Sketch for the derivation of Young's equation. In (a), a liquid sessile droplet in its equilibrium shape wetting a (hydrophobic) surface surrounded by gas is shown. By displacing the contact line, Young's equation (2.21) can be derived. (b) shows a zoom on the relevant area with the displaced liquid.

Young's Equation Emerging from equation (2.11), the free energy of the droplet in its equilibrium state can be calculated as the sum of all products of the areas and the surface tensions of the relevant interfaces, which leads to

$$\mathcal{F} = \sigma_{lg}A_{lg} + \sigma_{sg}A_{sg} + \sigma_{sl}A_{sl}. \quad (2.19)$$

A displacement of the contact line by δl is considered, as it is sketched in figure 2.3(b). The contact angle during the displacement is assumed to be constant. As a consequence, the areas of the interfaces change by $\delta A_{sl} = s\delta l$, $\delta A_{sg} = -s\delta l$, and $\delta A_{lg} = \cos(\Theta)s\delta l$. The change in free energy due to this displacement leads to

$$\delta\mathcal{F} = \sigma_{lg} \cos(\Theta)s\delta l + \sigma_{sl}s\delta l - \sigma_{sg}s\delta l, \quad (2.20)$$

in which s is a unit-length. In equilibrium, the change in free energy must vanish, and therefore $\delta\mathcal{F} = 0$. With this information, equation (2.20) can be rearranged to

$$\sigma_{sg} = \cos(\Theta)\sigma_{lg} + \sigma_{sl}. \quad (2.21)$$

Equation (2.21) is Young's equation, which expresses the contact angle as the function of the surface tensions between all phases present. For convenience, the index lg is dropped in the following, i.e. the surface tension of the liquid-gas interface is denoted as σ .

Free Energy in Case of Wetting It might be essential to minimize the free energy of a sessile droplet or some liquid wetting a solid in some cases. For that purpose, the differential of equation (2.19),

$$d\mathcal{F} = \sigma dA_{lg} + \sigma_{sg}dA_{sg} + \sigma_{sl}dA_{sl}, \quad (2.22)$$

constraint to some boundary conditions, such as the volume, can be minimized. Nevertheless, this requires that σ_{sl} and σ_{sg} are known, which is often not the case. Then these constants need to be determined. However, it is easier to measure the contact angle, and therefore, σ_{sl} and σ_{sg} must be eliminated from equation (2.22). This can be achieved with the following consideration: A flat solid plate with a total area of A_{tot} can be assumed on which a sessile droplet wets the area of A_{sl} and subsequently, $A_{sg} = A_{tot} - A_{sl}$. Since A_{tot} is constant, $dA_{sg} = -dA_{sl}$ and equation (2.22) becomes $d\mathcal{F} = \sigma dA_{lg} + (\sigma_{sl} - \sigma_{sg}) dA_{sl}$. Together

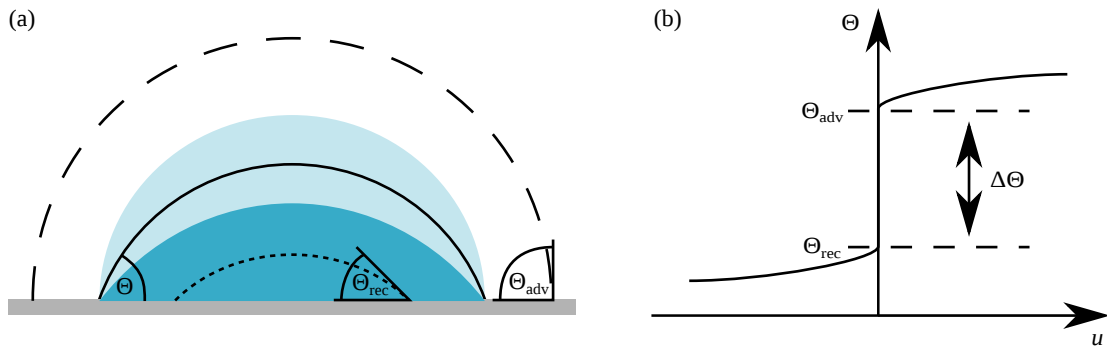


Figure 2.4: The contact angle hysteresis, as it can be observed in goniometric experiments, is illustrated in (a). The solid line shows a droplet with a contact angle Θ . When the droplet volume is increased, Θ is increased, while the droplet radius stays constant, until Θ_{adv} , the advancing contact angle, is reached. When the volume is decreased, the process is inverted towards smaller contact angles, until the receding contact angle Θ_{rec} , is reached. (b) shows the qualitative behavior of the contact angle as a function of the contact line velocity u .

with Young's equation (2.21), the change in free energy of a sessile droplet is

$$d\mathcal{F} = \sigma (dA_{lg} - \cos(\Theta)dA_{sl}) . \quad (2.23)$$

This equation is a useful form for energy minimization methods since σ and Θ are easy to determine experimentally.

2.2.2 Contact Angle Hysteresis

The above section about the contact angle deals with ideal substrates (and fluids), where the contact angle is a unique property of the three present phases as mathematically described by equation (2.21). However, this ideal situation is impossible to achieve in experiments. The following description of a typical process of contact angle measurement illustrates this situation.

When a droplet with a defined volume is placed onto a substrate and reaches a static state, the contact angle Θ can be measured, as sketched in figure 2.4(a) by the solid line. When the volume is increased, it can be observed that the contact line stays pinned, and the contact angle increases until a certain angle is reached. This angle is called the advancing contact angle Θ_{adv} , and the corresponding state is indicated in light blue color in figure 2.4(a). When the droplet volume is further increased, the contact line starts to move with velocity u and the droplet radius increases. Depending on the applied flow rate and, therefore, the contact line velocity, the measurable contact angle can further increase as a function of u , as shown in figure 2.4(b). Usually, the applied flow rate is chosen to be small, so that this process can be assumed as quasi-static, and the velocity of the contact line is on the order of a few $\mu\text{m/s}$. Then the dashed line in figure 2.4(a) indicates a shape of the droplet that is adopted during the volume increase, and the contact angle that is measured during the movement of the contact line is considered as Θ_{adv} . On the other hand, when the volume of the droplet is decreased, starting from the initial droplet shape, the process is inverted towards smaller contact angles with a pinned contact line until, again, a critical contact angle is reached, indicated by the deep blue color in figure 2.4(a). During a further, sufficiently slow, decrease in volume,

this angle stays constant while the contact radius decreases and, on its way, adopts a shape indicated by the dotted line. At this position, the receding contact angle Θ_{rec} can be measured. The difference between the receding and the advancing contact angle is called the contact angle hysteresis

$$\Delta\Theta = \Theta_{\text{adv}} - \Theta_{\text{rec}} . \quad (2.24)$$

Consequently, the value of the equilibrium contact angle Θ lies within the range spanned up by Θ_{adv} and Θ_{rec} .

The contact angle hysteresis has different origins [14]. Emerging from the solid surface, surface roughness and chemical defects or inhomogeneities are the most prominent reason for the hysteresis effect that can even lead to contact line pinning, i.e., a particular region of the contact line is pinned to a point on the surface, while the rest of the contact line moves. However, also fluid impurities that often do adsorb at the contact line can play a role. From an energetic point of view, the ad- and desorption of fluid molecules must be considered as an additional term in equation (2.23) to influence the free energy and, therefore, the contact angle. Finally, line tension-effects that can become dominant for small liquid volumes can influence the contact angle hysteresis.

Note that the contact angle hysteresis can be interpreted as the origin of a lateral adhesion force between the droplet and a surface. It can be written as

$$F_{\text{LA}} = kl\sigma (\cos(\Theta_{\text{rec}}) - \cos(\Theta_{\text{adv}})) , \quad (2.25)$$

with k being a situation specific form factor, and l the wetted length [24]. The contact angle hysteresis is the reason why a droplet at an inclined surface first starts to slide upon a critical inclination angle that depends on the substrate and the liquid. In that case, the driving force is gravity which will be treated in the next section, besides others.

2.3 Influence of External Forces

In the last section, Young's equation (2.21) is derived from energy considerations. However, it can also be understood as a force balance, considering σ as a force per unit length. Note that within this framework, figure 2.3 is not entirely correct, though it can be found in many textbooks. If the sketched droplet is assumed to be in its mechanical equilibrium, a force at the three-phase contact line directed towards the solid is missing since there must be some force counteracting the force normal to the surface. When droplets are set onto soft materials, this resulting force becomes directly visible in its deformation (see, e.g., Style et al. [25]). The present section is about some consequences when other forces become essential, besides the one originating from surface tension, focusing on the gravity and Maxwell stresses due to an electric field.

2.3.1 Influence of Gravity: Bond Number and Capillary Rise Height

Imagine sitting at an office desk on which a glass of water is standing. Accidentally, it is tipped over. When the liquid has come to a rest, typically something can be observed that looks more like a big liquid film with a diameter of maybe 20 cm, and besides this film, maybe some smaller sessile droplets can be

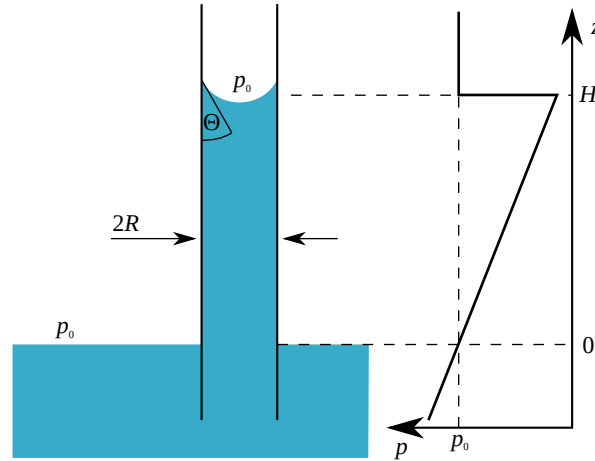


Figure 2.5: The capillary rise height H of a liquid having a contact angle of Θ with the capillary of radius R , and the pressure distribution.

observed with a diameter in the order of approximately 1 mm that have the shape of the one sketched in figure 2.3(a). Why do the shapes of these two disjunct parts of liquid differ from each other, though it is the same material? The answer can be found in the different volumes of these droplets and the force acting on it: gravity.

The Bond Number and the Capillary Length A sessile droplet with a radius of 1 mm has a spherical shape. When the volume is increased, its radius increases, and it can be observed that the shape of the droplet is not spherical anymore but flattened, however, with a contact angle similar to the one of the spherical droplet. Emerging from this observation, the question arises, at which size of the droplet it can be expected that gravity leads to a deformation of the sphere. The answer can be found within a dimensionless number, the Bond-number

$$\text{Bo} = \frac{\Delta\rho g H R}{\sigma}, \quad (2.26)$$

which compares forces originating from gravity g and forces due to surface tension. H and R are two different length scales, and $\Delta\rho$ the difference in density between the liquid and the surrounding fluid. In the case of a sessile droplet, it can often be read that $H = L$, the radius of the droplet. When $\text{Bo} \ll 1$, gravity plays no role, and the liquid surface is a minimal surface (the tiny sessile droplet). On the other hand, when $\text{Bo} \gg 1$, then the influence of the surface tension can be neglected, which leads to the liquid film-like shape in the water glass example. When $\text{Bo} = 1$, then the relevant surface- and volume forces are equal. If furthermore, the density of the surrounding fluid can be neglected, and $H = L$, then equation (2.26) can be transformed to

$$l_c = \sqrt{\frac{\sigma}{\rho_1 g}}, \quad (2.27)$$

with the capillary length l_c and ρ_1 the density of the liquid. In the case of water, $l_c \approx 2.7$ mm

The Capillary Rise Height Another consequence from gravity is the rise height H of some liquid within a capillary of radius $R \ll l_c$ that is dipped inside a pool of the liquid. The contact angle between the liquid and the capillary is Θ , and the liquid has a surface tension σ and a density of ρ_1 . The situation is sketched

in figure 2.5. Since $R \ll l_c$, the shape of the liquid within the capillary can be assumed as spherical, and according to the Laplace-equation (2.15), the pressure jump across the interface is $\Delta p = \sigma(2 \cos(\Theta)/R)$. The pressure within the surrounding gas is p_0 at each position above the liquid, and it is assumed that the density of the gas is negligible compared to the one of the liquid. With the hydrostatic pressure ρgH , the capillary rise height can be calculated as

$$H = \frac{2 \cos(\Theta) \sigma}{\rho g R}. \quad (2.28)$$

Note that it is assumed that the fluid rim around the spherical shape of the liquid is not taken into account for the calculation of the hydrostatic pressure.

2.3.2 Influence of Electrostatic Forces: Maxwell-Tension and Taylor-Cone

Another force that may act on liquid droplets and influences their shape are electrostatic forces due to an electric field \vec{E} . In the case of a plate capacitor, this is the ratio of the potential difference U and the distance l between the two plates, i.e., $E = U/l$, since \vec{E} has only one component in the particular case. When a particle of charge q is placed between the two plates, a force F_{el} acts on this particle, and, depending on the sign of the charge it is attracted to one of the plates. In general, the force acting onto a charged particle is called the Coulomb force and is written as

$$\vec{F}_{el} = q\vec{E}. \quad (2.29)$$

Maxwell-Tension In the case of a charged fluid instead of the particle, the interface may deform due to the electric field, and therefore, a different electric field and charge distribution arises. Hence, local forces at the fluid surface must be considered. The tension acting on the fluid can be expressed by the Maxwell stress tensor [26]

$$\mathcal{T}_{ik} = \epsilon_0 \epsilon \left(E_i E_k - \frac{1}{2} \delta_{ik} E^2 \right). \quad (2.30)$$

i and k are the three dimensions in space x, y , and z , and δ_{ik} is the Kronecker-delta. ϵ_0 is the permittivity of the vacuum and ϵ the one of the liquid. In the case of a perfectly conducting liquid, only normal stresses on its surface are relevant [16]. Note that water can be considered as perfectly conducting due to the presence of dissolved ions and the auto dissociation effect, i.e., water dissociates into positively charged H_3O^+ and negatively charged OH^- -ions. The resulting force due to an electric field onto the surface of this liquid can, therefore, be calculated by integrating equation (2.30) over its surface A_1 . This results in

$$F_{el,i} = \oint_{A_1} \mathcal{T}_{ik} n_k dA. \quad (2.31)$$

Subsequently, taking only into account the normal direction n_k , equation (2.31) can be expressed as a force per surface area A in its normal direction \vec{n} [26]

$$\frac{\vec{F}_{el}}{A} = \frac{\epsilon_0 \epsilon}{2} E^2 \vec{n}. \quad (2.32)$$

The force acting on A can be calculated with equation (2.32), when the electric field at this position is known.

The electro-capillary number and the Taylor-Cone In general, however, this is not the case, and numerical calculations are needed. At least a dimensionless number exists, with which the force on a liquid's surface due to the electric field can be compared to surface tension forces. In particular, this is the Electro-Capillary-number

$$\text{Ca}_{\text{el}} = \frac{\epsilon_0 \epsilon E^2 L}{\sigma}, \quad (2.33)$$

with L being a relevant length scale [27]. Nevertheless, one famous, analytical solution of a situation where forces due to surface tension and Maxwell stresses are pre-dominant exists. It is named after Sir Geoffrey Ingram Taylor, who was the first person who theoretically described it in 1964, and is called the Taylor-Cone [28]. However, already in 1917, John Zeleny experimentally observed this cone that forms from a liquid drop at the tip of a needle located on the opposite side of a conductive plate [29]. Between the needle and the plate, an electrostatic potential U is applied. It can be observed that the initially spherical cap-shaped capillary surface approximates a cone shape until a liquid jet emerges upon a critical voltage. Taylor calculated this last stable cone shape to have a unique opening angle of 98.6° [28].

3 Global Methods

This chapter gives an overview of the used methods throughout this thesis, including the experimental setup, image processing, and the Surface Evolver. Note that if further details are needed additionally to the ones given in this chapter, they are presented in the relevant chapter. My colleague Michael Heinz from the Institute for Technical Thermodynamics, TU Darmstadt, programmed the excellent MATLAB-tool DENIISE: Droplet Evolution: Impact, Imbibition, Spreading, Evaporation which is used to evaluate side view data to extract time-dependent information about the contact angle of droplets on surfaces [30]. Frank Plückebaum, Jörg Bültemann (both Institute for Nano- and Microfluidics, TU Darmstadt), and Marcel Neu, a former student, helped with the construction of the experimental setup. Günther Auernhammer from the Leibniz-Institut für Polymerforschung Dresden e.V. gave some valuable ideas on some features of the experimental setup. It was constructed as a central setup within the Collaborative Research Centre (CRC) 1194 Interaction between Transport and Wetting Processes. During the design process, maximum adaptivity had to be considered to allow other experiments to be performed in it. Therefore, it contains some optional features that have not or only rarely been used in the work presented here. Moreover, different versions of the experimental setup do exist. In this chapter, the central instance, also termed "benchmark configuration", is presented. Some described features can be transported or adopted to different versions of the setup.

3.1 Experimental Setup

Figure 3.1 gives an overview of the constructed central experimental setup. A rack build from Item profiles (Item Industrietechnik, Germany) serves as the basic structure that is put on an optical table (Vision Iso Station, Newport, USA, not shown). The primary purpose of the benchmark configuration is the observation of processes of objects, most often droplets, ideally from two perpendicular directions. For that purpose, objects to be observed must be put on the manual x - y - z -stage that allows movement in all three directions in space, as depicted by the red arrows in figure 3.1. The stage consists of two parts, i.e., an x - y -stage (Nikon, Japan) mounted onto a manual lab jack (model 281, Newport, USA). In figure 3.1, an optional climate chamber is depicted which allows the experimenter to perform measurements in a constantly humidified atmosphere (see section 3.1.1 for further details). Another optional feature sketched in figure 3.1 are two guide rails that, for instance, can be used to precisely position a needle tip above a substrate. Some details on the droplet application can be found in section 3.1.2. Since in general, the behavior of droplets on different kind of surfaces is to be observed, the objects must be magnified. For that purpose, 12X macro objectives (Navitar, USA) are used for side and top view magnification. These objectives allow an individual adjustment of the magnification and can be supplemented with additional lenses. Moreover, both have a build-in fine focus, allowing to fine-tune the focus plane. The magnified image is recorded with two high-speed cameras, i.e., the FASTCAM SA1.1 in top view mode and the FASTCAM SA-X2 in side view mode (both Photron, Japan) are used for most experiments, but other cameras can be put onto the camera

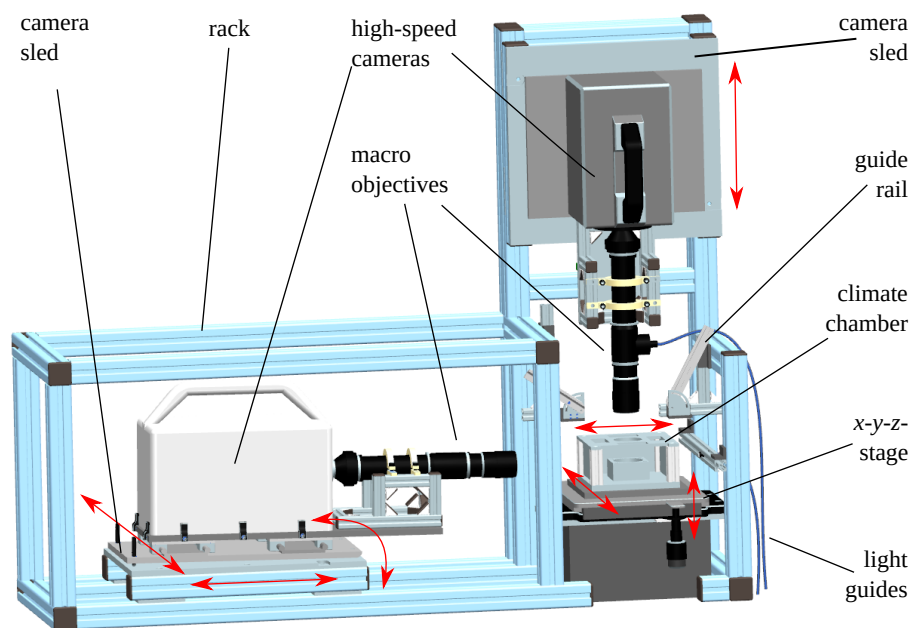


Figure 3.1: Overview of the central experimental setup. It allows individual and synchronized, magnified observations in top and side view of processes that may happen inside of an optional climate chamber. Guide rails may be used, e.g., for targeted feeding of fluids, such as droplets. Red arrows mark possible directions of movement.

sleds as well. Further details on the optics can be found in section 3.1.3. The sled for the camera in top view mode can be moved up and down. This allows moving the object to the correct working distance of the objective and, therefore, to focus it. Moreover, it also permits experiments that do require a setup with a high-build construction, but only side view observations. To be able to observe a process from two sides simultaneously, it is required that the two optical axes do intersect each other at the location of the object. Therefore, the side camera can be moved back and forth. Additionally, it can be tilted by about 10° and moved from left to right and back, to be able to move the optical focus into the object level. Illumination is performed via two light guides, each connected to a single Intra LED 5 cold light source (Volpi, Switzerland). In the case of side view imaging, the illumination takes place as backlight illumination. Optionally, a diffuser can be put between the outlet of the optical fiber and the object. For top view images, the outlet of the light guide is put into an objective specific fiber intake (Navitar, USA). The light is then reflected by 90° so that it is coaxial with the viewing direction of the objective. The reflected light that comes from the object can pass this mirror and subsequently falls onto the sensor of the camera. Synchronization of the cameras is achieved with the Photron Fastcam Viewer software (Photron, USA) that is also used to record the images. Triggering of the cameras is performed in end-triggering mode with the shutter controller SC10 (Thorlabs, USA), giving the trigger signal.

3.1.1 Humidification

When the shape evolution of sessile water droplets during evaporation is of major interest, it is essential that the atmosphere around the droplet can be set to a constant humidity in different experiments to enable its comparability. One way to achieve this is sketched in part (a) of figure 3.2, and the realization of the climate chamber is shown in (b). A nitrogen stream is split up into two individual tubes that do

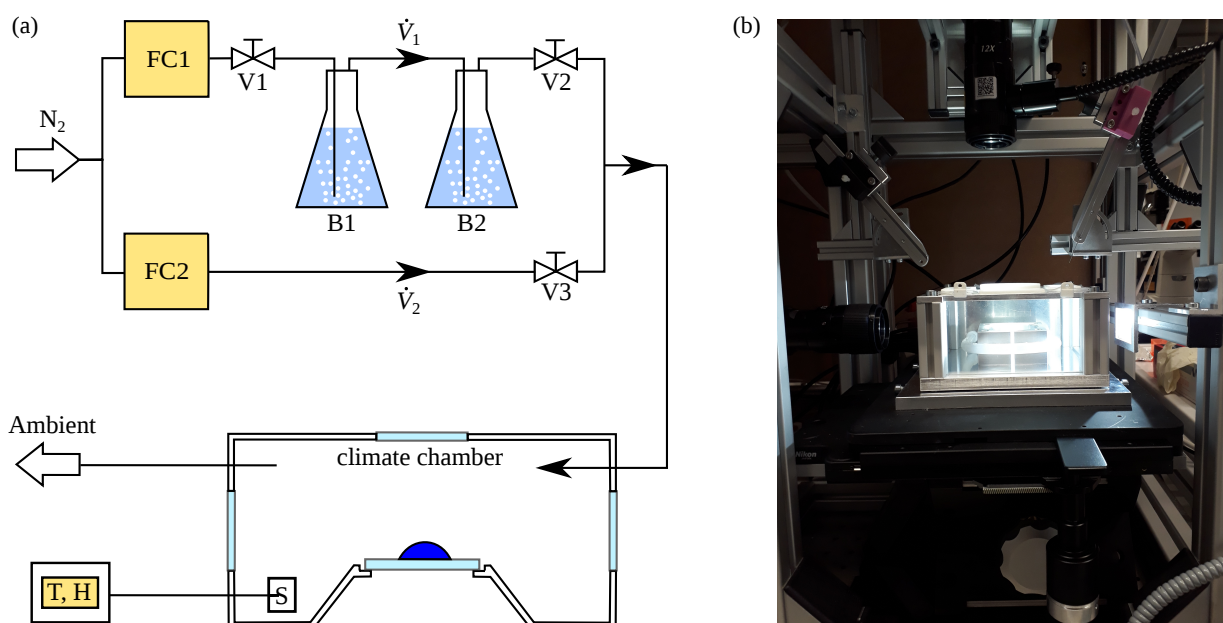


Figure 3.2: Humidification of the atmosphere inside the climate chamber. (a) shows a sketch of the process and (b) the climate chamber on the x - y - z -table of the benchmark configuration.

feed two flow controllers FC1 and FC2 (Series 358, Analyt MTC, Germany) with a maximum flow rate of 500 ccm/min, each. The flow rate \dot{V}_1 that is controlled by FC1 is lead through two 500 ml borosilicate glass bubblers B1 and B2 (Carl Roth, Germany) filled with DI-water (from Milli-Q device, 18.2 M Ω ·cm). The outlet within the bubbler is equipped with a filter plate. This ensures that many small gas bubbles rise through the liquid, resulting in an improved mass transfer compared to larger bubbles so that the nitrogen is almost saturated with water vapor when it leaves B2. This humidified nitrogen stream is mixed with a not-humidified one, having a flow rate \dot{V}_2 set by FC2. The mixed stream is then lead through the climate chamber. By individually controlling \dot{V}_1 and \dot{V}_2 , humidities between ~ 10 %rh and ~ 90 %rh can be achieved. The humidity and temperature are measured simultaneously by a self-build device. It uses the digital sensor SHT75 (Sensirion, Switzerland) that is connected to the microcontroller Arduino UNO (Arduino, Italy) that converts the signal into values for temperature and humidity and can be read out by a computer and pass the values instantaneously forward to a connected display. The accuracy of the humidity measurement within the humidity window between ~ 10 %rh and ~ 90 %rh is ± 1.8 %rh and the accuracy of the temperature is typically ± 0.4 °C. All tube connectors and the valves (BOLA, Germany) are made from PTFE. The tubes are made out of FEP. Both materials assure a sufficient chemical resistance against most common fluids. This allows using other liquids than water. The valves V1, V2, and V3 are a safety precaution that water (or a different liquid inside of the bubblers) cannot reach the flow controllers or the inside of the climate chamber when the humidification system is not operated.

The climate chamber itself, as it can be seen in figure 3.2(b), consists of a square aluminum ground plate with a substrate holder located in the middle. At each corner of the climate chamber, a 1 cm \times 1 cm item profile (Item Industrietechnik, Germany) is mounted vertically on the ground plate. At the rear part of the climate chamber, a metal plate with three boreholes (two for the in- and outlet of the humidified nitrogen stream and one for the humidity sensor) is installed. The humidity sensor itself is located close to the substrate to assure accurate humidity measurements near the evaporating droplet. The other three

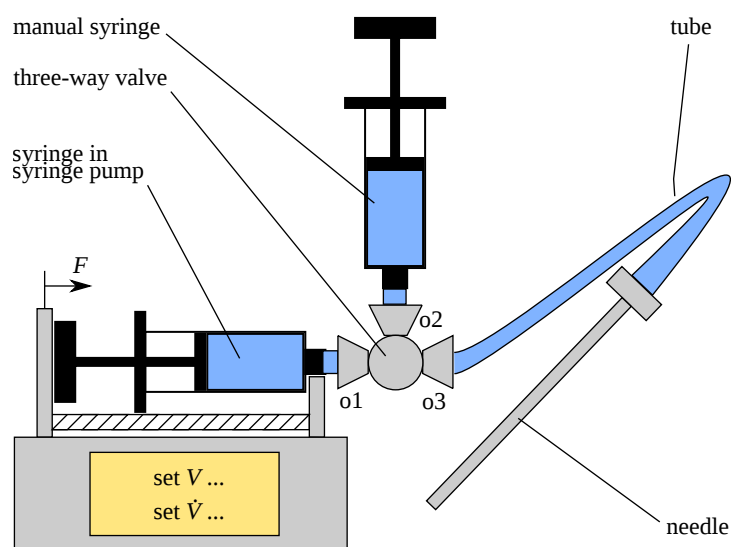


Figure 3.3: Sketch of the droplet dosing unit. A force F is applied to the plunger of the syringe by the syringe pump. The outlets of the three-way valve are denoted as o1, o2, and o3.

sides of the climate chamber are closed with acrylic glass windows. The front window can be lifted up to have easy access to the inside of the chamber. The top plate is equipped with a center hole in which a 2-inch borosilicate wafer (Microchemicals, Germany) is mounted. Parafilm (Pechiney Plastic Packaging, USA) is stretched and clamped into four rectangular cutouts by a 3D-printed parafilm holder. This allows the separation of the chamber atmosphere from the laboratory. However, the parafilm membrane can be penetrated with a needle to place droplets on the substrate. All metallic parts are made from aluminum. If a chemically more resistant chamber is required, aluminum can be substituted by a suitable stainless steel and the acrylic glass by borosilicate glass.

3.1.2 Droplet Dosing

Droplets can be placed by pipetting them with different pipettes (Eppendorf, Germany) onto the surface. This is the preferred method throughout this thesis since it is fast, simple, and dosing is of high accuracy. However, this is hardly possible when droplets should be set on a substrate within the climate chamber or when droplets are applied during a running process, which does not allow a manual application. E.g., this is the case when droplets are placed within a strong electric field. For that purpose, a different system is constructed, as shown in figure 3.3, to put droplets with a defined volume and flow rate onto surfaces. Precise dosing is achieved by using a syringe pump (Legato 100, KD Scientific, USA). The pump can be equipped with different sized syringes. In any case, it is a gastight glass syringe (1000 Series Gastight, Hamilton, USA) with a Luer Lock adapter at the syringe outlet. This allows the experimenter to mount a three-way valve (also called three-way stopcock, Fisher Scientific, Germany) to the syringe at o1 of the valve (see figure 3.3). At one end of the valve (o3), a FEP-tube is mounted that guides the liquid to a needle in case of droplet dosing (steel needle, GA26, Hamilton, USA), as it can be seen in the upper right corner of image 3.2(b). Alternatively, a different needle can be mounted and be connected to some other fixture, as it is the case, e.g., in chapter 7. To ensure a precise, leakage-free dosing of liquid volumes, no gas bubbles must be present within the system. Moreover, small volume syringes within the pump allow more accurate dosing of the final volume. However, the volume might be too small to fill up the whole

tube before dosing the droplet at the needle tip. Therefore, a second liquid reservoir is needed at o2 of the three-way valve. By actuating the pump with closed o3, but no liquid reservoir attached to o2, gas can be pushed out between these two points. Then a second syringe with a larger volume is connected to o2, and the valve is switched to the o2 - o3 position. In this way, the whole tubing can be filled with the liquid. By then switching the valve to the o1 - o3 position, droplets can be dosed with well-defined flow rates and end volumes. All connections are Luer Lock connections.

3.1.3 Some Consequences from Optics

To be able to extract quantitative information from an image, it is essential that the used optics can resolve the relevant image features. The optical resolution ξ , i.e., the minimal distance between two observed objects that can be distinguished, can be calculated as

$$\xi = \frac{0.61\lambda}{NA}, \quad (3.1)$$

with the wavelength of the used light source λ and numerical aperture of the objective NA . Equation (3.1) is a direct result of the wave properties of light and its diffraction at the objective. The reader is referred to appropriate textbooks such as [31] for a derivation of the above formula. On the other hand, the experimenter depends on the available optical instruments (of course, the numerical aperture is a property of the objective, as well). From these, a different, more practical criterion can be derived to estimate the minimum distance between two neighboring points that can be distinguished. This is the spatial resolution of a digital image, also denoted as pixel resolution ξ_{px} . Digital images consist of pixels. The number of pixels, as well as its pixel resolution ξ_{px} , depend on the sensor of the camera and the size of one physical sensor pixel, i.e. $20 \mu\text{m}$ in the case of the two high-speed cameras (see table 3.1), as well as the magnification of the used objective and can be calculated as

$$\xi_{\text{px}} = \frac{l_{\text{px}}B}{M \cdot M_{\text{at}} \cdot M_{\text{mount}}}. \quad (3.2)$$

In equation (3.2), B is the binning of the camera sensor, i.e., the number of pixels that can be connected, M is the objective magnification, M_{at} the lens attachment magnification, M_{mount} the magnification of the used objective mounting, and l_{px} the physical dimension of one pixel on the sensor. Note that B is always 1 in the present work, i.e., each pixel of the final image represents one camera pixel. Therefore, assuming a constant magnification and pixel length, different properties of an object in a digital image can only be distinguished when the distance between them is at least ξ_{px} .

The tubes of the objectives always consist of the 12X Navitar macro objective with which magnifications between 0.58x and 7x are possible. Three lens attachments of $M_{\text{at}} = 0.5\text{x}$, 1.0x (none), and 1.5x are available at the benchmark configuration. The additional F-Mount magnification is 2.0x in case of the side

Table 3.1: Important properties of the used cameras.

Camera	l_{px}^2 ($\mu\text{m} \times \mu\text{m}$)	type	size sensor (px \times px)	f_{max} (fps)
Photron SA1.1	20×20	CMOS	1024×1024 at 5400 fps	675000
Photron SA-X2	20×20	CMOS	1024×1024 at 12500 fps	1080000

view and the C-Mount magnification is 1.0x in the top view. The Image Pixel size can be calculated with these pieces of information and the above formula. Note that also the working distance l_w , i.e., the distance between the objective and the object, and the depth of field l_{dof} , i.e. the optical sheet width on the object's side that can be focused, depends on the used objective combination. All relevant information, including the numerical apertures, are summarized in table 3.2 [32].

Note that the optical resolution and the pixel resolution are not the only limiting factors, especially in high-speed imaging. Since the frame rate f defines the maximum exposure time, it also influences the amount of light that falls onto the sensor of the camera. On the other hand, an increased magnification and, therefore, higher optical and pixel resolution, does result in a decreased intensity of light that arrives at the sensor. Simultaneously, also the maximum amount of light is limited by the used light source, and the size of features that can be observed is limited by physical factors that must be taken into account (e.g., the Bond number). Therefore, the experimenter always has to make a compromise between available light, magnification (and thus spatial, and pixel resolution), and the frame rate, i.e., the temporal resolution.

3.1.4 Alternate Experimental Setups

Due to the limitations discussed in section 3.1.3, i.e., the limited optical resolution, it may be necessary to perform some experiments with an alternate experimental setup. Therefore, the above features of the benchmark configuration are designed to be transferable to other locations. In the present work, this is the inverse microscope Eclipse TI (Nikon, Japan). A microscope is built for large magnifications and, therefore, the microscopy optics ensures a sufficient spatial resolution. By coupling the end of the light guide into the microscope and focusing it by a condenser lens, enough light is available. The high-speed cameras can also be attached to the microscopy body and, therefore, this alternate setup has the advantage of an increased possible temporal and spatial resolution. Moreover, other experimental methods such as confocal imaging, total internal reflection (TIRF) measurements or epifluorescence measurements are available within this setup, when using different cameras than the high-speed cameras. However, since the microscope is inverted, only transparent substrates can be used within the alternate setup. Moreover, side view images are hardly possible due to a lack of space for additional constructions around the microscope.

Table 3.2: Optical properties of the available objective combinations for minimum (low) and maximum (high) magnification [32].

M_{at}	M_{mount}	l_w (mm)	M_{tot} (low - high)	NA (low - high)	ξ (μm) (low - high)	ξ_{px} (μm) (low - high)	l_{dof} (μm) (low - high)
0.5	1.0	165	0.29 - 3.50	0.009 - 0.051	37.04 - 6.66	68.97 - 5.71	6.17 - 0.19
None	1.0	86	0.58 - 7.00	0.019 - 0.101	18.52 - 3.34	34.48 - 2.86	1.39 - 0.05
1.5	1.0	50	0.87 - 10.50	0.028 - 0.151	12.34 - 2.24	22.99 - 1.90	0.64 - 0.02
0.5	2.0	165	0.58 - 7.00	0.009 - 0.051	37.04 - 6.66	34.48 - 2.86	6.17 - 0.19
None	2.0	86	1.16 - 14.00	0.019 - 0.101	18.52 - 3.34	17.24 - 1.43	1.39 - 0.05
1.5	2.0	50	1.74 - 21.00	0.028 - 0.151	12.34 - 2.24	11.49 - 0.95	0.64 - 0.02

3.2 Data Evaluation

High-speed imaging techniques allow the experimenter to gain a better insight into processes that take place on very small time scales below 1 ms or even smaller. The number of images which has to be processed in order to extract dynamical information on some parameter can be very large, in the order of $\sim 10,000$ images, so that it is impossible to manually evaluate all experiments in a reasonable amount of time. But even when static behavior should be investigated, automatic evaluation has a lot of advantages in terms of time savings and accuracy over the manual evaluation that, of course, also must be performed in some cases. For manual image evaluation, tools such as fiji [33] that is based on imageJ [34, 35] can be used, as it is also the case in the present work. Besides that, however, it is indispensable to exploit the advantages of automatic algorithms in order to evaluate image data, which in the following is also called primary data.

3.2.1 Used Software Tools

In the case of evaluation of the images that were taken in side view mode, some tools are exploited that are not developed in the present work. I.e., these are the tool DENIISE: Droplet EvolutionN: Impact, Imbibition, Spreading, Evaporation programmed by Michael Heinz [30], and another external tool developed by two Greek groups [36]. Both tools are written in MATLAB and use packages that are implemented within this scripting environment. The reader is referred to the above-mentioned papers and the literature cited therein for more information.

In contrast to the side view data, top and bottom view data are evaluated using the Python programming language. Image processing often requires image manipulation techniques, such as different filters or morphological operations. Also, this is done in the present work. For that purpose and in order, of course, to detect edges of features of interest, built-in methods of the scikit-image library [37] are used in version 0.14.2.

3.2.2 General Steps in Image Processing

The main tasks which must be performed within the image analysis consist of three general steps. These are summarized in figure 3.4. Part (a) of this figure shows an image from a recording of the breakup of a capillary bridge that is taken as an example. The steps are as follows:

1. Read in each image from an image sequence separately or a single defined picture (see figure 3.4(a))
2. Detect the edges of the feature of interest. For that purpose, manipulate the image as much as it is necessary (see figure 3.4(b))
3. For further data processing extract the coordinates of the relevant feature(s) (see figure 3.4(c))

Steps number 1. and 3. can be performed with standard scripting methods, while step number 2. is the central step within image evaluation. The following section is about edge detection as the central method applied throughout the evaluation of all experiments. However, the specific evaluation algorithm may differ for each different type of experiment. Therefore, the reader is referred to each chapter for more details on the respective algorithm how the edge detection is embedded within the image evaluation.

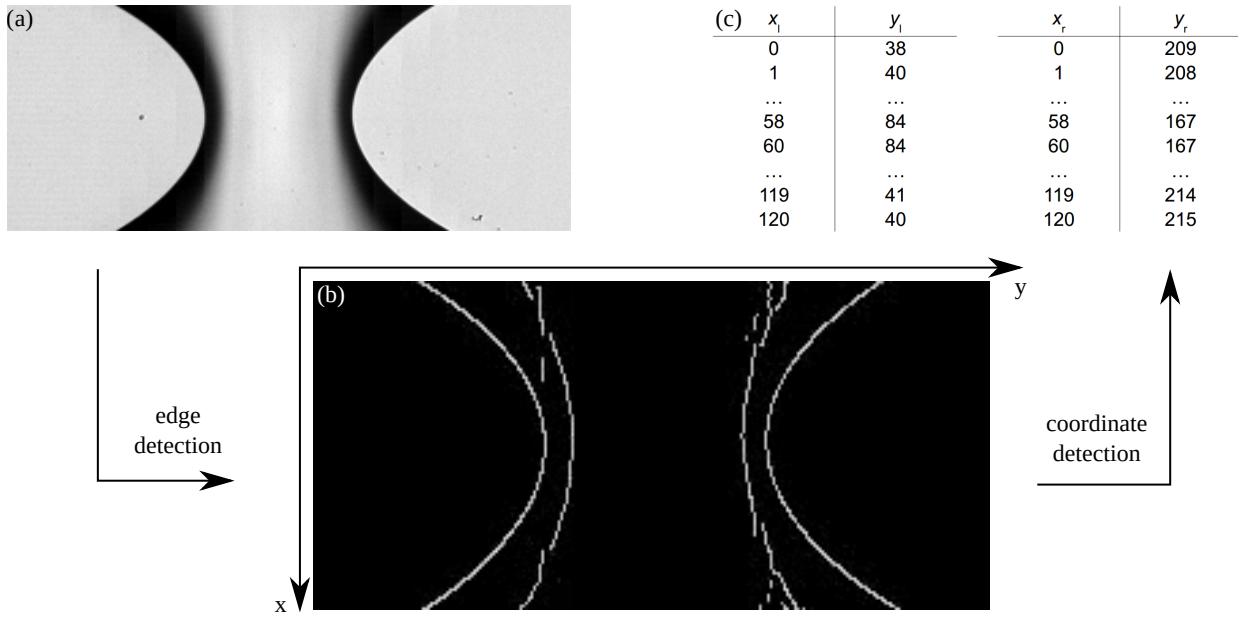


Figure 3.4: Visual description of the main steps of image detection. From a read-in image in an image stack as shown in (a), the edges are detected (b). From these data, the coordinates of the left and right edges of the capillary bridge can be detected (c).

3.2.3 Edge detection

A digital grayscale image consists of $n \times m$ pixels. Each pixel may have a value v between 0 (black) and some maximum value (white), which is 256 in an 8-bit image. Each image within an experiment is evaluated separately in case of a high-speed image series, or the image is defined if only one is of interest (as in chapter 7). In a first step, the image is manipulated using the closing operation, i.e., small dark spots that may appear due to, e.g., dust on the substrates or at any place in the optical path, such as lenses or the camera sensor, are removed. For this purpose, a parameter can be set. It defines the maximum size in pixels of the spot that is removed.

The following Gamma Correction step is performed to increase the contrast of the images. Each grayscale value of a pixel of the input image $v_{in}(x,y)$ is exponentiated by γ :

$$v_{out}(x,y) = v_{in}(x,y)^\gamma \quad (3.3)$$

where $v_{out}(x,y)$ is the value of the output pixel. This step can be important, especially in the case of high-speed imaging, where the recording frequency, magnification, and maximum amount of light are always competitive, and the experimenter often struggles with low contrast images (see section 3.1.3 for further elaboration). Additionally, Gamma Correction increases the gradient in grayscale values inside the image, which is vital for the following edge detection step that is performed by the Canny edge detection algorithm [38, 39].

The first step within the edge detection algorithm is the smoothing of the image using a Gaussian filter, i.e., a Gaussian low-pass filter. For that purpose, the parameter σ is defined at the beginning of the script. σ is the width of the normal distribution of the filter and is not to be confused with the surface tension. In

the next step, the gradients within the image are detected by applying a Sobel filter in the horizontal and vertical direction¹. The Sobel operator calculates the gradients of the grayscale pixel values $v(x,y)$ in x - and y -direction and then localizes the maxima of the magnitude of the gradient of $v(x,y)$

$$|\nabla(v(x,y))| = |v_x| + |v_y|, \quad (3.4)$$

which is a simplified version for computational purposes of the mathematically correct version $|\nabla(v(x,y))| = (v_x^2 + v_y^2)^{1/2}$. Additionally, the direction χ is calculated with

$$\chi = \tan^{-1} \left(\frac{v_x}{v_y} \right). \quad (3.5)$$

Ridges have their maxima in $|\nabla(v(x,y))|$ in the direction of the gradient [39]. In the following step, only the maxima are conserved within a matrix, and other values are labeled as 0. The Canny edge detection algorithm has a low and high threshold value as two additional input parameters. The ridge values can be classified with these values into weak and strong ridge pixels. This information can then be used to connect the pixels on which the ridge is located. For more information concerning the Canny edge detection algorithm and the Sobel operator, the reader is referred to [39].

The processed image is stored in a final step one after the other in a 3D-array in case of high-speed images or as a single image when only one image should be processed. This eases the surveillance of the evaluated images.

3.3 Numerical Setup - The Surface Evolver

The Surface Evolver is a numerical tool developed by Kenneth Brakke, first published in 1992 [41]. It can be used to minimize the energy of surfaces subject to constraints such as volume, pressure, or level-set constraints, using gradient descent and optionally conjugate gradient method. Besides the surface tension, also volume energies such as gravity may be considered.

3.3.1 General Overview and Functionality

Since the Surface Evolver is a finite-element tool, the total surface is represented by many triangular elements called facets. In a limited way, Surface Evolver handles any number of dimensions, but it is built for two-dimensional facets in a three-dimensional space, and only within this framework full functionality is guaranteed. Therefore, this is how it is used in the present work, and the brief description is limited to this case. Each facet is defined by three vertices, attributed to three coordinates, which are connected by three linear edges forming the triangle. These edges can be refined in order to gain more precise results, for instance, in terms of surface curvature. Other important mesh manipulation methods are equiangularization and vertex averaging. The face consists of the sum of all facets and may surround a body such as a droplet.

¹The Sobel operator was never published by the authors themselves. Sobel and Feldman only presented their work in a talk called "A 3x3 Isotropic Gradient Operator for Image Processing" at the Stanford Artificial Intelligence Project (SAIL) in 1968. Nevertheless, the operator was named after Sobel after the talk was credited inside of a footnote in a book by Duda and Hart. The history and the documentation of the talk of the Sobel operator can be found in [40].

Vertices and edges may lie on constraints, such as level-set constraints, or they can be prohibited to move above certain boundaries in space. Faces are attributed to surface tension. In the case of wetting, contact angles are more convenient to use than surface tensions (except for the surface tension between liquid and gas). These are implemented as energy constraints in the form of line integrals. Bodies may have a constant volume or constant pressure. A density can be defined with which also gravity as volume energy can be considered. Besides these implemented boundaries and constraints, any other energetic constraint may be defined by the user.

The main feature within the Surface Evolver is the iteration step. This operation allows the surface to evolve towards an energetic minimum. When the surface tension of a sessile droplet is the only present energy, i.e. when gravity can be neglected, contact angles are known system properties, and the body is attributed to a certain volume, then the free energy of a system

$$\mathcal{F} = \sigma (A_l - \cos(\Theta)A_{sl}) \quad (3.6)$$

can be minimized. In the present case, this can only be achieved by changing the areas A_l and A_{sl} , while adhering to the volume constraint. A minimum is reached, when the differential of equation (3.6) is 0, i.e.,

$$d\mathcal{F} = \sigma (dA_l - \cos(\Theta)dA_{sl}) = 0. \quad (3.7)$$

Within an iteration step, each involved vertex is moved due to a before calculated force, which is the negative gradient of the energy function at each vertex, multiplied by a globally defined scale factor using the gradient descent method. The Surface Evolver makes sure that all constraints and boundaries are taken into account during the movement by mapping the force on the tangent of the boundary or mapping it back in case of constraints. To increase the efficiency of the energy minimization iterations, the conjugate gradient method can be used.

Further information on how to employ the Surface Evolver that is used in version 2.70 in the present work, can be found in [41] or the manual that is delivered with the download of the software. Many examples for which the Surface Evolver can be used can be found in [18].

3.3.2 An Automatic Routine

The Surface Evolver originally is designed as an interactive command line tool. The user first defines the initial geometry, boundaries, constraints, and energies within a data file and then performs mesh operations such as refining and surface evolving with one-letter commands in a terminal while observing the surface and the command line output, i.e., the calculated energy, after each operation.

In the present work, an own iteration routine has been implemented to automate the evolution process and uniformly judge about convergence. It makes use of already implemented features and consists of four main steps.

1. The surface of some problem is evolved in one iteration step, as described in the previous section.
2. The total energy of the surface (and the body) of the actual shape is read out and the coefficient of variation of the last 7 iterations is calculated.
3. Relevant edges are refined when some edge length is larger than a user-defined maximum edge length.

4. Relevant facets are merged when some edge length is smaller than a user-defined minimum edge length.

These four steps, plus an optional task-relevant fifth step that includes all problem specific operations, are repeated within a loop until a convergence criterion is reached. A simulation is considered as converged when the coefficient of variation of the last seven iterations is smaller than a user-defined convergence criterion. Taking the coefficient of variation has the advantage that this is a relative error measure that is independent of the absolute value and, therefore, problems of different length measures can be handled with the definition of this convergence criterion. The idea of combining the iteration with an energy-based convergence criterion is implemented similarly in the SE-FIT [42], which is, simply speaking, a graphical user interface for the Surface Evolver with many extended features.

4 Surface Modification Techniques

This chapter gives an overview of the theory and the realization of the used surface modification techniques to obtain the results in the present work. Moreover, the characterization of these substrates is presented. Klaus-Dieter Voss performed the photolithography steps. Atomic-Force measurements were done by, and ellipsometric measurements were performed under the guidance of Beatrice Fickel.

4.1 Introduction

In chapter 1, it has been shown how humanity has used the wetting behavior within capillaries or on papyrus to develop the technique of writing and printing. It has also been revealed that the *Stenocara* desert beetle in the Namib Desert [9] exploits wetting patterns to harvest water from air. But also a lot of plants and other animals exploit wetting properties of surfaces, and humanity tries to imitate this behavior to make use of it. In the case of animals, the water collecting properties of spider silk [43] can be mentioned. Other mechanisms originating from plants are also under consideration for water harvesting from humid air. For instance, it is attempted to imitate the *Sarraceni* trichrome by producing microchannels with different length scales [44]. A maybe more relevant example in every day's life is the Lotus effect [45] that can be found within advertising slogans for some wall paints. Other water repellent coatings are used in the clothing industry to increase the sales of rain jackets. And this even in two ways: When buying the jacket, the customer is pleased with its repellent effect and notices after some time that it has diminished considerably, which might tempt him or her to repurchase a jacket.

Usually substrates are characterized by their wettability. The new, water repellent rain jacket has a hydrophobic coating with a low contact angle hysteresis, which leads to a pearl-off of the rainwater. After a few months of wearing, it can be observed that the coating on the jacket disappeared on some areas. On these hydrophilic patches with higher contact angle hysteresis, the clothing material gets soaked with water and the rain jacket starts to lose its original purpose. While in the case of a rain jacket this effect is not desired, it is highly welcomed, and this is where we come back to the topic of printing and writing, in case of blotting paper, in which ink gets soaked up by a hydrophilic fiber network.

This chapter is about the modification of surfaces in order to achieve desired properties and its characterization with a focus on its wettability. Since the focus lies on flat surfaces with alternating hydrophilic and hydrophobic stripes as well as flat hydrophilic surfaces with a low contact angle hysteresis, only these topics are discussed. While in the latter case, hydrophilic means that the advancing contact angle is well below 90° , the terms hydrophilic and hydrophobic are applied less strictly in the case of the striped pattern surface. There, it simply means that the hydrophilic stripe has increased energy and, therefore, increased wettability compared to the hydrophobic one. The production of the striped patterned surfaces are discussed

in more detail in section 4.2, since an own chemical vapor deposition chamber was constructed, while the smooth hydrophilic substrates are described less extensively in section 4.3.

4.2 Chemically Patterned Substrates

One goal of the present work is to observe the stability and the breakup dynamics of sessile droplets on chemically patterned surfaces. Therefore, substrates are needed consisting of areas with different wettabilities, while the length scale of each area must be smaller than the diameter of the droplets so that a droplet wets more than just one area of a defined wettability. Stripewidths should be accomplishable in the order of $10\ \mu\text{m}$ - $1000\ \mu\text{m}$. The patterns should have a sharp boundary in wettability and the repeatability of the two-dimensional patterns must be guaranteed. I.e., a striped patterned structure with alternating hydrophilic and hydrophobic stripes as used in the studies of Bliznyuk et al. [46, 47, 48], Kooij et al. [49] and Jansen et al. [50, 51] is favored. Additionally, substrates must be transparent so that it is possible to observe a droplet and its contact line under an inverted microscope. The material should be readily available and the procedure should be manageable with the provided resources.

Since the substrate should be transparent, glass is favored as a basic substrate. Different methods are available to chemically micropattern this kind of material, including corona discharge [52], micro-contact printing [53, 54], and silanization from the liquid [55, 56, 57], or the gas phase [46, 58, 59] after photolithography steps. While with the corona discharge method, and microcontact printing, it is expected that there will be no sharp gradient in surface wettability, all other methods are most likely suitable for the present purpose. Additionally, microcontact printing is not considered because it is expected that the repeatability of the dimensions is not guaranteed. Furthermore, it includes photolithography and silanization steps that must be executed anyway when the latter two techniques are taken into account [53]. Therefore, it is an additional effort to micropattern the surfaces by microcontact printing compared with the silanization from the liquid or gas phase. These two techniques will be discussed later on. But first, the focus is on photolithography before the two silanization techniques are discussed in more detail.

4.2.1 Photolithography

Photolithography is a common technique in microsystem engineering and semiconductor technology. It is described in monographs such as [22, 60]. Though photolithography is performed externally by Klaus-Dieter Voss, it is indispensable for the substrate preparation in the present work. Therefore, all relevant steps are described in the present section.

First of all, the substrate on which the photolithography procedure is executed must be **cleaned** so that no dust or any organic layers adhere to it. Then, a layer of a photoresist with defined thickness can be applied on the surface. Usually, this is done by **spin coating**. In this process, the substrate is fixed on a chuck that can be rotated with speeds in the order of 100 - 10000 $1/\text{s}$. First, a defined volume of a photoresist is deposited in the middle of the substrate, and the chuck is set into motion with a defined angular speed ω , which depends on the viscosity η of the used photoresist. The value of ω can be found in any datasheet of

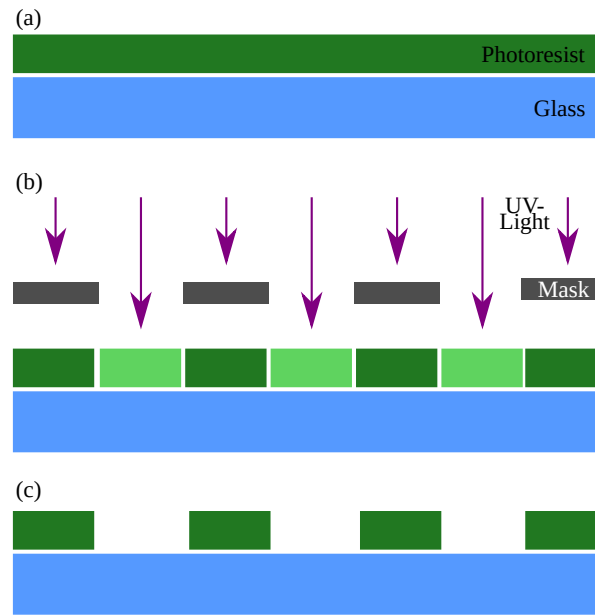


Figure 4.1: Sketch of photolithography steps when using a positive photoresist. In (a), the glass substrate is completely covered with the photoresist. In (b), a mask of the desired pattern is placed above the substrate inside of the illuminator, and the free parts are illuminated with UV-light. Exposed portions of the photoresist become soluble in a matching solvent. After a development step, not illuminated parts of the photoresist cover the substrate (positive photoresist).

a commercially available photoresist. The final film thickness h_f of the photoresist follows an empirical relation [22]

$$h_f \sim \left(\frac{\eta}{\omega^2} \right)^{1/3}. \quad (4.1)$$

Optionally, the last two steps can be exchanged. In this case, the photoresist is deposited with a syringe and a defined volume flow. In any case, the result of the spinning process is a uniform film of defined thickness on a substrate, as shown in figure 4.1(a). In order to evaporate all residual solvent inside the photoresist, the substrate is **soft baked** in a subsequent step inside of an oven or on a hot plate. This step is followed by the photoresist's **exposure** with UV-light for a photoresist specific time range and intensity. A photomask of the desired pattern is placed between the resist and the light source so that parts of the photoresist are illuminated, others not, as shown in figure 4.1(b). Subsequently, the substrate is taken out of the exposure device and usually again placed inside an oven or on a hotplate in the **post-exposure bake**. This step is not needed in the present case. The substrate is placed directly inside of a **development** bath. In the case of a positive photoresist (e.g., AZ 9260), the illuminated parts are dissolved in the solution. When a negative photoresist, such as SU-8, is used, illuminated areas stay on the substrate while the not illuminated parts are dissolved. Since for the present study a positive photoresist is used, the result of the development process can be illustrated as depicted in part (c) of figure 4.1. Lastly, the substrate is **rinsed** in a suitable liquid and **dried**, subsequently.

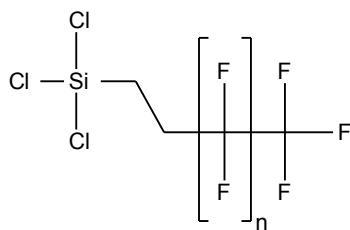


Figure 4.2: General chemical structure of perfluorinated trichlorosilanes.

4.2.2 Silanization

A common way to change (usually reduce) the energy of surfaces is silanization. In this process, a layer of silane molecules can be bonded to different kinds of surfaces. Since the focus lies on glass surfaces in the present study, only this kind of surface and very similar surfaces (concerning surface chemistry) such as the one of silicon wafers are discussed. Perfluorinated trichlorosilanes are used to functionalize the hydrophobic parts. The decision for this kind of silanes was made, since they are commonly described in the literature for hydrophobizing glass and silicon surfaces (e.g., [46, 51]), and the technical silanization process is well defined (see e.g., [58] for gas phase, or [57] for liquid phase deposition). Moreover, these molecules are highly hydrophobic due to their fluorinated chain, as depicted in figure 4.2 where the chemical structure of this kind of silanes is shown.

Trichlorosilanes of any kind consist of a head with a silicon (Si) atom surrounded by three chlorine atoms. In the case of perfluorinated trichlorosilanes, a tail as sketched in figure 4.2 is attached to the Si atom at the remaining free bond. This carbon (C) chain can have different lengths, which can be characterized by the number n of the $n + 1$ fluorinated C-atoms. In all cases, the first two C atoms have two terminating H-atoms, each. Due to the fluorinated end-group, the tail is hydrophobic, while the head is highly reactive. In the present study, two different trichlorosilanes are used, i.e., these are (3,3,3-Trifluoropropyl)trichlorosilane (abcr, Germany, CAS: 592-09-6) and 1H,1H,2H,2H-Perfluorodecyltrichlorosilane (abcr, Germany, CAS: 78560-44-8) which, from now on, will be abbreviated with TFPTS and PFDTs, respectively.

Chemistry In this subsection, the focus lies on the silanization reaction mechanism when the silanes, i.e., trichlorosilanes, react with surfaces. Trichlorosilanes are commonly used to hydrophobize glass or silicon surfaces. Jacob Sagiv performed detailed studies on the silanization reaction of trichlorosilanes and the subsequent surface chemistry of the forming layer in 1980 [55]. His studies were motivated by an observation by Bigelow et al., published in 1946, who found out that polar organic molecules form reversible, oleophobic monolayers by adsorption on solid surfaces [61]. Sagiv used information from Zisman [62] and others [63, 64] to suggest a reaction mechanism for trichlorosilanes, which is shown in an adopted version in figure 4.3.

In a first reaction (Rx 1), the functional group that is formed by the three terminating chlorine atoms (Cl) surrounding the silicon (Si) atom is hydrolyzed in a hydrolyzation reaction with water in which the Cl atoms are substituted by hydroxy groups (OH). As a side product, hydrochloric acid (HCl) is formed. The subsequent condensation reaction (Rx 2) does consist of two reactions. In reaction Rx 2.1, the hydrolyzed silane molecule is covalently bonded to the OH-groups of a substrate. Please note that the terminal

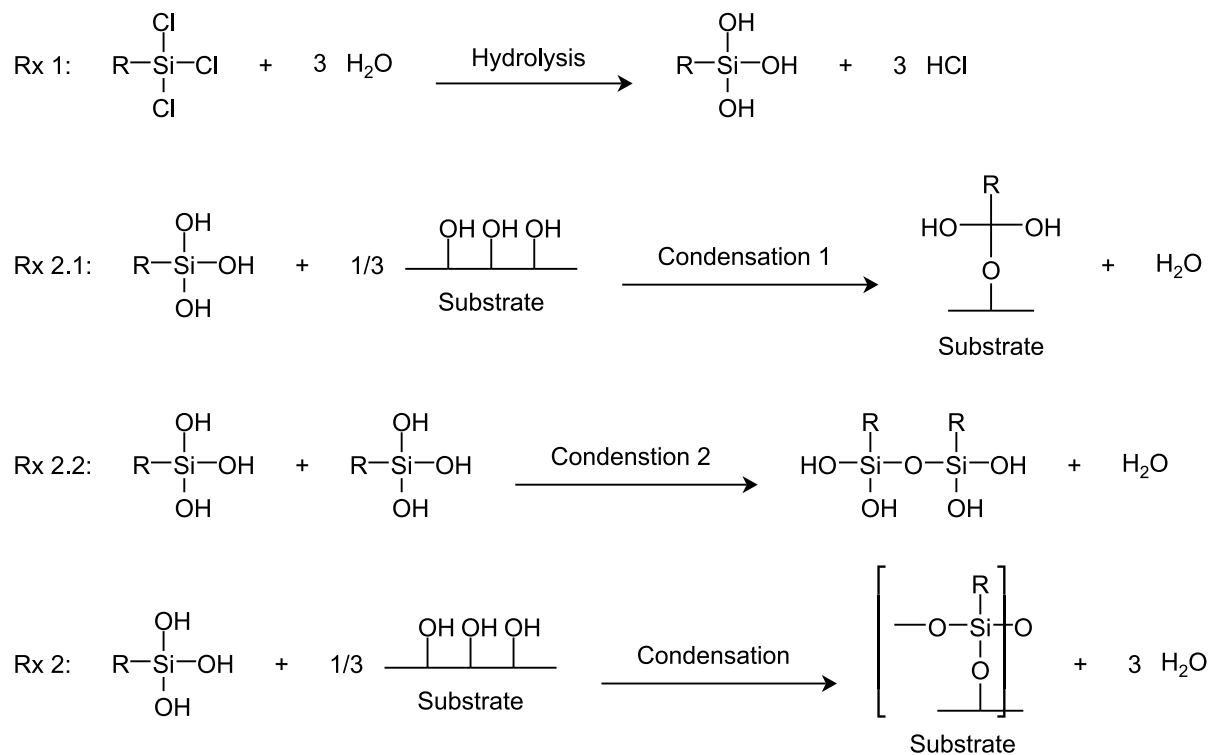


Figure 4.3: Sketch of the chemical reactions which lead to the silane monolayer on hydrolyzed substrates, adopted from [55].

OH-groups on the substrate are necessary for this reaction to occur. In the present case, glass substrates are used, which, similar to silicon substrates, can be activated in plasma to form these hydroxy groups. Reaction Rx 2.2 is shown to illustrate the linking of terminal hydroxy groups of the hydrolyzed silane molecule among each other. Rx 2 summarizes the two before described condensation reactions (note that Rx 2.2 occurs twice in Rx 2). The result of the described silanization process is a closed, covalently bonded monolayer of the used trichlorosilane on the substrate with the silane molecules being linked among each other.

Sagiv used n-octadecyltrichlorosilane $\text{C}_{18}\text{H}_{37}\text{SiCl}_3$ in his studies, i.e. $\text{R} = \text{C}_{18}\text{H}_{37}$, and silanization took place in a wet chemical process. Studies from other authors suggest that a monolayer is also formed in the case of perfluorinated trichlorosilanes, i.e., $\text{R} = \text{CF}_3(\text{CF}_2)_n\text{C}_2\text{H}_4$ and when deposition of the silane takes place from the vapor phase (see, e.g. [65, 66, 58]). Please also note that the above-presented reaction mechanism is an ideal picture of the situation. Other reactions between the hydroxy groups might occur, leading to vertical polymerization of the silane molecules. Furthermore, it might also be that more than only one hydroxy molecule from the silane molecule is covalently bonded to the substrate [67]. Nevertheless, these problems can be overcome by using the right silanization technique [59]. In the following section, the focus lies on these different methods for silanization.

Comparison between Relevant Silanization Techniques As described previously, two suitable silanization techniques are identified to chemically pattern glass surfaces: deposition from the liquid and deposition from the gas phase. The latter is called chemical vapor deposition (CVD) in the following. Additionally, in the case of CVD techniques, it is differentiated between deposition at low pressures (LP) and

atmospheric pressures (AP) (or pressures close to it). In the case of liquid phase silanization techniques, trichlorosilanes are diluted in a solution containing chemicals such as chloroform, carbon tetrachloride, and n-hexadecane [55], dodecane [56] or bicyclohexyl [57]. In a subsequent step, cleaned substrates are placed inside this solution for a certain amount of time. In [57], the authors included a table with more examples of used solvents, silanization time, and also pre- and post-silanization cleaning techniques employed in other studies. If the deposition is taken out from the vapor phase, the substrate is placed inside of a vessel. At atmospheric pressures (AP-CVD), a small, open container such as a small petri dish is placed in the vessel with the substrate. The silane evaporates and reacts with the substrate surface. Note that within this classification logic also techniques that include vessels in which the pressure can slightly be reduced by a membrane pump, such as dessicators or vacuum ovens, belong to AP-CVD. In case of low pressure (LP-CVD), the substrate is placed inside a vacuum chamber, which is subsequently evacuated by a vacuum pump until pressures in the range of fine vacuum (10^{-3} mbar) or even lower are reached. The silane is placed inside a vessel separated by a valve from the vacuum chamber [58]. When a defined end pressure is reached, the silanization process is started by opening the valve. The silane then evaporates into the chamber. Some more sophisticated devices have the ability to heat the substrate, control the flow rate of silane or activate the surface within the device [58, 68, 69].

Most of the advantages and disadvantages can be directly derived from the description of the processes. An attempt is made to compare the relevant methods in table 4.1. While in liquid phase processes, a lot of different, potentially unhealthy, and in other ways dangerous solvents must be used, this is not the case in both CVD-processes. Furthermore, especially when microstructured surfaces should be silanized after photolithography, it must be ensured that the compatibility between photoresist and solvent is guaranteed. Nevertheless, Brasjen et al. [56] show that this is possible when chemicals are combined correctly. Another aspect is the precursor usage, i.e., the amount of silane used, which tends to be less in vapor phase deposition methods than in wet chemical processes. The quality of the coating can be judged by the coating uniformity and the control of its thickness. According to Fadeev and Carthy [67] and Wang et al. [70], the layer's uniformity from the CVD process is superior compared to wet chemical processes. While in LP-CVD monolayers can be produced, non-uniform layers are deposited from solvent-based methods. According to Psarski et al. [59], the uniformity of monolayers and hence the control of the coating thickness increases with the chain length of the fluorinated trichlorosilanes since cross-linking between the molecules is reduced. Cross-linking can also happen in solution and during long reaction time, as it is the case in AP-CVD (up to 24 h) due to uncontrolled humidity in the lab environment, which might affect the quality

Table 4.1: Comparison of three different silanization techniques from the liquid phase (wet chemical) and the gaseous phase at low (LP-CVD) and atmospheric pressures (AP-CVD). The scale reaches from -- for very bad over - to 0 for neutral and + to ++ for superior.

Criteria	wet chemical	LP-CVD	AP-CVD
Solventless	--	++	++
Precursor usage	0	++	+
coating uniformity	0	++	+
control of coating thickness	-	++	+
environmental vulnerability	-	+	--
structures with high aspect ratio	-	++	++
effort	+	--	++
deposition rates	++	-	--
throughput	++	-	--

of the silane layer. Nevertheless, also wet chemical protocols have been reported in which a uniform monolayer is formed [57]. When structures with high aspect ratios should be coated, the CVD methods' superiority is evident since the vapor can reach every point of the substrates, especially in the case of small structures in the range of 1 μm or smaller. Solvent-based methods are limited due to the capillary lengths of the solvents which might prevent the solution from penetrating into small structures. The effort that has to be put in each method shows another picture of the situation. A LP-CVD reactor is a unique construction from suitable vacuum parts, at least a rotary vane vacuum pump and other parts such as different valves and specially constructed pipelines. Silanization in AP-CVD and from solution in their most simple versions only require a few vessels and containers and a fume hood. An advantage of the wet chemical silanization over both CVD methods is higher deposition rates and, consequently, increased throughput of substrates.

Since high throughput and the deposition rate in the order of a few minutes are not relevant in the present case and the focus is mostly on a uniform, well-defined monolayer on substrates with structures going down to the order of a few μm , a decision for a LP-CVD reactor was made and constructed subsequently. Moreover, this has the advantage that a broader range of photoresist can be used during micropatterning, which might become necessary in other projects than the present one. The realization of the chemical vapor deposition at low pressures is presented in the following subsection.

Realization of the Chemical Vapor Deposition The CVD chamber that was developed in the present work was constructed to match the conditions of Mayer et al. [58]. In their work, the authors used Trichloroperfluorosilanes for surface modification and additionally were able to produce substrates with repeatable quality, i.e., the monolayer on their glass and silicon substrates is closed. This is generally important because it prevents chemical inhomogeneities which do affect the wetting behavior of liquids on these surfaces. Thus the possibility of unwanted pinning events of liquid on the surface is decreased. In the following part, the process itself is presented before it is focused on some constructional details.

Figure 4.4(a) shows a sketch of the process. Substrates can be inserted inside of a vacuum chamber. After the chamber is closed, it can be evacuated by a vacuum pump by opening valve V4. During this process, valves V1, V2, and V3 are closed. When a defined pressure p_{start} is reached, V4 is closed, and V1, which separates a silane containing precursor cylinder from the chamber, is opened. The silane evaporates into the vacuum chamber, and the pressure inside of it increases. When a defined pressure p_{silane} is reached, V1 is closed, and, depending on the used silane, V2 is opened so that water can enter the reaction chamber. According to Rx 1 in figure 4.3, water is necessary to initiate the silanization reaction. Moreover, it stabilizes the final monolayer [58]. The valve is kept open until again a particular pressure $p_{\text{H}_2\text{O}}$ is reached. Then V2 is being closed again, and the silanization takes place within a defined reaction time t_{react} . In a final step, the chamber is vented by opening V3 and the substrates can be taken out of the chamber. All relevant process parameters of the used silanes are presented in section 4.2.3.

The silanization reaction in [58] takes place at pressures in the order of 1 mbar. Therefore it is necessary that the vacuum chamber can be evacuated to fine vacuum, which is the pressure range between $1 \cdot 10^{-3}$ mbar to 1 mbar. Consequently, all parts belonging to the vacuum chamber must be connected with appropriate connectors, and a vacuum pump with an end pressure below the reaction pressure aimed to be used. By using KF-vacuum-flanges (VAb, Germany) and crimped connections (Swagelok, USA), all parts are properly connected. A double rotary vane pump (Duo 1.6, Pfeiffer Vacuum, Germany) with an end pressure of $3 \cdot 10^{-3}$ mbar ensures a fine vacuum in the chamber.

A second requirement that must be fulfilled is a direct result from Rx 1 in Figure 4.3. Since HCl is

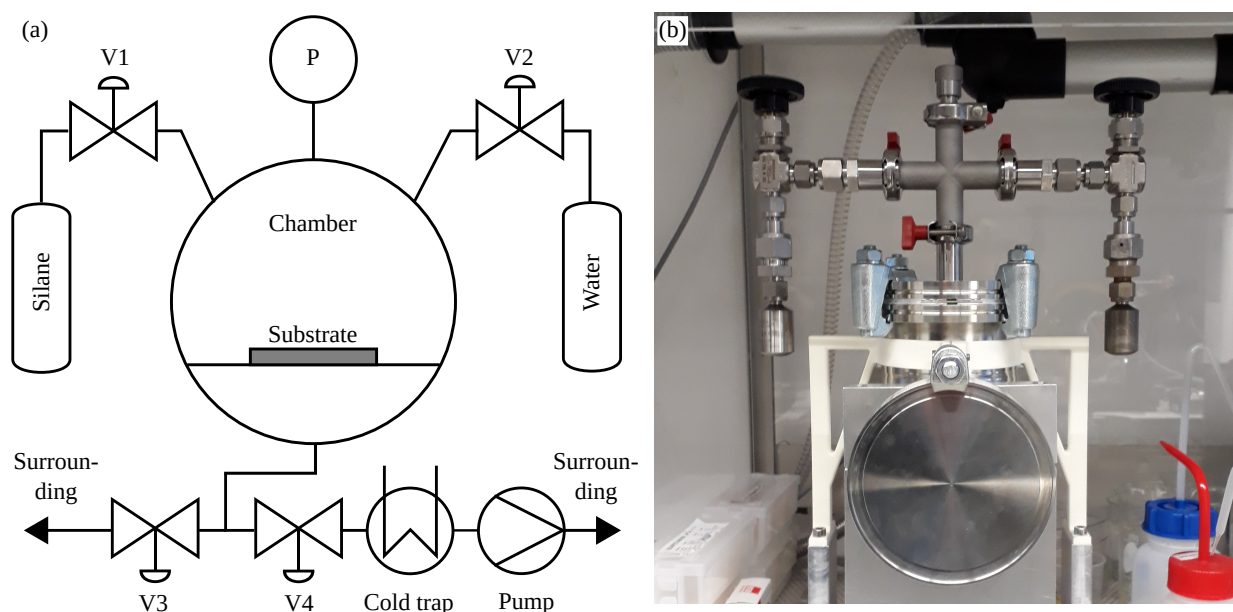


Figure 4.4: (a) Schematics of the CVD-chamber: It can be evacuated by a double rotary vane pump (Pump). The chamber is separated from the pump by a valve (V4) and can be vented by another valve (V3). The pressure is measured inside the chamber (P). Two precursors (silane and water) can evaporate into the evacuated chamber by opening a valve (V1) and (V2) (each precursor by its valve). (b) shows the reaction chamber's realization with two precursor cylinders (left and right arm) and the venting valve (top). Substrates can be entered inside of the chamber from the front.

produced during hydrolysis, all parts in contact with the reaction gases must be able to withstand a corrosive atmosphere or be suitably protected from it. Therefore metallic parts fabricated from stainless steel 1.4306/304L are used wherever it is available. Furthermore, the gaskets used between the KF-flanges of the vacuum parts (VAb, Germany) are made out of Viton. The pressure inside of the chamber is measured with a Pirani vacuum sensor (VCP63MV, Thyracont, Germany) that determines the heat conduction inside of a known gas. From this, the pressure can be calculated which is shown on an external device (VD12S2, Thyracont, Germany). The heated filament inside the Pirani sensor, which serves as the heat source for the heat conduction measurement, is made out of platinum and rhodium to prevent any damage and, hence, to assure a correct determination of the pressure. Finally, a nitrogen cold trap (Pfeiffer Vacuum, Germany) is placed between the vacuum chamber and the vacuum pump. Though the reaction gases are not pumped directly, even small amounts of HCl can damage the vacuum pump. Therefore the cold trap is needed in which small amounts of the reaction gases do condense and can subsequently be removed from the process. As a positive side effect, the pumped gas density increases with decreasing temperature, and hence the pumping efficiency does increase. Moreover, the cold trap serves as a vapor barrier for oil vapor coming from the vacuum pump, which could affect the surface chemistry of the substrate. The oil inside the vacuum pump is exchanged regularly to prevent corrosion inside of the pump.

Other vital parts used in the silanization reactor are precursor cylinders and the valves V1 and V2 with its appropriate pipelines (Swagelock, USA). In particular, needle valves are used which do assure a precise dosing of the precursors.

4.2.3 Used Material and Substrate Preparation

To be able to produce the chemically micropatterned substrates repeatably, the following protocol is established. The first step in photolithography is the rinsing of the substrates. Therefore the used 2"-borofloat33-wafers (Siegert Wafer, Germany) are first rinsed with acetone, then with isopropanol for 1 min in each solution. Next, the wafers are dried on a hotplate at 130 °C for 15 min before the positive photoresist AZ 9260 (Microchemicals, Germany) is spin-coated onto the wafers according to the parameters of its datasheet. The resulting thickness of the photoresist is $\sim 7 \mu\text{m}$. After the soft bake step in which the substrates are placed inside of an oven at 100 °C for 7.5 min, the substrates with the corresponding photoresist are illuminated inside the mask aligner MA56 M (SÜSS MicroTec, Germany), and the photoresist is exposed for 350 s at a wavelength of 365 nm using an appropriate mask. The substrate with the illuminated photoresist is then developed inside a mixture of DI-water and the developer AZ 400k (Microchemicals, Germany) ($\text{H}_2\text{O}:\text{AZ 400k} = 4:1 \text{ vol}\%$) for 3.5 - 4 min. Then it is rinsed in DI-water and subsequently dried in an airflow. This whole process leads to uncovered parts, and areas of the glass surface covered with photoresist. The pattern is defined by the corresponding mask. In the present case, only striped patterns are used. The substrates are then packed in an appropriate box and subsequently laminated so that they can be transported. All before mentioned steps of photolithography are performed within a cleanroom environment.

The substrates are stored within the laminated box until they are needed. When this is the case, they are placed inside a plasma chamber (FEM TO, Diener, Germany). After evacuation of the chamber for 2 min with a membrane vacuum pump (EN-8T, Nidec, Japan), the surface is treated within oxygen plasma for 30 s at 100 W with oxygen from an oxygen source (KröberO2, Kröber Medizintechnik GmbH, Germany) at a flow rate of 35 ccm/min. This has two effects: Firstly, the uncovered glass areas are cleaned, and all organic residues on it are removed. Secondly, the glass surface is activated, i.e., OH-groups are produced on the surface, which are necessary to silanize the surface successfully (see Rx1 in figure 4.3). The substrates are taken out of the plasma chamber and then placed inside the CVD-chamber which is then evacuated until the pressure p_{start} is reached. Then the procedure according to section 4.2.2 is executed. All relevant process parameters for the two different silanes used can be read from table 4.2. The silanization process is stopped by venting the chamber and taking out the substrates. In a subsequent step, the photoresist is rinsed off with acetone and then cleaned in an ultrasonic bath filled with acetone for 10 min at room temperature to remove any remaining traces of the photoresist from the surface. Finally, the substrate is rinsed with isopropanol, blown dry with nitrogen, and stored inside a wafer box. It was taken care of that experiments are performed maximum 5 d after the substrates were produced. Note that also tests with (Tridecafluoro-1,1,2,2-tetrahydrooctyl)trichlorosilane (FOTS, abcr, Germany, CAS: 78560-45-9) were performed successfully. In that case the same process parameters as with PFDTs can be applied [58].

Table 4.2: Process parameters for two different silanes.

Silane	CAS	p_{start} (mbar)	p_{silane} (mbar)	$p_{\text{H}_2\text{O}}$ (mbar)	t_{react} (min)	source
PFDTs	78560-44-8	$5 \cdot 10^{-3}$	$2 \cdot 10^{-1}$	1	30	[58]
TFPTs	592-09-6	$5 \cdot 10^{-3}$	1.2 – 1.6	-	60	[66]

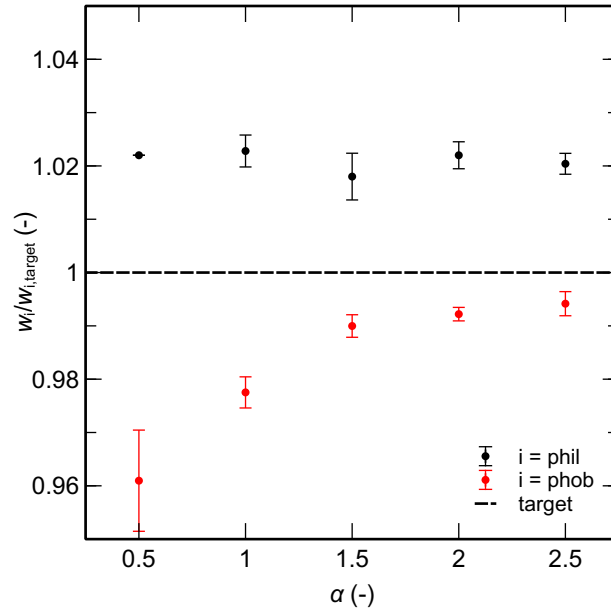


Figure 4.5: Dimensionless width from different parameters α and w_{phil} . The target width $w_{i,\text{target}}$ is the desired width of the hydrophilic or the hydrophobic stripe. The error bars represent the standard deviation from five different stripes.

4.2.4 Characterization

Stripewidth After all photolithographic steps are performed, a glass substrate consists of glass stripes covered with a photoresist and those that are uncovered. The uncovered glass areas will be exposed to the silane atmosphere in a subsequent step and become hydrophobic after this treatment. Their stripe width is therefore denoted with w_{phob} . The covered stripes are protected from the silane, stay hydrophilic, and are denoted with w_{phil} . In accordance with literature (Bliznyuk et al. [46] were the first ones who did that) a parameter

$$\alpha = \frac{w_{\text{phob}}}{w_{\text{phil}}}, \quad (4.2)$$

the ratio between the hydrophobic and the hydrophilic stripe width, is defined.

The stripe width of the covered and uncovered glass areas is measured under an inverted microscope to judge the quality of the photolithography. The results are shown in figure 4.5. w_i is divided by $w_{i,\text{target}}$. It can be seen that the hydrophilic stripe width is about 2% larger than the desired stripe width while w_{phob} is smaller. From figure 4.5 it seems like the quality of the hydrophobic stripe width for larger α is better and the error, i.e. the deviation from the dimensionless target width 1, decreases. This is true for the relative error. However, the absolute error in stripe width is as the one of the hydrophilic stripe with an opposite sign, as is to be expected. During the photolithography steps, the light scattering, as well as the development of the photoresist after it has been illuminated may lead to these small deviations from the pattern of the mask. Since the error is regular, it probably has its origin in the light scattering during illumination. However, the stripe width quality can be regarded as very good since the error made is about 2% of the (constant) hydrophilic stripe width.

Monolayer and Roughness To have repeatable wetting properties of the substrate, a closed monolayer of silane is desired. By measuring the film thickness and comparing it to the respective silane length, it can be judged if a silane monolayer or a multilayer has formed on top of the carrier substrate. A way to measure the thickness of thin layers is ellipsometry. Without going further into detail, the measurement principle is as follows: Polarized light is emitted by a polarisator and sent onto a substrate under an incidence angle smaller than 90° where it is reflected and the direction of polarization of the light is changed. This change of polarization can be detected by the analyzer, which, in general, is a second polarizer which's direction is turned until no light can pass. This is detected by a detector. The collected data can then be analyzed by fitting the data with an appropriate model. The reader is referred to textbooks such as [71] for further information on ellipsometry.

In the present case, the 0-ellipsometer Nanofilm EP3-SE (Accurion, Germany) with a continuous wave diode laser of wavelength 658 nm at an inclination angle between 40° and 68° and the evaluation software from the manufacturer was used. Since a flat, reflective surface with low roughness is needed for analyzing the monolayer, silicon wafers are silanized with PFDTS following the above-described protocol. Note that a homogeneous silane layer was applied, instead of a striped pattern. The surface chemistry of silicon is very similar to the one of glass and therefore it is expected that it behaves the same compared to glass when it is silanized.

First, ellipsometric measurements of a bare silicon surface were performed. Then the same measurements with the silanized silicon surface were executed. These measurements were compared to subtract the bare silicon surface's influence and the data was fitted with the software intern *Polymer*-model. As an input parameter, the refractive index of PFDTS $n_{\text{PFDTS}} = 1.3485$ was set [72]. This allowed to determine the thickness of the layer to be $1.73 \text{ nm} \pm 0.10 \text{ nm}$. The determined value suits well with the layer thickness measured in other studies ($1.6 \pm 0.1 \text{ nm}$ in [73], or $\sim 1.4 \text{ nm}$ in [74]).

The roughness of a homogeneously silanized glass substrate was validated using Atomic-Force measurements. At three different wafers, it was always well below 1.2 nm, which is the surface roughness as quoted by the glass wafer supplier (Siegert Wafer, Germany).

Contact Angles of Evaporating Droplets To quantify the wetting behavior of water droplets on the used substrates, contact angle measurements of evaporating droplets on these surfaces were performed. Within these experiments, for each surface, seven individual DI-water droplets were sequentially placed on a freshly prepared, pristine substrate using a needle connected via a tube with a syringe in a syringe pump. More details can be found in section 3.1.2. The initial volume of each droplet was $1 \mu\text{l}$ and the flowrate was $0.1 \mu\text{l/s}$. The climate chamber setup, as described in section 3.1.1, was used to ensure a constant humidity H and temperature T within these experiments ($H = 25 \text{ \%rh}$, $T = 25 \text{ }^\circ\text{C}$). Only side view images were taken. Evaluation of the image data was performed with the software presented in [36]. The data is then averaged over seven experiments for each substrate in both the contact angle Θ and the base diameter d of the droplet, and then binned over an interval of $0.01 \cdot t/t_{\text{evap}}$, where t is the time and t_{evap} the total evaporation time range, by a self-written evaluation software.

Results for the dimensionless time evolution t/t_{evap} of Θ are shown in figure 4.6(a), while the corresponding base diameter d is depicted in figure 4.6(b). The first data point for each surface in (a) and in (b) represent the average of a droplet that is pumped up, i.e., the contact line is in an advancing state. Therefore, the maximum value in figure 4.6(a) represents the advancing contact angle Θ_{adv} for water on each substrate. After the needle is pulled out of the droplet, evaporation leads to decreased droplet volume. In an initial

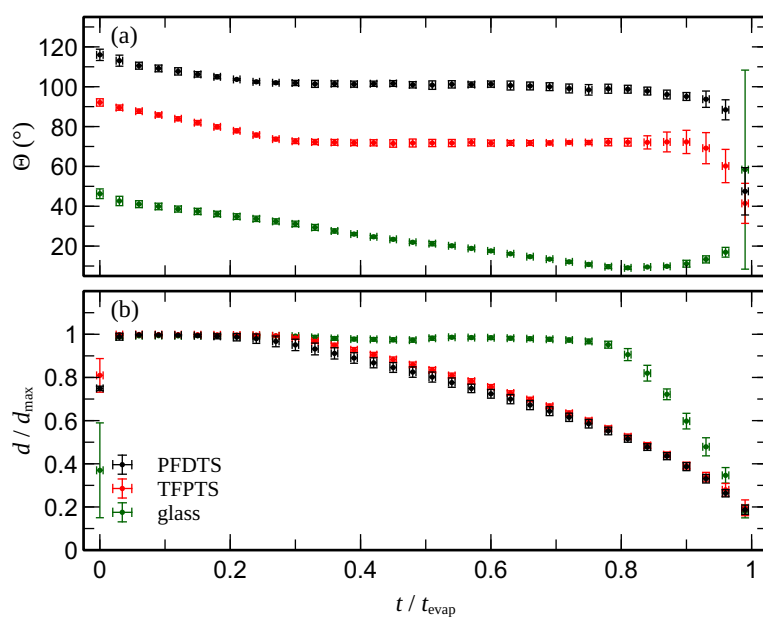


Figure 4.6: Contact angle (a) and dimensionless diameter (b) of evaporating water droplets on three different surfaces PFDTs, TFPTs, and glass as a function of the dimensionless evaporation time. Reprinted (adapted) with permission from the supplementary material of [75]. Copyright 2019 American Chemical Society.

evaporation stage, the contact angle decreases, while the base diameter, and therefore the base radius that is also called contact radius, stays constant. This evaporation mode is called the constant contact radius (CCR) mode. This stage is followed by a time range within which the base diameter decreases while the contact angle stays constant. Therefore evaporation in this time range happens in a mode that is called constant contact angle (CCA) mode. Since the contact line is in a receding state during CCA mode, this contact angle is interpreted as the receding contact angle Θ_{rec} of a water droplet on the appropriate substrate. The final stage of evaporation is neither a CCR nor a CCA mode but something that, according to literature, is called the mixed mode [76, 77, 78, 79, 80]. Radius and contact angle decrease simultaneously. In literature it is debated about the causes of this mixed mode. While Bourges-Monnier and Shannahan [76] and Cazabat and Guéna [79] think that this phenomenon is due to surface heterogeneities that do become important for decreasing contact radii, Bormashenko et al. [78] are of the opinion that the precursor film that forms during evaporation affects the contact angle. Kim et al. [77] and Park et al. [80] showed that unavoidable contaminants also play a role. This debate is still ongoing within a small community. Probably the truth contains all the above-mentioned reasons. For the present work, this effect might be important but is not investigated in more detail. The slight increase of the contact angle during the last stage of water on the bare glass surface is due to measurement errors in the automated evaluation of the droplet that is a result from a combination of the difficulty in measurement of small contact angles in combination with a short contact radius and the automated evaluation of the contact line.

Corresponding advancing and receding contact angles of deionized water on the investigated substrates are summarized in table 4.3. These results confirm the statements cited before that the contact angle increases with an increasing chain length of the adsorbed fatty acids and silanes at the surface [61, 62, 55, 59]. The measured contact angles on PFDTs and TFPTs silanized surfaces correspond well with values from literature [58, 66, 59] which indicates that the used silanization technique is reliably working and

the quality of the silane layer is adequate for the present purpose.

Problems While the wettability of the silanized areas can always be reproducibly produced, this is not the case for the hydrophilic part. Depending on the time between the opening of a fresh package of wafers and its production, the contact angle on the hydrophilic stripe changed, though this was in the range of about 10° . It was tried to establish a standardized protocol with plasma cleaning prior to the photolithography steps and defined time intervals between all steps leading to the striped pattern. Nevertheless, differences in contact angle between different substrates could be detected depending, for instance, on the humidity. Moreover, when the surface is plasma cleaned before photolithography, the removal of the photoresist after CVD is not achievable without remaining residues. When the wetting behavior on the hydrophilic stripe is of importance, i.e., in chapter 6, this problem is accounted for by measuring the corresponding contact angles and the wetted length on the hydrophilic stripe.

4.3 Hydrophilic Substrates with Low Contact Angle Hysteresis

One goal of the present work is to observe and investigate the forming and structure of a liquid bridge between an electrode and an aqueous droplet. Since the influence of the three-phase contact line is of central interest, hydrophilic substrates with an advancing contact angle $\Theta_{\text{adv}} < 90^\circ$ are required. On the other hand, lateral adhesion forces between the droplet and the substrate should be as small as possible so that the forces and, therefore, the applied potential between the droplet and the electrode is minimized. Therefore, and in addition to the hydrophilic nature of the solid-liquid combination, substrates with a low contact angle hysteresis $\Delta\Theta$ are needed.

However, this is not trivial, since, in general, low contact angle hysteresis is associated with hydrophobic surfaces. The probably most prominent examples exploit the Lotus effect and are often termed as superhydrophobic surfaces, see e.g., [81, 82], among others. Typical static contact angles of water on this kind of surfaces are around or above 150° and the contact angle hysteresis is below 5° . While the Lotus effect uses *dry*, solid surfaces, another way to achieve low contact angle hysteresis substrates is to apply an additional liquid layer, most often this is a silicon oil, between the substrate and the water droplet. When the silicon oil is held inside the structure of the substrate, e.g., a micropillar array, these surfaces are called liquid-infused surfaces or slippery lubricant-infused surfaces (SLIPS) [83, 84, 85]. But also flat, slippery surfaces exist on which a layer of silicon oil is burned-in, and another silicon oil is spread on top of this layer [86]. Typical static contact angles of water on slippery surfaces, assuming that ordinary silicon oil is used as a lubricant, are around $\sim 100^\circ$, and the contact angle hysteresis is approximately 2.5° - 5° .

The range of literature that can be found when searching for low contact angle hysteresis and simultaneously small static water contact angles below 90° is, however, very limited. To the best knowledge of

Table 4.3: Advancing and receding contact angles of DI-water droplets on used surfaces.

Surface	Θ_{adv} ($^\circ$)	Θ_{rec} ($^\circ$)
PFDTS	120	102
TFPTS	94	72
Glass	49	12

the author, only two appropriate methods could be found. The first one is the same as the slippery surfaces presented above, but different lubricants are used. While Dai et al. used trimethoxysilane as the lubricant on an etched copper surface [87], hydroxy-terminated polydimethylsiloxane (PDMS) is taken by Guo et al. [88]. Trimethoxysilane cannot be used in the present case due to its acute toxicity within the open experimental setup. Hydroxy-terminated PDMS, however, is applicable, and tests with it were performed, which confirmed the measured contact angles of Guo et al. of about 76° with a contact angle hysteresis of about 5° , though the method was adopted to the one of Eifert et al. [86]. However, cloaking, i.e., a film of the lubricant pulling over the water droplet, could be observed in all of the experiments leading to a quite complex system in which the effect on the three-phase contact line cannot be distinguished from other influences. Moreover, in a later stage of the project, the focus will be on droplet coalescence. Since cloaking also influences (non-)coalescence of sessile droplets, lubrication films or SLIPS cannot be used in general in the present problem [89]. In May 2019, Kaneko et al. [90] published the second method. This paper reports that when a tetraethoxysilane-trimethoxysilane mixture is spin-coated onto a glass or silicon slide and then dried in an oven, a solid sol-gel layer forms on the substrate which has both, contact angles well below 90° and a small contact angle hysteresis slightly larger than 5° . Though here a trimethoxysilane is used too, this is not problematic since the substrate preparation can be performed within a fume hood, and in a solid state it is not a danger for the experimenter anymore. The preparation and characterization of the substrate is presented below.

4.3.1 Used Material and Substrate Preparation

Substrates were prepared by applying the protocol of Kaneko et al. [90] for the present purpose. As the carrier substrates, microscopy glass slides ($76\text{ mm} \times 26\text{ mm}$, Carl Roth, Germany) were used. The used chemicals for the solvent solution were ethanol (Ethanol denatured $\geq 99.8\%$, Carl Roth, Germany), deionized (DI) water from a Millipore device (Milli-Q, $18.2\text{ M}\Omega\cdot\text{cm}$), and hydrochloric acid (HCl, $36.5\text{-}38.0\%$, Sigma-Aldrich, USA, CAS: 7647-01-0). The main components of the final solution with which the wetting properties can be controlled are tetraethoxysilane (TEOS, abcr, Germany, CAS: 78-10-4) and 2-[Methoxy (ethyleneoxy)10 propyl]trimethoxysilane (Dynasytan 4148, Evonik, Germany), which is also abbreviated as PEG-M in the following.

In the first step, a solution of the five before-mentioned liquids is mixed using the volume ratio PEG-M : TEOS : water : ethanol : HCl = $8.7 : 22.1 : 180 : 180 : 0.05$. This is accomplished by first mixing the solvent solution consisting of water, ethanol, and HCl in this order within a beaker while stirring. Subsequently, PEG-M and TEOS are added. According to [90], the minimum contact angle hysteresis is measured using the molar ratio of $[\text{PEG-M}]/[\text{TEOS}] = 0.15$, resulting in the above-mentioned volume ratio. Note that also other molar ratios are tested in substrate characterization experiments. In the experiments presented in chapter 7, however, only substrates with the molar ratio $[\text{PEG-M}]/[\text{TEOS}] = 0.15$ are used. This solution is stirred for at least 24 h. Before coating the carrier substrates with the solution, it must be cleaned thoroughly. Therefore, substrates are treated within a ultrasonic bath for 10 min using acetone as the solvent. These substrates are then taken out of the acetone bath, rinsed with DI water and blown dry in a nitrogen stream. Subsequently, the substrates are plasma cleaned within an oxygen plasma (plasma chamber: Femto, Diener Electronic, Germany; oxygen supply: KröberO2, Kröber Medizintechnik, Germany) using an oxygen flow rate of 25 ccm/min at 120 W for 1 min, after the chamber has been evacuated for 1 min with a membrane vacuum pump (EN-8T, Nidec, Japan). This step is not described in [90], but own tests showed that though it does not influence the final contact angle, it has a significant influence on the film uniformity of the coated layer on the final substrate. This is due to an increased surface wettability of

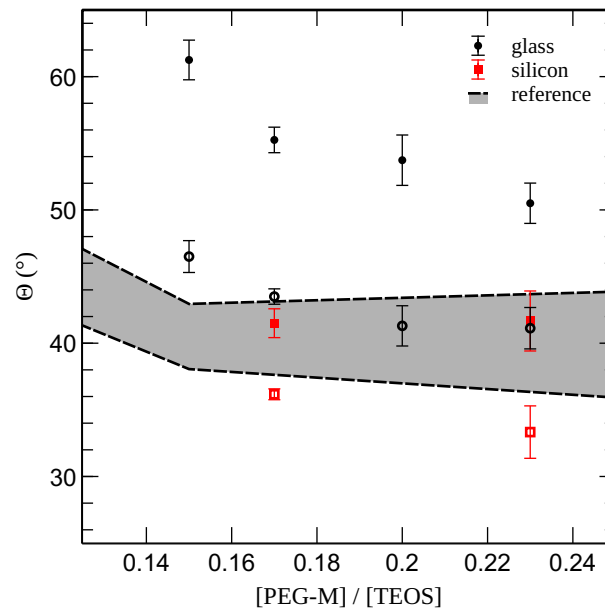


Figure 4.7: Measured water contact angles (mean values and standard deviations) versus contact angles from Kaneko et al. [90] (dotted lines show advancing and receding angles, respectively). In the case of own measurements, two different carrier substrates are tested (glass and silicon). Empty symbols show receding, and solid ones advancing contact angles.

the solution in the subsequent spin coating step. In this step, the cleaned substrate is placed onto the spin coater's chuck, and the PEG-M/TEOS solution is evenly spread onto the substrate with a disposal pipette, until it is completely covered. The substrate is then spun at 1000 rpm for 50 s at room temperature in ambient air using the smallest possible acceleration. Then the samples are dried in an oven at 80 °C for 3 h. Finally, the substrates are rinsed with DI water, blown dry with nitrogen, and stored until experiments are performed.

4.3.2 Characterization

The results of the contact angle measurements of DI water droplets on the substrates prepared with the protocol above can be found in figure 4.7. Contact angle measurements were performed with a DSA 100 (Krüss, Germany) by inflating a droplet through a needle with a flow rate of 0.25 $\mu\text{l/s}$ until the final volume of 2.5 μl was reached. Since the volume of the droplet was chosen to be small, the influence of gravity can be neglected due to Bond numbers well below 1. While the contact line progresses, the advancing contact angle Θ_{adv} was measured using the software Advanced Elements (Krüss, Germany). The tangent method was chosen to extract the contact angle. By deflating the droplet with the same flow rate as above, the receding contact angle Θ_{rec} was measured in the same manner while the contact line was receding. Additionally to own measurements, the original results from Kaneko et al. [90] are depicted. However, note that the contact angles in [90] were measured on water droplets sliding down an inclined surface. There, the volume of the droplet was 50 μl , and therefore gravity has a significant influence on the shape of the droplet.

The absolute values of Θ_{adv} and Θ_{rec} and the contact angle hysteresis $\Delta\Theta$ are larger in own measurements, in the case of glass as a carrier substrate, compared to literature values. Since different measurement techniques are used (own measurements versus literature) and additionally, entirely different droplet volumes are compared, a first attempt to explain the differences in contact angles is to blame it on these two factors. Tests with silicon wafers as carrier substrates were performed to exclude any mistakes that might have happened during the preparation of the solution at two different molar fractions of PEG-M and TEOS. These solutions were the same as the ones that were spin-coated onto the glass substrates. The contact angles measured on the surfaces using silicon wafers as a carrier substrate confirm the measurements of Kaneko et al. [90]. It therefore can be concluded that the carrier substrate itself has a significant influence on the quality of the layer and, hence, on the wetting behavior. Though the contact angle hysteresis of the sol-gel layer on the silicon surface is lower than the one on the glass surface, silicon wafers cannot be used as a carrier substrate because it is electrically conductive. This could also be seen in own tests, in which electrolysis was observable at an electrically connected water droplet sitting on this kind of surface after an electric potential has been applied between the substrate itself and the droplet. Nevertheless, the contact angle hysteresis $\Delta\Theta$ of DI water droplets on the PEG-M - TEOS treated glass slides, at different molar ratios between PEG-M and TEOS, is $\Delta\Theta \approx 10^\circ$. This is about 75% smaller than on an untreated glass surface. Moreover, the advancing contact angle is always well below 90° . Therefore, the sol-gel surface prepared on the used glass slides fulfills the requirements described above.

5 Stability of Droplets on Chemically Patterned Surfaces

Most of this chapter is published in Hartmann and Hardt 2019 [75]. Cora Despot performed some of the experiments. In his function as my supervisor, Steffen Hardt, gave valuable input during the whole process of this project.

5.1 Introduction

In chapter 1, it was shown that without capillarity and wetting, writing, printing, and the transport of information in the (physically) written form could have never been developed in the way we know it. Fortunately, humankind has learned to use these effects and further develop printing processes to benefit from it. In recent years, printing technologies have been developed which use pre-patterned, flexible webs within a continuous coating process to direct ink towards hydrophilic areas [6]. But also in discontinuous inkjet printing processes, chemically inhomogeneous surfaces can be beneficial. For instance, pre-defined hydrophobic regions can be used to repel droplets that do emerge from an inkjet nozzle. Due to their impact velocity, this can lead to splitting of these drops [91, 92, 93]. A review by Kuang et al. [94] gives an overview of this topic with a particular focus on inkjet printed dots and lines. The above-mentioned examples deal with pre-patterned substrates in printing technology. However, chemically heterogeneous surfaces can emerge from the printing process itself and significantly influence it. For instance, this is the case in multilayer inkjet printing in which multiple ink layers are printed on top of each other. Printed electronics [95, 96, 97], solar panels [98], or fuel cells [99] can be produced with this printing technology. It is easy to imagine that with such small dimensions, such as those found in these products and which are in the order of the droplet diameters, there is an influence on the printed image and, in this case, on the functionality of the printed products.

Chemically striped patterned surfaces can not only be applied in printing technology. It also could be used in biomedical devices and microfluidic applications. Xia et al. [100] summarized these and other potential applications in their review. The papers by Bliznyuk et al. and Kooij et al. [46, 48, 49] sketch an idea, how chemically stripe patterns could be used in microfluidics. In [46], the authors produced substrates with alternating hydrophobic and hydrophilic stripes with different stripe width ratios $w_{\text{phob}}/w_{\text{phil}}$ and called this ratio α . For the key finding of this publication, Cassie's law [101] is exploited, which states that the effective contact angle of a droplet wetting a surface with a pattern much smaller than the droplet can be modeled as a function of the areas with different wettability and their associated contact angles. Applied to the work of Bliznyuk et al. [46], they found that the effective contact angle of a glycerol droplet parallel to the stripes Θ_{\parallel} can be calculated as

$$\cos(\Theta_{\parallel}) = \frac{\alpha}{1 + \alpha} \cos(\Theta_{\text{phob}}) + \frac{1}{1 + \alpha} \cos(\Theta_{\text{phil}}) \quad (5.1)$$

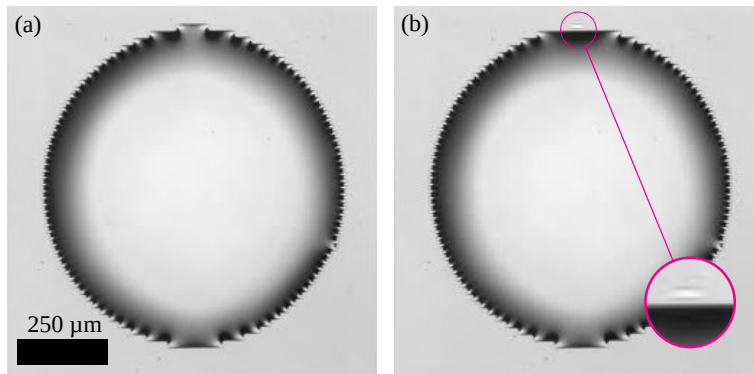


Figure 5.1: Breakup of an evaporating water droplet on a chemically patterned striped surface with a hydrophilic stripe width of $25\ \mu\text{m}$ and $\alpha = 0.5$. In (a), the droplet volume is large enough to wet N stripes. When evaporation proceeds, the droplet breaks up into a large droplet wetting $N - 2$ stripes, leaving a small droplet on the outer hydrophilic stripe, as shown in (b). Reprinted with permission from [75]. Copyright 2019 American Chemical Society.

for droplets which are 1-2 orders of magnitude larger than the stripe width. Θ_{phil} and Θ_{phob} are the contact angles on the hydrophilic and the hydrophobic material, respectively, if there was no striped pattern. Perpendicular to the stripes, the contact angle is measured to be slightly smaller than the contact angle on the hydrophobic, pristine substrate. Moreover, the shape of the droplet is elongated along the striped pattern, as it was also simulated by Jansen et al. [102] In two follow-up papers of this group, they showed that the obtained knowledge could be used to guide droplets along striped patterns on a horizontal plane when α is successively decreased [48, 49]. Jansen et al. [51] took a similar pattern and studied the evaporation behavior of sessile water droplets on it. Again the droplet size was larger than the stripe width. The researchers of [51] found that the droplet evaporates from an initially elongated shape in CCR mode (compare section 4.2.4) in the directions parallel and normal to the striped pattern. After about 33% of the evaporation time, the droplet continues to evaporate in CCR mode in the normal direction but recedes in CCA mode parallel to the stripes, leading to a sessile droplet shape that subsequently approaches a spherical cap. In the final evaporation stage, the shape of a spherical cap is maintained with subsequently smaller radii due to evaporation. According to the authors, receding in the direction normal to the stripes occurs in a stick-slip-like manner. This could also be confirmed by molecular dynamic simulations [103] and lattice Boltzmann simulations [104, 105, 106, 107]. The Surface Evolver was used to gain more insight into this topic, too [108]. However, in none of these studies droplet breakup was studied, observed, or reported.

Leopoldes et al. did some experimental and numerical research on the impact of micron-scale droplets on striped patterns. [109]. In this study, the stripe width was in the order of the droplet diameter. The authors observed that, besides that the final sessile droplet shape depends on the deposition position relative to the stripes, some detached liquid remains on a hydrophilic stripe next to the main body of the droplet. However, this finding has its origin in inertial forces that lead to the droplet's disruption during impact. The remaining of some satellite droplets could also be observed as a side observation by Jansen et al. for droplets wetting 3 to 15 stripes in a publication from 2014 [50]. Also here, inertia played a significant role, but the authors did not further investigate this observation.

When we performed similar experiments to Jansen et al. in their 2015 paper in terms of stripe width and stripe width ratio, we observed, unlike the findings in [51], that the receding perpendicular to the stripe pattern can not be simply identified as a stick-slip motion. Rather, the final movement of the three-phase

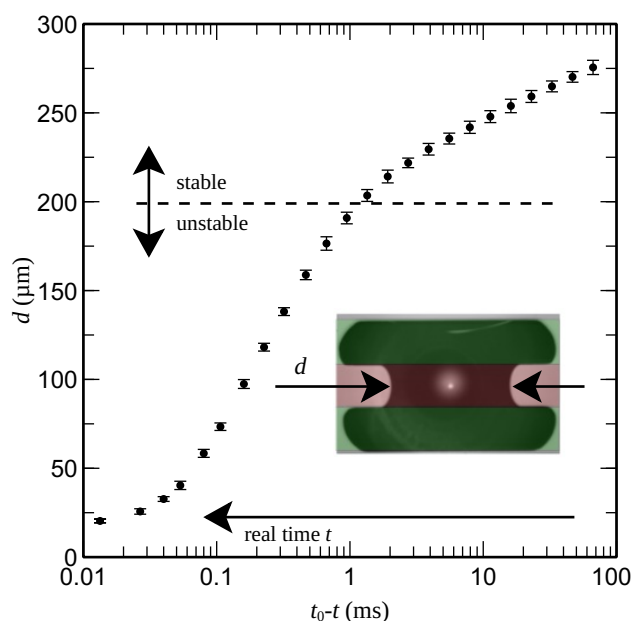


Figure 5.2: Overview of the stability problem. The inset shows a droplet in top view on a striped pattern as it may appear in the unstable regime of the wetting contrast, green areas denote to hydrophilic, red areas to hydrophobic regions. The minimum bridge width d is used throughout this and the following chapter to compare the experiments with simulations and a model. Reprinted (adapted) with permission from [75]. Copyright 2019 American Chemical Society.

contact line from a hydrophilic stripe over a hydrophobic stripe can be described as a breakup process, leaving some small amount of liquid detached from the main body of the droplet on the neighboring hydrophilic stripe. This observation is shown in figure 5.1. While in (a), the situation is shown with a droplet wetting N stripes before the receding, the droplet's main body in (b) wets $N-2$ stripes. At the same time, some liquid residue is observable on the top hydrophilic stripe.

In order to study the mechanisms that lead to breakup in more detail, the above-presented experiment must be transformed into a more generic problem. Therefore, the stripe widths are increased to be in the order of about $500\ \mu\text{m}$. This allows improved optical accessibility in terms of resolution, magnification, and light availability. Moreover, droplets with repeatable volume can be produced with a pipette to wet the same amount of stripes, i.e., three stripes in the order hydrophilic-hydrophobic-hydrophilic. However, the chosen stripe width is small enough to neglect gravitational forces or at least to minimize their influence since the Bond number is well below, or in extreme cases, around the value of 1. A sketch of the problem is shown in the inset of figure 5.2.

This transformation of the problem to a less complicated geometrical configuration allows to study under which wetting conditions, i.e., the contact angle contrast, a sessile droplet on a patterned surface can become unstable. Furthermore, the time evolution of the shape of the capillary bridge that spans over the hydrophobic stripe, as it is shown exemplarily in figure 5.2 for the bridge width d , can be evaluated in more detail. Note that in figure 5.2, as well as in similar plots in this and the following chapter, the real time t runs from right to left, since the breakup process is plotted as a function of the time before the actual pinch-off at t_0 . The less complex configuration allows us to study the instability criteria in terms of mechanics, i.e., with the Laplace-equation and energy minimization techniques, in particular, using

the Surface Evolver and compare it to the experiments. For that purpose, the minimum bridge width d is identified as a critical parameter.

5.2 Experimental Procedure and Data Evaluation

In section 3.1 and 4.2, the experimental setup, global options in data evaluation, and the substrate preparation as well as its characterization are presented. Here, the focus lies on the experimental procedure itself and the data evaluation of the taken pictures and videos.

5.2.1 Experiments

Substrates were prepared as described in section 4.2. Then experiments were performed. Depending on the type of investigation, two different setups were used. When processes on a larger length- and time scale should be investigated, i.e., the complete droplet shape is relevant, then experiments were performed inside the benchmark configuration. When the shape of the capillary bridge is of more interest, then experiments were performed on the microscopy setup. After the substrate was placed at its appropriate position, water droplets were placed on the substrate using a pipette in such a way that a droplet wets two hydrophilic stripes with one hydrophobic stripe between them. The applied droplet volume depends on the two parameters hydrophilic stripe width w_{phil} and the stripe width ratio α . As a fluid, deionized water (18.2 M Ω ·cm at 25 °C) was used, which was collected from a Milli-Q device each time right before the experiments took place. The experiments were performed at uncontrolled humidity since the focus of the present study is on the stability of such systems, not on the evaporation behavior of the droplets. An estimation on the time scale can be found in section 6.2. In both used setups, images were acquired using high-speed cameras. Triggering of the cameras took place in end-trigger mode. For each set of parameters, experiments were repeated at least seven times. In subsequent figures, mean values are shown with error bars, representing the standard deviation. In order to transform primary data to secondary data, a self written algorithm was used in the case of droplet breakup that is presented in the following section.

5.2.2 Evaluation of Primary Data

Figure 5.3 gives an overview of the high-speed image evaluation algorithm. After the program is started, the user can define parameters for the image and edge detection. This includes parameters for the edge detection algorithm itself (see subsection 3.2.3). The program then loops over all experiments in the folder where it is started. As a result of this, it first evaluates all experiments from one α -parameter study, starting from small values for α . This happens for each hydrophilic stripe width stored in the folder.

Each experiment is evaluated in the following way: First, the read in direction from the experiment is inverted. In particular, the first recorded image is the last one that is read in, the second recorded image is the one before the last one that is read in, and so on. Then the edges of each image are detected using the Canny edge detection algorithm [38]. In this step, all detected edges are saved to a three-dimensional data array called edgeDetectArray. Further information on the edge detection is described in section 3.2. Subsequently, the algorithm finds all relevant lines and columns of the image in which the capillary bridge has its maximum size. From this information, all images of the experiment are cropped to the relevant area in order to save computation time in subsequent steps. The resulting array, i.e. the new edgeDetectArray,

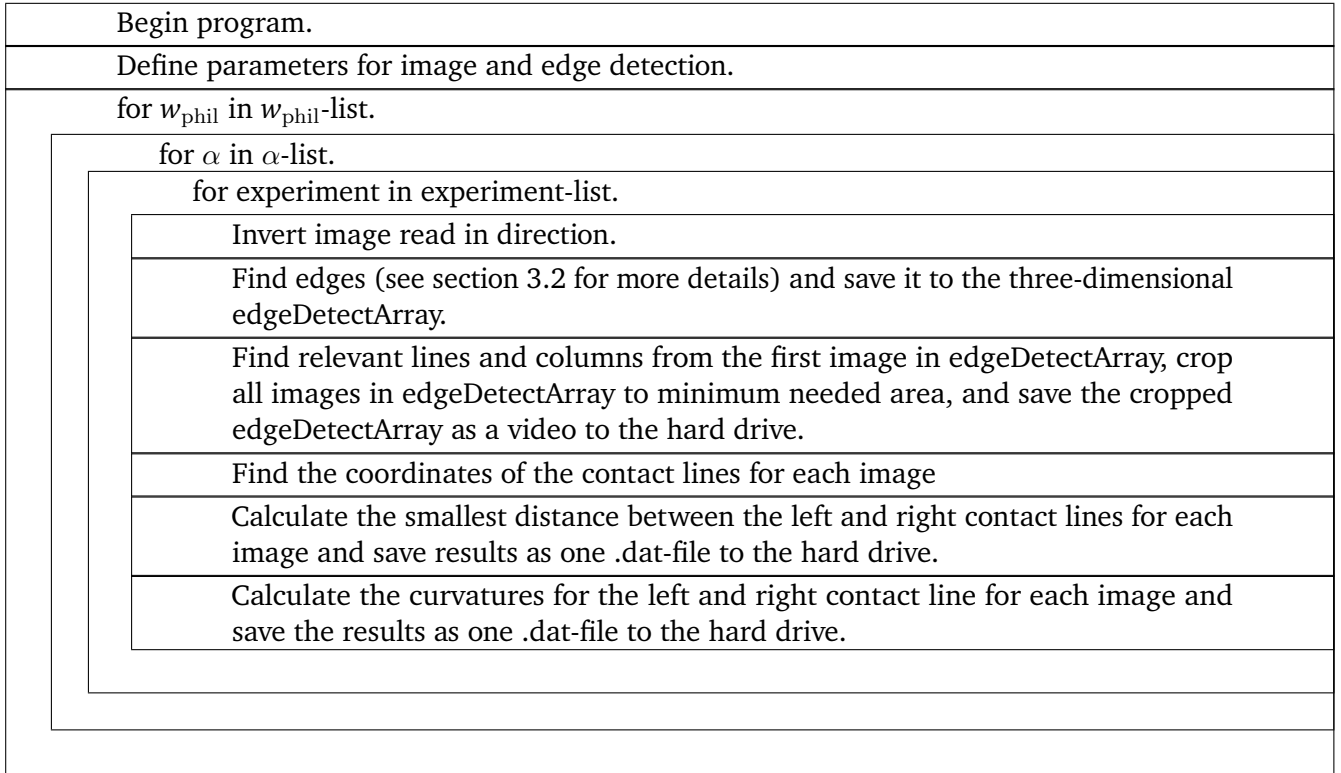


Figure 5.3: Structogram of the image evaluation algorithm.

is stored to the hard drive as a video file for verification purposes. From the edgeDetectArray, the contact line coordinates can then be evaluated for each frame and saved in the contactLineArray. Within this step, the algorithm also automatically finds the image where the capillary bridge is broken up, in particular, when the fluid detaches at t_0 . From the coordinate data from both sides of the detected edge of the contactLineArrays, the minimum width of the capillary bridge can now be calculated using the equation

$$d = \min \left(\sqrt{(x_r - x_l)^2 + (y_r - y_l)^2} \right). \quad (5.2)$$

The minimum bridge width is found by calculating the distance between each coordinate pair of the left and right contactLineArray. Only the minimum value, which equals the minimum bridge width d , is stored. This process is performed for every frame for which the capillary bridge is not broken up. The frame number and the corresponding minimal distance d are saved to the hard drive in a file, which contains two columns: the number of frames and the minimum distance in pixels.

5.2.3 Code Validation

In order to check whether the image processing algorithm works correctly, image data from a numerical simulation of the breaking up capillary bridge was evaluated by the algorithm and compared with the cell data of this simulation. The simulation was set up and performed by Mathis Fricke with the software Free Surface 3D with initial geometry data originating from the Surface Evolver, which again used boundary conditions from experiments. The reader is referred to section 6.3 for more details about this process.

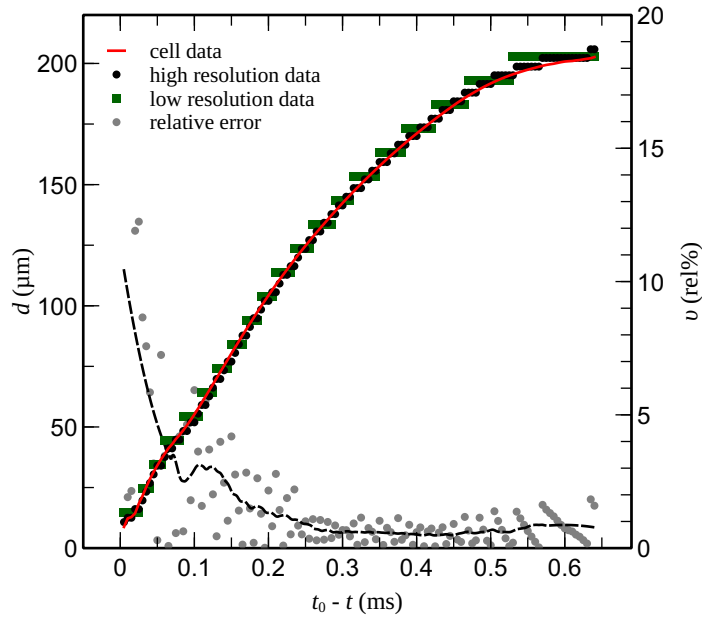


Figure 5.4: Comparison between the simulated breakup of a capillary bridge, and the evaluated images from the image data originating from simulations. The pixel resolution of the high-resolution data is $1.79 \mu\text{m}/\text{px}$ and of the low-resolution data $4.95 \mu\text{m}/\text{px}$, respectively. The relative error is plotted on the second y -axis. The black dashed line serves as a guide for the eye for the error data. Cell data originates directly from the numerical simulation and serves as the reference.

Cell data, as well as images, were written out every $1/200000$ s. Images were extracted from the visual representation of the simulation in two different resolutions, i.e. $1.79 \mu\text{m}/\text{px}$ in the case of high-resolution pictures, and $4.95 \mu\text{m}/\text{px}$ in the case of low-resolution, respectively. Figure 5.4 shows the results. The red line represents the cell data that serves as the benchmark. It originates directly from the simulations and is the minimum width obtained from the numerically calculated data within the cells representing the capillary bridge. Black and green data points represent the data originating directly from the image evaluation algorithm with the before-mentioned images as image data. From the figure, it can be seen that the breakup time t_0 is found correctly by the algorithm. This instance was also found when comparing the images with the data originating from the algorithm. Moreover, the data for the minimum bridge width calculated by the evaluation algorithm d_{pic} follows the cell data d_{cell} correctly. Deviations from the red line at different times t before breakup are due to the resolution of the images. In order to quantify the deviation from correct values, the relative error

$$v = \frac{|d_{\text{cell}} - d_{\text{pic}}|}{d_{\text{cell}}} \quad (5.3)$$

for the high-resolution data is plotted on the second ordinate as gray data points with a dashed line serving as a guide for the eye. As can be seen, v is well below 2% for larger values for d while the error increases to about 10% for small values of d . This is due to the resolution of the image. Nevertheless, with this data, the absolute error (which is $1.98 \mu\text{m}$ for the last image ($d_{\text{pic}} = 10.74 \mu\text{m}$, $d_{\text{cell}} = 8.76 \mu\text{m}$) made by the image evaluation algorithm is of the order of one image pixel size.

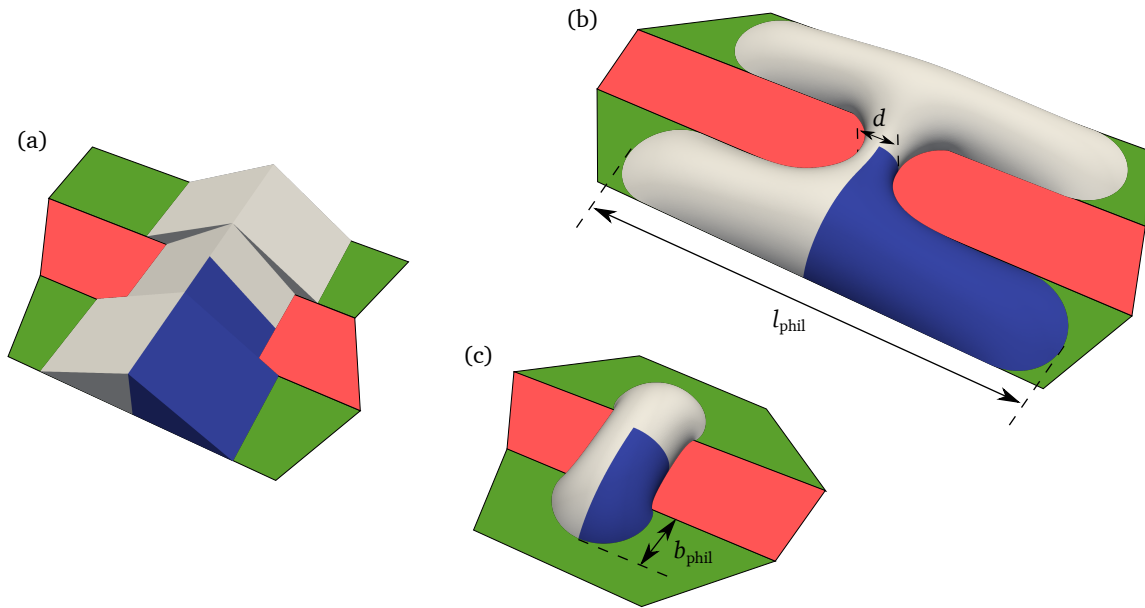


Figure 5.5: Picture of the initial geometry (a), fully converged minimal bridge width configuration (b), and fully converged critical wetting contrast configuration (c). From the experiments, it is known that the droplet has a symmetric shape. Therefore only one quarter of the droplet, colored in blue, is considered in the simulations. Hydrophilic and hydrophobic stripes are indicated in green and red, respectively. b_{phil} and d refer to the wetted width of the hydrophilic stripe and the minimum width of the capillary bridge on the hydrophobic stripe.

5.3 Numerical Procedure

For numerical calculations of the problem, Surface Evolver is used. In section 3.3, the general functionality and the idea of the numerical model is presented. Here it is shown how this is employed for droplets on chemically patterned surfaces.

5.3.1 Model and Geometry

In contrast to experimental methods, the Surface Evolver allows us to study any contact angle contrast $\Delta\Theta_{con} = \Theta_{phob} - \Theta_{phil}$, i.e., the maximum difference between the two contact angles for which no breakup is observed on the hydrophobic and the hydrophilic area of a stripe pattern surface. Therefore, it can be used to find its critical value for droplets to break up or stay intact.

Starting from the initial geometry, as shown in figure 5.5(a), both situations can be achieved within the energy minimization iterations within Surface Evolver, depending on the contact angle on the hydrophilic (green) and hydrophobic (red) stripe. Computational time can be saved by only simulating a quarter droplet with two symmetry planes, one along the center line of the hydrophobic stripe and one cutting the droplet along the capillary bridge along its axis. Symmetry planes in Surface Evolver are those with a contact angle of 90° . The resulting simulation domain is colored in blue. For a wetting contrast smaller than the critical one, it is expected that the droplet does not break up, and the liquid recedes from the hydrophilic stripe with decreasing volume. This situation is sketched in figure 5.5(c) with b_{phil} being the

wetted width of the hydrophilic stripe. On the other hand, when the contact angle contrast is large enough, a situation shown in figure 5.5(b) is expected with d , the bridge width, being the critical parameter. Both situations in principle do agree with experiments, as will be shown later on. The contact line on the hydrophilic and the hydrophobic stripe is free to move along the stripe direction.

A second version (subsequently also denoted with (v2)) of the model was implemented to calculate the critical bridge width. This was necessary because the Surface Evolver does not account for contact angle hysteresis. However, hysteresis effects may affect the wetted length on the hydrophilic stripe, and, therefore, the critical bridge width. Consequently, in version (v2), the wetted length l_{phil} is kept constant during the iterations, while all above described parameters stay untouched. This version of the model was also used for the calculations in the follow-up chapter 6 to calculate the initial configuration for the Volume-of-Fluid simulations.

In any case, no other energies except for surface energies were taken into account. In particular, gravitation was neglected, since the droplet dimensions were expected to be smaller than the capillary length.

5.3.2 Parameters and Algorithm

The required central building blocks in order to automate the calculations are described in section 3.3.2. Here, the algorithm is presented that was developed to calculate minimal energy configurations of droplets on chemically striped pattern surfaces. Besides the description, including all relevant parameters, the implemented algorithm is shown in figure 5.6.

First, the initial geometry, as sketched in figure 5.5(a), with given hydrophilic and hydrophobic stripe widths and contact angles, is loaded with a specific liquid volume. Then some pre-evolving steps are performed, including ordinary evolving and mesh refining steps to achieve a realistic surface configuration. This is followed up by an automated procedure, which, in its central piece, is recommended in the manual of the Surface Evolver: the subsequent refinement and evolving of the surface towards an energetic convergence criterion within each refinement level. Therefore, two meshing parameters and one convergence criterion are defined for each of the, in total, three refinement levels, i.e., a minimum and a maximum mesh size $e_{\text{min},i}$ and $e_{\text{max},i}$, as well as a value for the convergence of variation of the last seven iterations $c_{\text{conv},i}$, as it is needed for the described routine in section 3.3.2 that is subsequently executed. Note that the calculation of $c_{\text{conv},i}$ takes place within the surface evolving step in figure 5.6. The problem-specific routine is executed after the mesh cleanup. It consists of two queries to judge whether a droplet breaks up or evaporates as a whole:

1. Breakup: An evolved liquid surface is considered as broken up if the minimum width of the liquid bridge d in figure 5.5(b), is less than $d_{\text{thresh}} = 0.1 w_{\text{phil}}$.
2. No breakup: No breakup is expected when the wetted width of the hydrophilic stripe (b_{phil} in figure 5.5(c)) is less than $b_{\text{thresh}} = 0.25 w_{\text{phil}}$.

The breakup criterion (1.) was chosen so that the corresponding threshold is significantly smaller than the critical widths found in the experiments and the calculations with the model presented below. When this is true, then in version (v1) for the critical wetting contrast, the calculation for the pair of Θ_{phil} and Θ_{phob} is finished. On the other hand, when criterion (2.) is fulfilled, the wetting contrast is small enough that the droplet is expected to evaporate intact. The described routine is repeated for each refinement level until the calculation has reached the final convergence criterion $c_{\text{conv},3} = 10^{-7}$ for a mesh that fulfills the criteria

$e_{max} = 1/80(w_{phil} + w_{phob})$ and $e_{min} = 1/100(w_{phil} + w_{phob})$. When convergence is achieved, but none of the criteria (1.) and (2.) is fulfilled, then the droplet volume is reduced by ΔV , and the above-described routine is repeated until either the breakup or the no-breakup criterion is fulfilled. It is not necessary to further evolve a droplet that fulfills the no-breakup criterion to convergence, since preliminary studies showed that when convergence is reached, still no breakup has occurred.

In version (v2) for the critical bridge width calculation, the droplet volume is increased by ΔV after a breakup was detected, and the calculation is repeated with the higher volume. Together with the volume decrease after the droplet shape has fully converged, the volume is in- or decreased in such a way that this procedure is similar to the principle of nested intervals. The volume is changed until a pre-defined relative threshold value ΔV_{thresh} is reached which equals 0.5% of the last stable volume.

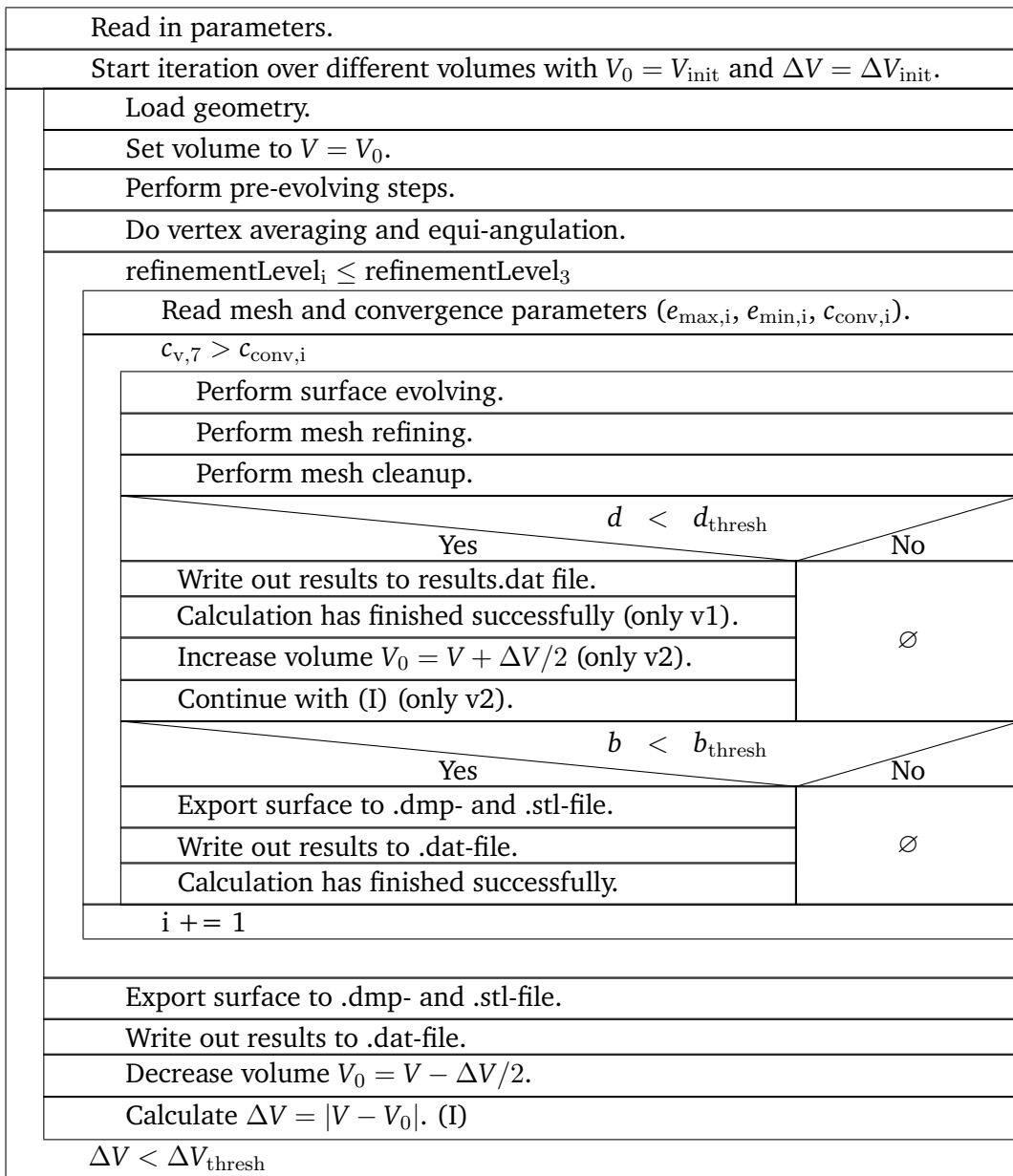


Figure 5.6: Overall Surface Evolver algorithm.

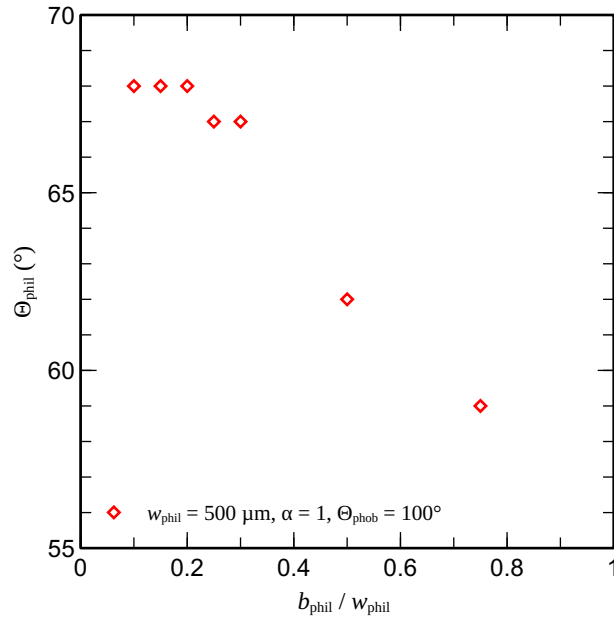


Figure 5.7: Validation of the no-breakup criterion. The dots show the calculated hydrophilic contact angle upon which no breakup is expected for a fixed hydrophobic contact angle ($\Theta_{\text{phob}}=100^{\circ}$) for different choices of the no-breakup criterion $b_{\text{phil}}/w_{\text{phil}}$.

5.3.3 On the No-Breakup Criterion

The no-breakup criterion (2.) is an empirical criterion that was developed after preliminary simulations were performed. In these simulations it is found that for a given parameter set (w_{phil} , α , Θ_{phil} and Θ_{phob}) and if the difference between the hydrophilic and the hydrophobic contact angle is small enough, b_{phil} decreases with volume. This finding is based on fully converged simulations. Consequently, in this situation it is energetically more favorable for a droplet to recede from the hydrophilic stripe than to break up and wet only the hydrophilic stripes. The value of $0.25w_{\text{phil}}$ for the no-breakup criterion results from a parameter study for $w_{\text{phil}} = 500 \mu\text{m}$ and $\alpha = 1$ that was performed prior to our final calculations. In this study the threshold value for b_{phil} was subsequently decreased, and it can be observed that the calculated hydrophilic contact angle marking the transition to no breakup changes by maximum 1° compared to the one obtained with the no-breakup criterion. This can be seen from figure 5.7. The hydrophobic contact angle was 100° in this study. Having a not too small threshold value for b_{phil} also helps to limit the CPU-time requirements of the simulations, since for a given set of parameters the number of iterations required significantly increases when the threshold value is reduced.

5.4 Results and Discussion

Figure 5.8 shows the general evaporation behavior of a water droplet at four different stages (I - IV) on a surface with a low and a high wetting contrast between the hydrophilic and the hydrophobic stripe in (a) and (b), respectively. In both cases, the hydrophobic stripe is coated with PFDTs, while in (a), the hydrophilic area is coated with TFPTS, it consists of the bare glass surface in (b). Corresponding contact angles are presented in table 4.3. The first row for each wetting contrast shows the bottom view, the second

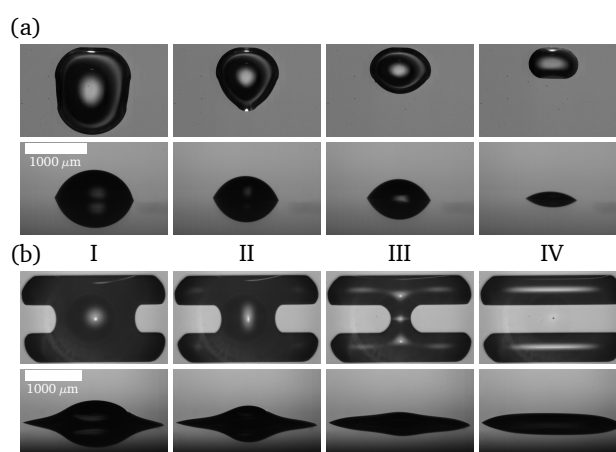


Figure 5.8: Water droplets on a striped surface at different stages of evaporation (indicated by I - IV). Hydrophilic and hydrophobic stripes are formed by TFPTS and PFDTs in (a) and glass and PFDTs in (b). While in (a) the droplet evaporates as a whole, it breaks up in (b). The width of the hydrophilic stripe is $500\ \mu\text{m}$ and $\alpha = 1$ in both cases. The first row in each case shows the top view, the second the side view. Reprinted with permission from [75]. Copyright 2019 American Chemical Society.

the side view that reflects the wetting behavior parallel to the stripe direction. In the experiment with the smaller wetting contrast, the droplet initially wets two hydrophilic stripes with a hydrophobic one between them (step I). This is followed by steps II and III in which the liquid first recedes from the bottom hydrophilic stripe and then from the hydrophobic one while the main body of the liquid phase stays intact, i.e., there is no breakup of the sessile droplet. This general behavior is similar to the one that is known from literature [102, 103, 104, 105, 106, 107, 108], and shows that it is also observable for configurations in which a droplet has similar length scales as the stripe pattern. During evaporation in stages I - III, the droplet recedes on the hydrophilic stripe with the receding contact angle of TFPTS. In stage IV, however, when the droplet finally wets only one hydrophilic stripe, the contact angle becomes smaller than the receding one on TFPTS. This behavior is known from evaporating sessile droplets on unpatterned surfaces and already discussed in section 4.2.4.

In contrast to figure 5.8(a), in (b), the difference between the contact angles on the different stripes is increased. Also here, the droplet initially wets three stripes in the order hydrophilic-hydrophobic-hydrophilic, but the wetted length on the hydrophilic stripe stays constant. At the same time, the width of the liquid on the hydrophobic region, in the following also called the bridge, decreases from stage I to III, until it finally breaks up because it is energetically more favorable to wet only the two hydrophilic stripes (stage IV) instead of these and the hydrophobic one, in addition. The contact angle on the hydrophobic stripe shows a different behavior than described before. While in stage (I) it is slightly bigger than the receding contact angle, it increases with decreasing bridge width (compare stages I to III). This is because the pressure within the liquid bridge on the hydrophobic stripe increases with ongoing evaporation due to a decreasing bridge width. Since the mean curvature must be the same at every point on the surface, the pressure within the liquid bridge can only be balanced when the curvature of the liquid above the hydrophobic stripe is increased. Therefore the contact angle increases. In stage IV, the contact angle is again larger than in stage IV. This is because the liquid located above the hydrophobic stripe in stage III has merged with the liquid above the hydrophilic stripes and, hence, the local volume is increased there.

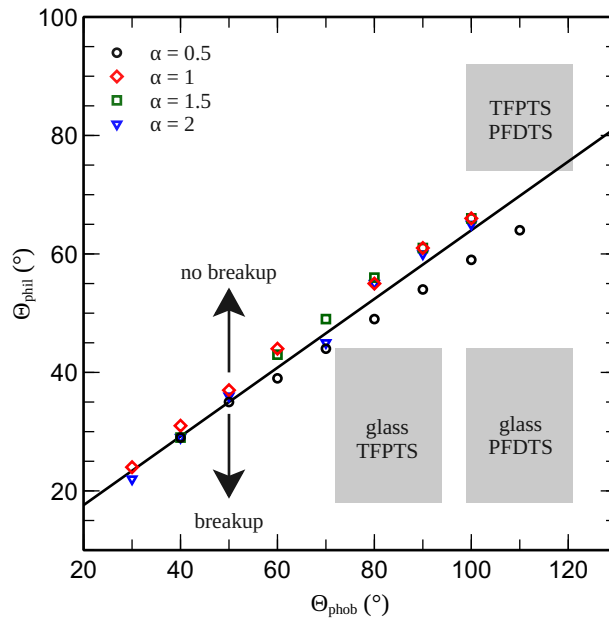


Figure 5.9: Phase diagram of the stability of droplets wetting three stripes, one hydrophobic one between two hydrophilic ones. The symbols show the boundary between the stable (no breakup) and unstable (breakup) regions as obtained with Surface Evolver. A droplet evaporates without breaking up if its contact angles are located above the line connecting the corresponding data points. Otherwise, it breaks up. The corresponding regions are marked with arrows. The rectangles denote the range of advancing and receding contact angles of water droplets on different combinations of substrates with which experiments were performed. Reprinted (adapted) with permission from [75]. Copyright 2019 American Chemical Society.

In these experiments, the wetted length on the hydrophilic stripe stays constant over the total evaporation time.

The experiments depicted in figure 5.8 show that there must be some critical wetting contrast between the hydrophilic and the hydrophobic stripe above which a droplet breaks up during evaporation instead of staying intact, as it could already be presumed from our initial experiments. Since the contact angle contrast is limited to some special cases in the experiments, its critical value is further investigated using the Surface Evolver in section 5.4.1. On the other hand, also a sessile droplet as in part (b) of figure 5.8 may be stable upon a critical pressure within the bridge. This is discussed in section 5.4.2

5.4.1 Critical Contact Angle Contrast

The results obtained for the numerical calculations with Surface Evolver are presented in figure 5.9. In these simulations, the parameters Θ_{phob} and α are kept constant. Starting from relatively high values for $\Delta\Theta_{con}$, Θ_{phil} is subsequently increased when an unstable configuration for decreasing volumes is detected until the no-breakup criterion is fulfilled. Each data point shown marks the critical contact angle contrasts $\Delta\Theta_{crit} = \Theta_{phob} - \Theta_{phil}$ where no breakup is expected for further decreased volumes. It is not necessary to further increase the contact angle range towards higher hydrophobic contact angles since, for flat surfaces, the maximum contact angle is about 120° [110, 111].

From figure 5.9 it can be seen that for $\alpha \geq 1$, $\Delta\Theta_{\text{crit}}$ is about the same, while for $\alpha = 0.5$, the critical contact angle contrast is slightly larger. However this difference between $\alpha \geq 1$ and $\alpha = 0.5$ is small and in the order of the measurable error within typical goniometric contact angle measurement errors. Therefore the influence of α on the critical contact angle contrast can be neglected for most practical purposes. Hence, the only relevant parameter to predict if an evaporating droplet breaks up is the contact angle contrast as a function of the hydrophobic contact angle. With an increasing hydrophobic contact angle, $\Delta\Theta_{\text{crit}}$ increases linearly, as it is indicated by the black line in figure 5.9 that divides the space that is spanned by Θ_{phil} and Θ_{phob} into a stable region above and an unstable one below the line. As already mentioned, no contact angle hysteresis is implemented within the Surface Evolver either on the hydrophobic or the hydrophilic stripe. It is expected that when differences in contact angles on both stripes are close to $\Delta\Theta_{\text{crit}}$, both, Θ_{phil} and Θ_{phob} are in their receding states. This observation is in accordance with the experiments performed with a TFPTS-PFDTS surface, shown in figure 5.8(a). Therefore the contact angles from Surface Evolver can be interpreted as the receding contact angles. However this is not true for large contact angle contrasts (see glass-PFDTS figure 5.8(b)).

The experiments presented in figure 5.8 can be used to validate the numerical calculations. In addition to the experiments on the materials glass-PFDTS and TFPTS-PFDTS, the material combination glass-TFPTS was tested in experiments, and breakup can be observed for all investigated α . The contact angle hysteresis for each material combination is depicted as gray rectangles in figure 5.9. I.e., the contact angle range measured with water on the given hydrophilic and hydrophobic part of the surface are shown. The performed experiments are in accordance with the results from the Surface Evolver calculations and can be understood as a validation of the numerics.

The results are shown in figure 5.9 and can be used to predict whether an evaporating water droplet on a striped surface breaks up or stays intact. In the following, the breakup regime, i.e., the region below the black line, will be further discussed based on the experimental data obtained for the combination glass-PFDTS.

5.4.2 Critical Bridge Width

When the wetting contrast is above the critical value as discussed in 5.4.1, the droplet is not a priori unstable. If there would be no evaporation, a freshly placed droplet would stay intact, provided that the contrast in contact angles is not too extreme. To quantify the stability within the unstable wetting contrast regime, it is convenient to consider the bridge width d as the critical parameter. The material combination PFDTS-glass is used as a representative in the unstable regime. In figure 5.10(a), the influence of different hydrophilic stripe widths ($w_{\text{phil}} = 250, 500$ and $750 \mu\text{m}$) and different α ($\alpha = 0.5, 1, 1.5$) on the minimal width of the bridge d are shown as a function of the time t before breakup at t_0 . The minimal width d of the capillary bridge and the time t before breakup are made dimensionless in figure 5.10b. For that purpose, w_{phil} is used as a suitable length scale for the bridge width, and the minimum width of the capillary bridge is multiplied by the inverse of w_{phil} , i.e., $D_{\text{phil}} = d \cdot w_{\text{phil}}^{-1}$, to compare the corresponding influence. In order to make the time dimensionless, the capillary time scale $\tau = (w_{\text{phob}}^3 \rho / \sigma)^{1/2}$ is chosen since the breakup process is expected to be dominated by inertia and surface tension σ . In this case, the hydrophobic stripe width w_{phob} is used as the length scale and ρ is the density of the fluid. The dimensionless time T is therefore considered as $T = t \cdot \tau^{-1}$. The characteristic behavior of the curves in figure 5.10 can be identified. For large dimensionless times $T \gg 1$, the slope of the curve is relatively small. At approximately $T \approx 1$, there appears to

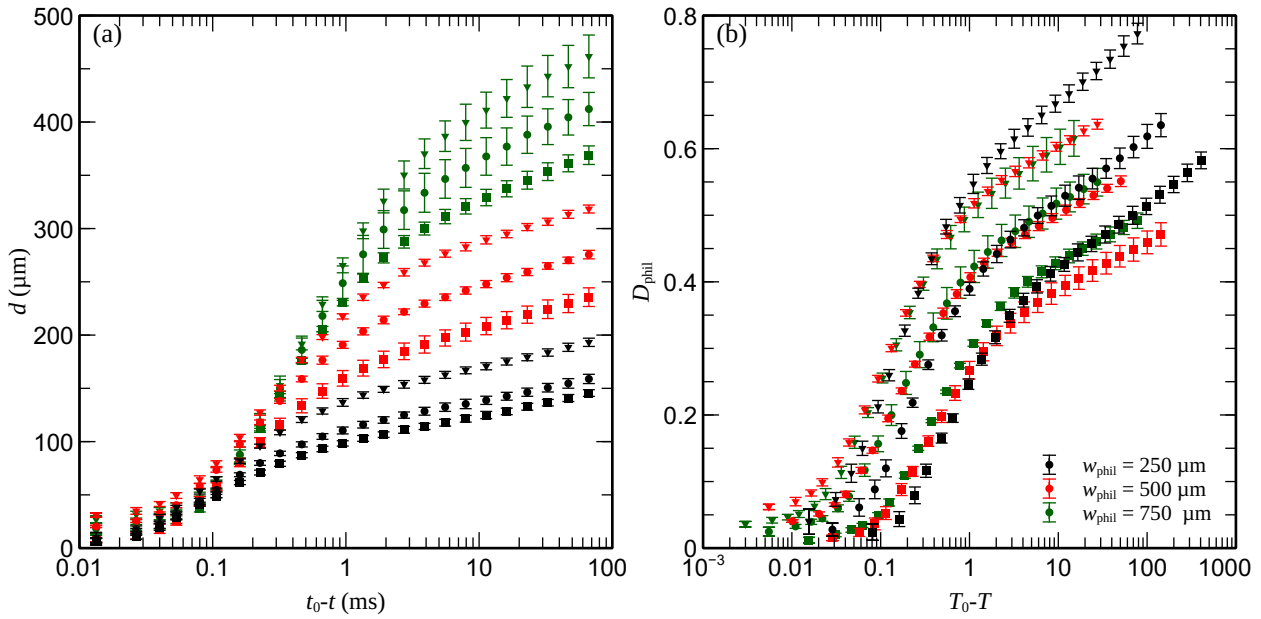


Figure 5.10: Influence of the hydrophilic stripe width on the breakup behavior for different values of α . The data are plotted in the non-dimensional (a) and dimensionless form (b). The hydrophobic stripes were obtained by functionalization with PFDTs. $t_0 - t$ and $T_0 - T$ measure the time before the breakup of the liquid bridge. t_0 and T_0 mark the points in time when the width of the liquid bridge becomes zero. In (b), the dimensionless minimal width of the liquid bridge is denoted by $D_{\text{phil}} = dw_{\text{phil}}^{-1}$. The assignment of symbols is as follows: $\alpha = 0.5$ (squares), $\alpha = 1$ (circles), $\alpha = 1.5$ (triangles). Reprinted (adapted) with permission from [75]. Copyright 2019 American Chemical Society.

be a change in the general behavior towards a steeper slope. Later on it will be shown that this is when the critical bridge width D_{crit} is reached, and the droplet becomes unstable, i.e., no configuration of the droplet surface with constant mean curvature between different points on the surface can be found for $D_{\text{phil}} < D_{\text{crit}}$.

When using the parameters described above for non-dimensionalization, it is obvious that when constant values of α but different values of w_{phil} are regarded in figure 5.10(b), the data collapses onto a single curve after the critical width is reached ($T \lesssim 1$). This indicates that the breakup process of the capillary bridge is dominated by inertial and capillary forces. In particular, it can be inferred that D_{crit} only depends on α and increases for an increased ratio of the hydrophobic and the hydrophilic stripe width. An explanation for that comes from geometric similarity considerations. For a constant hydrophilic stripe width, the evaporating droplets have different geometric shapes for different α . When α is fixed, however, and the geometric shape is rescaled, then the corresponding droplet shapes can be obtained for different values of w_{phil} . Therefore D_{phil} is independent of w_{phil} . Note that from figure 5.10, it can be inferred that for a constant hydrophobic stripe width, the critical width of the liquid bridge decreases with increased α .

When $D_{\text{phil}} > D_{\text{crit}}$, the slopes of the curves for constant α differ from each other. An extreme example can be seen for $\alpha = 1.5$. During these experiments, the atmosphere around the droplets was not controlled. Hence, this can be regarded as a result of different humidity and, therefore, different evaporation rates that lead to a decrease in the bridge width at different rates. For bridge widths below the critical

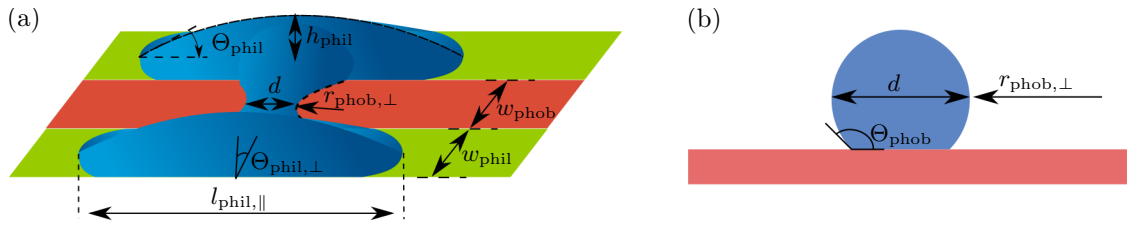


Figure 5.11: (a) Shape of a droplet as it is assumed in the model, together with relevant model parameters. Green and red areas denote hydrophilic and hydrophobic stripes, respectively. In (b) the capillary bridge is cut in the middle of the hydrophobic stripe parallel to the stripe orientation. Reprinted (adapted) with permission from [75]. Copyright 2019 American Chemical Society.

one, however, evaporation does not play any role since this breakup process happens on a small time scale. The reader is referred to chapter 6 for further information on this topic and a detailed discussion of the breakup dynamics.

Model From the experiments alone, it is not possible to extract the exact value for the critical diameter. In order to do that, it would be necessary to calculate the velocity of the capillary bridge due to the evaporation rate. Even when the humidity is controlled, only a very rough estimation of the evaporation rate is possible because of the complex droplet geometry. In order to predict the critical width of the capillary bridge, a geometrical model has been set up that compares the pressure within the bridge, p_{phob} , and within the liquid wetting the hydrophilic stripe, p_{phil} , adopting the Young-Laplace equation (2.15) for the present purpose to

$$\Delta p_i = \sigma \left(\frac{1}{r_{i,\parallel}} + \frac{1}{r_{i,\perp}} \right). \quad (5.4)$$

In equation (5.4), i refers to phob and phil. Each Δp_i can be calculated when two radii of curvature perpendicular to each other are known. For the present purpose, the directions parallel \parallel and perpendicular \perp to the stripe orientations are taken for convenience. The reader is referred to figure 5.11 for an overview of the used geometrical quantities.

For the liquid located above the hydrophilic stripe, the radii of curvature are calculated by scaling relationships using the relevant length scales w_{phil} and $l_{\text{phil},\parallel}$, the wetted length on the hydrophilic stripe. In accordance with experimental observations, this quantity is fixed. When additionally to the above quantities the contact angles of the liquid are taken into account, the radii of curvature

$$r_{\text{phil},\perp} = \frac{w_{\text{phil}}}{2 \cdot \sin(\Theta_{\text{phil},\perp})} \quad (5.5)$$

and

$$r_{\text{phil},\parallel} = \frac{l_{\text{phil},\parallel}}{2 \cdot \sin(\Theta_{\text{phil}})}. \quad (5.6)$$

can be obtained by assuming circular segments parallel and perpendicular to the hydrophilic stripe. $\Theta_{\text{phil},\perp}$ is the contact angle normal to the stripe orientation at the boundary between a hydrophilic and a hydrophobic stripe

$$\Theta_{\text{phil},\perp} = 2 \cdot \arctan \left(2 \frac{h_{\text{phil}}}{w_{\text{phil}}} \right) \quad (5.7)$$

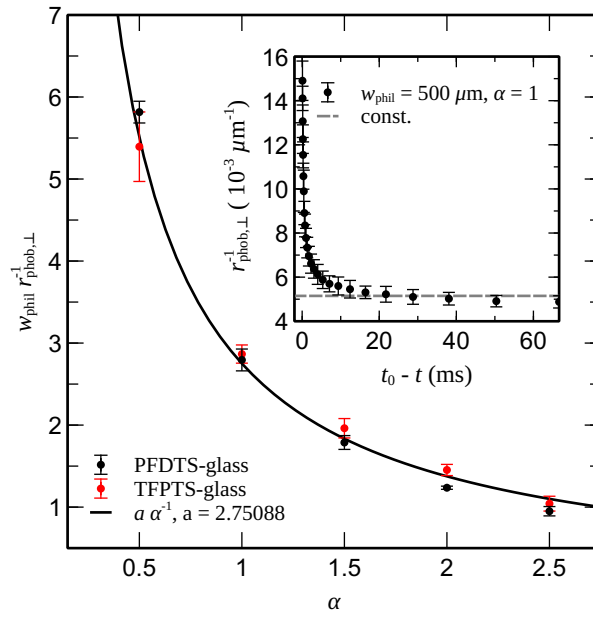


Figure 5.12: Dimensionless curvature of the capillary bridge perpendicular to the stripe orientation as a function of α for two different material combinations PFDTs-glass ($w_{\text{phil}} = 500 \mu\text{m}$) and TFPTs-glass ($w_{\text{phil}} = 250 \mu\text{m}$) as obtained from experiments. The black line shows a fit of the function $f(x) = a\alpha^{-1}$, in which a is the fitting parameter. The inset shows the typical behavior of the dynamics of $r_{\text{phob},\perp}^{-1}$. Reprinted (adapted) with permission from the supplementary material of [75]. Copyright 2019 American Chemical Society.

as sketched in figure 5.11 with

$$h_{\text{phil}} = \frac{l_{\text{phil},\parallel}}{2} \cdot \tan\left(\frac{\Theta_{\text{phil}}}{2}\right) \quad (5.8)$$

being the height of the liquid wetting the hydrophilic stripe. Thus, the pressure within the liquid above the hydrophilic stripe can be calculated when $l_{\text{phil},\parallel}$, w_{phil} , and Θ_{phil} , the contact angle on the hydrophilic stripe, are known.

The estimation of Δp_{phob} is a more difficult challenge since it is impossible to calculate this value from simple scaling relations for the curvatures of radii $r_{\text{phob},\perp}$ and $r_{\text{phob},\parallel}$. Since $r_{\text{phob},\parallel}$ is the result of the present problem, this variable does not pose a problem. $r_{\text{phob},\perp}$, however, must be determined from experiments. The results of this determination is shown in figure 5.12. There, the dimensionless curvature $K = w_{\text{phil}}/r_{\text{phob},\perp}$ at the point of minimal capillary bridge width is plotted as a function of α . The inset in figure 5.12 shows a typical dynamics of the curvature $r_{\text{phob},\perp}^{-1}$. From this, it can be deduced that $r_{\text{phob},\perp}^{-1}$ stays almost constant before the breakup. Therefore, the data points depicted in the main body of figure 5.12 show the curvature at points in time that are at least ten times the capillary time scale. It is extracted from images by fitting a parabola to the shape of the capillary bridge. The second derivative of the parabola is half of the curvature. The data points for glass-PFDTs are obtained from a substrate with $w_{\text{phil}} = 500 \mu\text{m}$ and the points for glass-TFPTs with a hydrophilic stripe width $w_{\text{phil}} = 250 \mu\text{m}$. From figure 5.12, it can be seen that for two different hydrophilic stripe widths and two different wetting contrasts, the dimensionless curvature is the same, and the data collapse onto a single curve. Therefore it can be deduced that K only depends on α . In order to have suitable input parameters for the model the data points can be fitted with

the function $K = a\alpha^{-1}$ in which a is found to be $a \approx 2.75$, and the resulting curvature is

$$\frac{1}{r_{\text{phob},\perp}} = \frac{2.75}{w_{\text{phil}}\alpha}. \quad (5.9)$$

Note that equation (5.9) is only valid for receding contact angles $\Theta_{\text{phob}} \geq 90^\circ$. From figure 5.11(b), it is clear that if the receding contact angle on the hydrophobic stripe is smaller than 90° ($\Theta_{\text{phob}} < 90^\circ$), the left-hand side of equation (5.9) must be supplemented by the factor $\sin(\Theta_{\text{phob}})$, so that the curvature is calculated normal to the plane of the liquid surface. The radius of curvature parallel to the hydrophobic stripe

$$r_{\text{phob},\parallel} = \frac{d}{2 \sin(\Theta_{\text{phob}})} \quad (5.10)$$

is modeled as a function of the minimum width of the capillary bridge d . When a droplet is in its equilibrium shape, the pressure within the droplet is uniform and, therefore, $\Delta p_{\text{phil}} = \Delta p_{\text{phob}}$, from which d can be calculated as a function of Θ_{phil} and $l_{\text{phil},\parallel}$.

In the following, a further assumption is made, which corresponds to an observation from experiments that shortly before the capillary bridge becomes unstable, almost the entire volume V of the droplet is located above the hydrophilic stripe. This can, for instance, be seen at stage III in figure 5.8(b) in which the capillary bridge covers less than 10% of the entire area wetted by the droplet. The volume of the droplet V is the sum of the liquid in the capillary bridge V_{phob} and above the hydrophobic stripes V_{phil} . With the above made assumption $V_{\text{phil}} \gg V_{\text{phob}}$, and therefore, it can be written that $V \approx V_{\text{phil}}$ and then V scales linearly with the contact angle on the hydrophilic stripe Θ_{phil} , $V \sim \Theta_{\text{phil}}$. This is correct when $l_{\text{phil},\parallel}$ is constant, which agrees with experiments. A constrained capillary surface becomes unstable if $\frac{dp}{dV}$ changes its sign from positive to negative [112, 113]. In the present problem, it can therefore be inferred that the liquid bridge becomes unstable if $\frac{dp}{d\Theta_{\text{phil}}}$ changes its sign because $\frac{dp}{d\Theta_{\text{phil}}} = \frac{dp}{dV} \frac{dV}{d\Theta_{\text{phil}}}$.

Model Results In the experiments where high-speed imaging is needed, no side view recordings were performed. To be able to see the influence of the wetted length of the hydrophilic stripe $l_{\text{phil},\parallel}$ on the critical bridge width, a sensitivity study is performed. The results are shown in figure 5.13(a). In this figure, as well as in part (b), the inverse of the width of the capillary bridge, $1/d$, is plotted as a function of Θ_{phil} . In figure 5.13(a), it can be seen that $l_{\text{phil},\parallel}$ only has a minor influence on the critical bridge d_{crit} . When only contact angles on the hydrophilic stripe within the limits of the advancing and the receding ones are regarded, the maximum error is about 5%. Therefore it is inferred that $l_{\text{phil},\parallel}$ does not have a significant influence on the breakup diameter.

From the inset of figure 5.12, it is inferred that $1/r_{\text{phob},\perp}$ stays almost constant before the bridge breaks up.

Table 5.1: Parameters used in the model. All calculations were performed for $w_{\text{phil}} = 500 \mu\text{m}$.

α	$l_{\text{phil},\parallel} (\mu\text{m})$	$1/r_{\text{phob},\perp} (1/\mu\text{m})$
0.5	2000	$11.00 \cdot 10^{-3}$
1	2300	$5.50 \cdot 10^{-3}$
1.5	2600	$3.67 \cdot 10^{-3}$
2	2900	$2.75 \cdot 10^{-3}$
2.5	3200	$2.20 \cdot 10^{-3}$

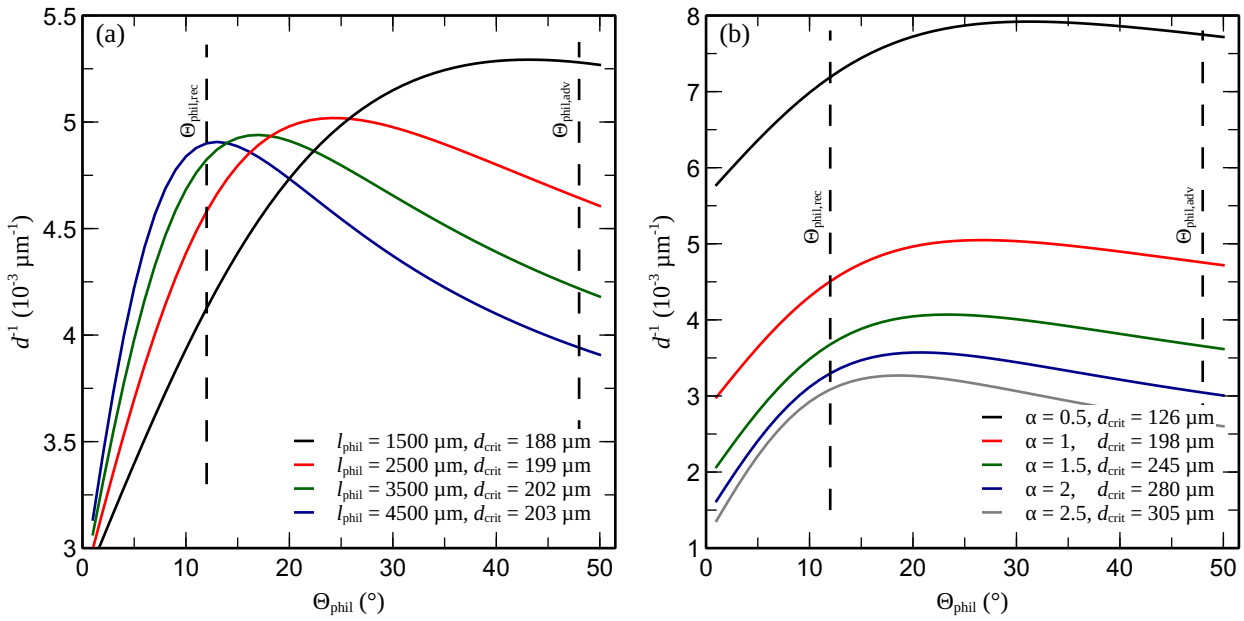


Figure 5.13: Inverse widths of the liquid bridge as a measure for the pressure obtained from the model. A change in slope from $\frac{dd^{-1}}{d\Theta_{\text{phil}}} > 0$ to $\frac{dd^{-1}}{d\Theta_{\text{phil}}} < 0$ marks the critical width d_{crit} of the bridge (see legend for corresponding values). The experimental values of the advancing and receding hydrophilic contact angles are indicated as dashed lines. (a) shows a sensitivity study for $w_{\text{phil}} = 500 \mu\text{m}$ and $\alpha = 1$. In (b), values for $w_{\text{phil}} = 500 \mu\text{m}$ and different α are shown. (b) is reprinted (adapted) with permission from [75]. Copyright 2019 American Chemical Society.

Therefore, $1/d$ can be used as a measure for the pressure inside the capillary bridge. From figure 5.8(b), it is known that Θ_{phil} increases when the width of the capillary bridge decreases in the final stage before the critical width is reached. This is because V_{phil} is increasing while V_{phob} decreases due to the adoption of the pressure in the capillary bridge and the liquid above the hydrophilic stripe. The present model also covers this effect. While the system is still in the stable region, i.e., $\frac{dp}{dV} > 0$ and, therefore, $\frac{dp}{d\Theta_{\text{phil}}} > 0$, volume is added to V_{phil} . As a result, Θ_{phil} increases. At a certain point, the slope changes from positive to negative, i.e., $\frac{dp}{d\Theta_{\text{phil}}} < 0$. At the local maximum, the bridge becomes unstable, and the critical bridge width can be read from the point where $\frac{d(\frac{1}{d})}{d\Theta_{\text{phil}}} = 0$.

Parameters used in the model calculations are summarized in table 5.1. All presented curves are calculated with a hydrophilic stripe width of $500 \mu\text{m}$.

Comparison to Simulation and Experiments The results from figure 5.13(b), i.e., d_{crit} from the points where $\frac{d(\frac{1}{d})}{d\Theta_{\text{phil}}} = 0$, are depicted in figure 5.14(a) as a function of α . The red points denote the results obtained from the Surface Evolver simulations performed with the constant length condition (v2). Within Surface Evolver, $l_{\text{phil,||}}$ is set to the values used in the model, and the contact angle on the hydrophilic stripe is considered as the contact angle where $\frac{d(\frac{1}{d})}{d\Theta_{\text{phil}}} = 0$. It can be seen that there is a generally good agreement between the model and the Surface Evolver simulations. Only the numerical value for $\alpha = 2.5$ seems to be incorrect. However, this deviation is acceptable. Multiple reasons might apply for the deviation. First of

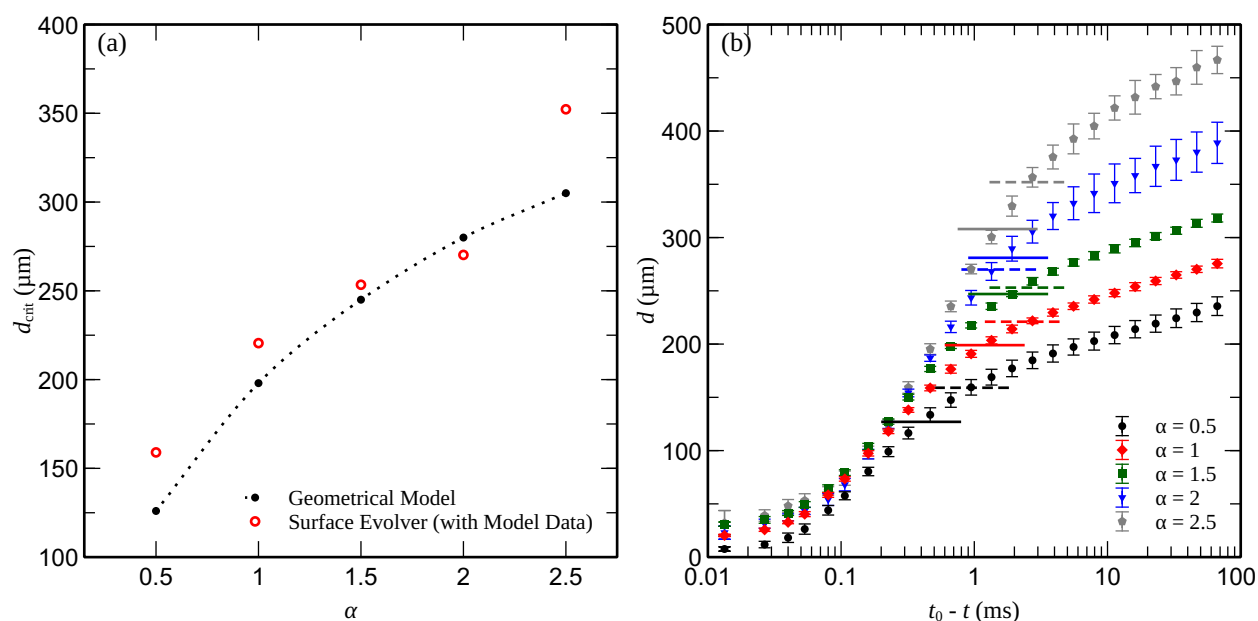


Figure 5.14: (a) Comparison between the critical bridge widths obtained from the model and the Surface Evolver simulations. In (b), the width of the capillary bridge as a function of time before breakup ($t_0 - t$) as obtained from the experiments is depicted. The lines show the corresponding results for the critical width as calculated with the model. The dashed lines represent the Surface Evolver simulations. (b) is reprinted (adapted) with permission from [75]. Copyright 2019 American Chemical Society.

all, the Surface Evolver is a tool for calculating capillary surfaces in their equilibrium shapes. However, shapes close to their point of instability are considered in the present problem. Additionally, the chosen convergence criterion has an influence on the calculated minimum bridge width. If a stricter criterion ($c_{conv,3} < 10^{-7}$) is chosen, the situation might arise that the critical volume, and therefore the critical width, is shifted towards larger values. The inverse situation appears for a less strict criterion. Moreover, due to the implemented algorithm that finds the critical width by applying the principle of nested intervals, also the chosen initial volume V_{init} , as well as the initial step ΔV_{init} at which the volume is decreased, have an influence on the final calculated critical volume. Finally, it must be considered that in the simple geometrical model presented above, the radii of curvature of the liquid above the hydrophilic stripe are modeled with simple circular segments. The shape calculated with Surface Evolver, however, is close to the one observed in experiments. Especially in the case of $\alpha = 2.5$, in which a larger deviation from the idealized picture compared to smaller values of α can be expected, the critical width found with Surface Evolver seems to better describe the experiments (see figure 5.14b).

In figure 5.14(b), the results from the model and the Surface Evolver calculations are compared to experiments. Also in these, $w_{phil} = 500 \mu\text{m}$. The results from these agree well with the experimental results indicated by the fact that the critical widths mark the points where the experimental curves change their slope. Finally, the conclusion can be made that droplets on striped patterns become unstable if the pressure within the capillary bridge cannot be balanced by the pressure that can be sustained in the liquid above the hydrophilic parts of the striped pattern.

5.5 Summary and Conclusion

Initial experiments with evaporating water droplets on chemically striped pattern surfaces with stripe widths of the order of $10\ \mu\text{m}$ were performed. These experiments showed that, unlike what is described in the literature, evaporating sessile droplets on this kind of surfaces do not necessarily recede in slip-stick motion but eventually become unstable. This observation motivated for studying the stability criteria for droplets on striped pattern surfaces in more detail. For that purpose, a key configuration is chosen, in which a water droplet initially wets three stripes in total, two hydrophilic stripes (with contact angle Θ_{phil}) separated by a hydrophobic one (with Θ_{phob}). Experiments with stripes of different wettability contrast $\Delta\Theta_{\text{con}} = \Theta_{\text{phob}} - \Theta_{\text{phil}}$ show that the stability depends on this parameter. In order to identify the critical contact angle contrast $\Delta\Theta_{\text{crit}}$, i.e., the contact angle contrast where no breakup of the droplet is expected for decreasing volume, Surface Evolver was employed. This numerical tool allows studying broad range of contact angles on both the hydrophilic and the hydrophobic stripe. It is found that the parameter space spanned by Θ_{phil} and Θ_{phob} can be divided into a stable and unstable regime for $\Delta\Theta_{\text{con}} < \Delta\Theta_{\text{crit}}$ and $\Delta\Theta_{\text{con}} > \Delta\Theta_{\text{crit}}$, respectively. The boundary between these regimes is linear and does not depend significantly on the stripe width ratio, and $\Delta\Theta_{\text{crit}}$ increases with increasing hydrophobic contact angle. Within the unstable regime, experiments were performed to explore the stability limits in terms of the minimum width of the capillary bridge that spans the hydrophobic stripe between two liquid fingers on the neighboring hydrophilic stripes. It is shown that when the minimum width of the capillary bridge d is above a critical width d_{crit} , the droplet is stable. With ongoing evaporation and, therefore, decreasing volume, the bridge width decreases until it reaches d_{crit} , and the droplet breaks up with two disjoint liquid reservoirs above the hydrophilic stripes. A dimensionless critical width $D_{\text{crit}} = d \cdot w_{\text{phil}}^{-1}$ could be identified which only depends on the hydrophobic and hydrophilic stripe width ratio. For a better understanding, a model was set up. This model balances the pressures within the liquid reservoirs above the hydrophilic stripes (the fingers) and the capillary bridge. With this simple model, it could be shown that for a decreasing capillary bridge width and therefore, an increasing pressure, a critical pressure exists that cannot be balanced by the pressure within the liquid fingers anymore. At this point, the droplet becomes unstable. The model agrees well with both the experiments and simulations with the Surface Evolver.

6 Breakup Behavior of Droplets on Chemically Patterned Surfaces

Parts of this chapter can be found in Hartmann et al. 2020 [114]. Frank Plückebaum performed some of the experiments. Lukas Weimar helped with the manual evaluation of primary data for the Rayleigh-Plateau instability. Steffen Hardt had the idea of taking the result of the Surface Evolver as the initial condition for computational fluid dynamics (CFD) simulations. The transformation of surface meshes to volume meshes was performed by Tomislav Marić and Dirk Gründing. Numerical Simulations with FS3D and the idea for the phase space is by Mathis Fricke though Li and Sprittles [115] first applied the idea of the phase space analysis without naming it explicitly. Steffen Hardt and Dieter Bothe made valuable contributions during the whole discussion process of the results together with Mathis Fricke. The presented results are, therefore, a conclusion of the discussion between Steffen Hardt, Dieter Bothe, Mathis Fricke, and the author of the present dissertation.

6.1 Introduction and Literature

In the previous chapter, the stability of droplets on chemically patterned surfaces is discussed and it is shown that the droplet is stable as long as the pressure inside the liquid forming the capillary bridge above the hydrophobic stripe can be balanced in the liquid above the two hydrophilic stripes. This is the case until a certain width of the capillary bridge is reached. When the width of the bridge decreases further due to evaporation, it breaks up. While in the previous chapter, the focus is on the statics of an evaporating droplet, the subject of the present chapter is the dynamics of the breakup process itself. In particular, the process between stages III and IV in figure 5.8(b) is examined more closely.

The breakup seems to be qualitatively similar to the collapse of a soap film between two circular rings. This was investigated by Chen and Steen [116] using numerical calculations. The authors found two breakup regimes, both dominated by the balance between inertial and capillary forces. The change in regime is due to a geometric transition during breakup. The first scaling they found is a classical result for the evolution of the minimum width d of a free liquid bridge

$$d(t_0 - t) = C \left(\frac{\sigma(t_0 - t)^2}{\rho} \right)^{1/3}, \quad (6.1)$$

where σ is the surface tension, ρ the fluid density, and $\tau = t_0 - t$ the time t before the bridge breaks up at t_0 . The authors of [116] also calculated that this scaling holds until the cylindrical like shape is formed which leads to a transition in breakup dynamics to a 2/5th-scaling that follows from the same dominating forces but is a result from the changed geometry. Note that in that context, "free" means that the bridge is entirely surrounded by some gas and not in contact with a substrate (except for the two rings, of course).

The prefactor C in equation (6.1) has been believed to be a universal constant with a value close to 1.4 for quite some time (see, e.g., Eggers and Fontelos [117]). However, more recent studies show that C is not universal. Instead, the experimentally observable value of the prefactor may depend, for example, on the initial state of the system [118].

According to Li & Sprittles[115], the appropriate dimensionless number characterizing the breakup of a free capillary bridge of a liquid is the Ohnesorge number

$$\text{Oh} = \frac{\eta}{\sqrt{\rho\sigma R}}, \quad (6.2)$$

which is the square root of the ratio of the viscous length scale $\eta^2/(\rho\sigma)$ (with η being the dynamic viscosity) and a characteristic length scale R . The width of the hydrophobic stripe in case of $\alpha = 1$, $\omega_{\text{phob}} = 500 \mu\text{m}$, is chosen as the characteristic length scale. With this definition, the Ohnesorge number for water surrounded by air can be calculated as $\text{Oh} \approx 4.70 \cdot 10^{-3}$. Clearly, the limiting cases $\text{Oh} \rightarrow 0$ and $\text{Oh} \rightarrow \infty$ characterize the inviscid and viscous breakup regime, respectively. The inviscid breakup regime is already mentioned above for the soap film. Within the viscous regime, viscous forces play the dominant role, and d scales linearly with time $t_0 - t$, i.e., $d \sim K(t_0 - t)$, with K being a constant. In the same publication of Li and Sprittles [115], a phase diagram is presented, in which, besides the two regimes mentioned above, also a third regime, the viscous inertial regime for intermediate values of Oh , can be identified in the parameter space that is spanned by d and Oh . Here, as well as in the viscous regime, $d \sim K(t_0 - t)$ is valid but with a different constant K . In [115], numerical simulations for a free capillary bridge with a similar value of Oh compared to the present case were performed. Dynamic transitions into the inviscid regime and from the inviscid into the viscous regime were observed as the minimum diameter of the bridge decreases approaching breakup.

Note that Chen and Steen [116], as well as Li and Sprittles [115] deal with a free capillary bridge without substrate contact. This is not the case in the present investigation, where the capillary bridge is in contact with the substrate. For liquids in contact with a substrate, Bostwick and Steen [113] provided a review, where the focus lies on the stability of constrained capillary surfaces in general. The same authors theoretically investigated the instability of static rivulets [119] and considered varicose (symmetric) and sinuous (anti-symmetric) modes for pinned and free contact lines. For symmetric modes, they confirmed the results by Davis [120]: For all contact angles, breakup can happen in the case of a free, i.e., unpinned, contact line, while for pinned contact lines, contact angles must be greater than 90° . Other studies exist for unpinned [121, 122] and pinned [123] contact lines, as well. In the case of anti-symmetric modes, a static rivulet is always stable in the case of a pinned contact line and unstable only for contact angles larger than 90° . These publications deal with the stability of rivulets. However, to the best knowledge of the author, no investigations on the breakup and dynamics of capillary bridges in contact with surfaces have been published so far. This chapter aims to examine the corresponding breakup dynamics and compare it to a "free" liquid bridge. For that purpose, the experiments are supplemented by numerical simulations, since only with these, it is possible to overcome some technical drawbacks origination from the experiments and to independently change fluid, and fluid-substrate properties. This is needed for detecting influencing parameters on the breakup physics. Moreover, the final breakup process is compared to the classical Rayleigh-Plateau instability, which is only possible from the experimental data due to other drawbacks, i.e. limited spatial resolution, originating from simulations.

6.2 Some Details on the Experimental Procedure and Data Evaluation

The experimental setup used to examine the bridge breakup dynamics in contact with a substrate is already presented above. Moreover, the experimental procedure itself is the same as used throughout chapter 5. Therefore the reader is referred to sections 3.1 and 5.2 for further details on the experiments. The dynamic data shown in this chapter are all recorded within the experimental setup that allows observing a droplet in top and in side view mode. No humidification of the atmosphere around the droplet was performed, and the recording frequency was set to 75,000 fps. As in the chapters before, DI-water (Milli-Q, 18.2 M Ω -cm) is used as the working fluid, and experiments are performed on PFDTs-glass patterns with different stripe width ratio $\alpha = w_{\text{phob}}/w_{\text{phil}}$. The experimental data shown in figure 6.8 results from all experiments performed within the microscopy setup since it allows a higher spatial resolution of the images taken during the breakup process. In the following, some explanations regarding the choice of this setup and the data evaluation are given.

6.2.1 Experiments

In chapter 5, it is shown that the critical diameter depends on the wetting behavior of the liquid on the hydrophilic stripe, i.e., its wetted length l_{phil} and the contact angle Θ_{phil} , while these two parameters are connected. The present chapter now deals with the breakup dynamics. Since the configuration at the onset of the instability is needed as the initial geometry for numerical simulations, it is vital to perform synchronized recordings from both the wetting behavior on the hydrophilic stripe and the breakup process of the capillary bridge. From the side view, the parameters l_{phil} and Θ_{phil} can be extracted close to the moment of the onset of breakup, while the top view gives information on the dynamics of bridge breakup, i.e., the temporal evolution of the minimum width of the bridge as a function of time $d(t)$. Only then numerical and experimental data can be compared reasonably. Therefore, the experimental setup that allows experimental observations in the top and side view mode is used for these experiments, though the resolution in top view mode is less than the one with the microscopy setup. This is taken into account by using only substrates with the parameter $w_{\text{phil}} = 500 \mu\text{m}$, which is small enough to neglect gravity but large enough to guarantee a sufficient spatial and temporal resolution. Furthermore, from chapter 5 it is already known that the only relevant geometrical parameter for a change in the dynamics is α . Therefore, it is sufficient to take into account only one hydrophilic stripe width.

Moreover, humidification of the atmosphere around the observed droplet is not needed since the breakup process occurs on the capillary time scale τ , see section 5.4.2, with $\tau = \sqrt{\frac{\rho}{\sigma} w_{\text{phob}}^3}$, with ρ being the density of the liquid, σ being the surface tension and w_{phob} being the hydrophobic stripe width. According to Li et al. [124], the evaporation time scale of a sessile droplet can be estimated as $\tau_{\text{evap}} = \frac{\rho L H}{\mathcal{D}_{\text{H}_2\text{O,air}} \Delta c_{\text{H}_2\text{O}}}$, with L and H being two different length scales, $\mathcal{D}_{\text{H}_2\text{O,air}} = 2.4 \cdot 10^{-5} \text{ m}^2/\text{s}$ being the diffusion coefficient of water vapor in air and $\Delta c_{\text{H}_2\text{O}} \approx 1 \cdot 10^{-2} \text{ kg}/\text{m}^3$ being the concentration difference of a saturated atmosphere to the surrounding air. Since typical widths of the capillary bridge are in the order of a few 100 μm , the ratio between the two time scales is $\frac{\tau_{\text{evap}}}{\tau} \approx 10^5$, and therefore, evaporation can be neglected during the breakup. The option of performing experiments within a climate chamber is therefore not needed.

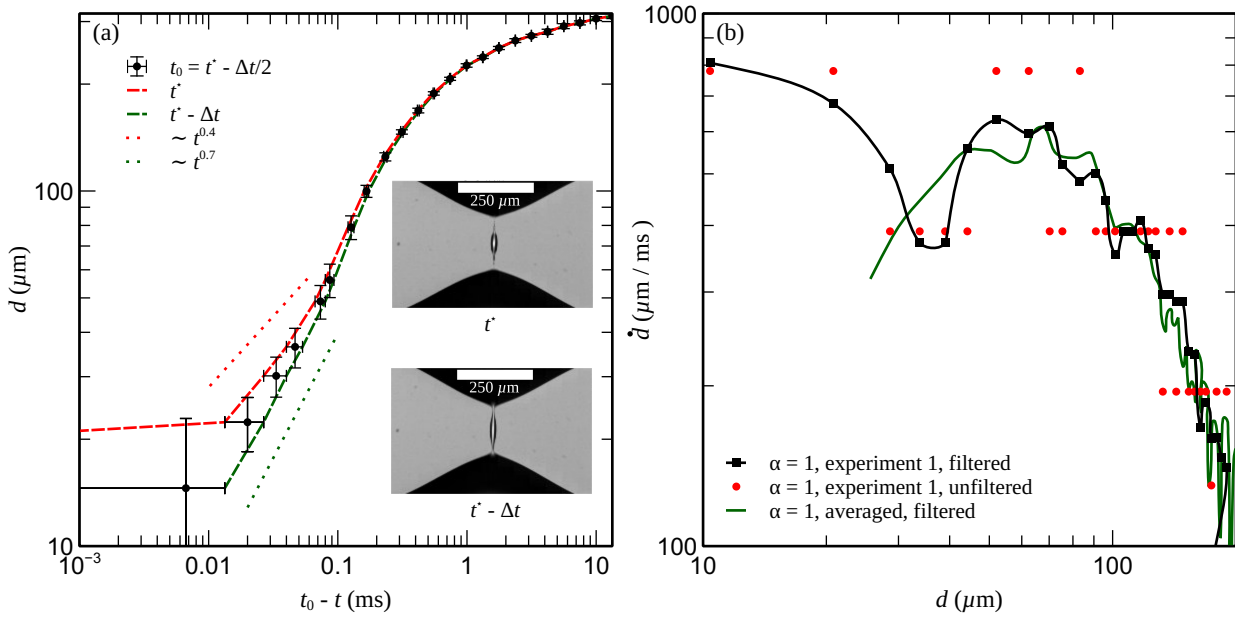


Figure 6.1: Illustration for the choice of breakup time for $w_{\text{phil}} = 500 \mu\text{m}$ and $\alpha = 1$. In (a), three curves resulting from the same set of averaged five breakup experiments are shown. The final slope of the curves (dotted lines) depends strongly on the choice of breakup time t_0 . The red curve results from choosing breakup to occur when the bridge fully detaches at t^* while the green curve represents the data with a breakup point at $t^* - \Delta t$ in which Δt is defined by the camera frame rate. The inlet pictures are taken from a different experiment from the microscopy setup. In (b), the breakup velocity is plotted versus the minimum bridge width for one experiment filtered (black) and unfiltered (red). The averaged data shown in (a) is plotted as its derivation in green color.

6.2.2 Data Evaluation - On the Choice of the Exact Breakup Time

The experimental data presented in the present chapter is evaluated with the same evaluation algorithm as presented in section 5.2.2. While in chapter 5 the exact time of breakup t_0 is of minor importance, it may have a significant influence on the interpretation of the data regarding the dynamics. This can be demonstrated with the breakup data for $w_{\text{phil}} = 500 \mu\text{m}$ and $\alpha = 1$, as it is depicted in figure 6.1(a). When images with a constant frame rate are recorded, and an event happens at a singular instance in time, this event can never be captured precisely. In the present case, this is the exact point of breakup when the fluid of the breaking up liquid bridge detaches at time t_0 . Typically, we have access to a frame in which the capillary bridge has already pinched off at t^* and a picture at $t^* - \Delta t$, in which the liquid bridge is still connected (see inlets in figure 6.1(a)). The time interval Δt is defined by the inverse of the camera frame rate, which is $\Delta t = 1/75,000 \text{ s}$. The correct pinch-off time t_0 must occur at some point in time between $t^* - \Delta t$ and t^* . From figure 6.1(a), it can be seen that the slope of the mean value of the same five experiments, depicted with logarithmic scales on both axes, changes depending on the choice of breakup. Since the slope within a log-log-plot represents the exponent of the drawn data, the choice of t_0 is of great importance for interpreting the data. Consequently, the uncertainty in breakup time is accounted for by estimating the pinch-off to happen at $t_0 = t^* - \Delta t/2$, mapping the events at $t^* - \Delta t$ to t_0 , and assuming an error in the time of $\Delta t/2$ on both sides of the mean value. The error bar in the vertical direction represents

the standard deviation of the minimum width of five measurements.

Another way to analyze the breakup process is to investigate the breakup speed as a function of the minimum width as shown in figure 6.1(b). From now on the evaluation within the space that is spanned by the minimum width and its breakup speed is called the phase space analysis. This type of analysis can be found in Li and Sprittles [115] but was independently developed by Mathis Fricke as described in [114, 125]. Since this analysis is independent from the exact point of breakup, it allows more detailed insights into the breakup processes. The key points of this analysis are presented here. However, a precise mathematical derivation of the idea can be found in the dissertation by Mathis Fricke [125]. When $d(t_0 - t)$ follows a scaling relation, as it does, e.g., in the inviscid regime (see equation (6.1)), then it can be expressed as

$$d(t_0 - t) = C(t_0 - t)^\nu, \quad (6.3)$$

with C being some constant, and ν the scaling exponent. The breakup speed can then be calculated as

$$\dot{d}(t_0 - t) = \nu C(t_0 - t)^{\nu-1}. \quad (6.4)$$

Note that the time derivation is performed with $(t_0 - t)$ as the time variable. Equation (6.3) can be converted to $t_0 - t$ and substituted into equation (6.4). After some calculus, the breakup velocity can be written as a function of the minimum width

$$\dot{d}(d) = \nu C^{\frac{1}{\nu}} d^{\frac{\nu-1}{\nu}}. \quad (6.5)$$

This means that if some scaling exists, that can be expressed with equation (6.3), then this scaling can be unambiguously identified within the phase space with equation (6.5). However, a consequent analysis of the breakup process requires the numerical differentiation of the experimental secondary data, which results from the code described in section 5.2.2. In the present case, the speed of breakup $\dot{d}(t_0 - t)$ for every data point in time for each single experiment is performed by

$$\dot{d}(d(t - (\Delta t)/2)) = \frac{d(t) - d(t - \Delta t)}{\Delta t}. \quad (6.6)$$

When this calculation is performed with experimental data, two things must be taken care of. First of all, this analysis only makes sense when single experiments are investigated. When the averaged data is taken, such as shown in figure 6.1(b), the real dynamics is averaged out, and the investigation within the phase space is less meaningful compared to the data for a single experiment, especially for the last few data points before pinch-off. Second, taking the derivative of experimental data that always is noisy requires to apply some filters to draw meaningful conclusions from it. This issue can be seen when the red and black data points are compared, resulting from one single experiment. In the present case, the Savitzky-Golay-Filter [126] is used as it is implemented within the Python package SciPy [127].

6.3 Numerical Methods

The presented data in figure 6.1 is an excellent example for the limitations of the experiments since from these data, a definitive statement concerning the governing physics of breakup is hardly possible. While in figure 6.1(a), the errors are too large, in (b), the derived data from experiments are too noisy to conclude for a definite scaling as suggested in equation (6.3). Therefore, simulations are performed to overcome the experimental limitations. However, also these suffer from some restrictions that must first be resolved for a quantitative comparison between experiments and simulation. One of the restrictions of the computational

fluid dynamics (CFD) simulation methods, as used in the present chapter, is the computation time and, hence, the duration of one simulation. The geometry of the last stable droplet configuration on a chemically patterned surface is relatively complex (see, e.g., figure 5.5(b)). If this shape must first be found from a generic geometry, such as a spherical cap, these simulations are not practicable in a reasonable amount of time without knowing the critical volume.

A practical way to overcome this issue is to use fully converged Surface Evolver calculations as the initial geometry for the CFD simulations. The parameters originating from the experiments at the moment when the bridge becomes unstable, i.e., the wetted length on the hydrophilic stripe l_{phil} , and the contact angles on the hydrophilic and hydrophobic stripes Θ_{phil} , and Θ_{phob} , must be captured precisely to calculate realistic initial conditions. These parameters are summarized in table 6.1. With this knowledge, a droplet configuration with a minimum stable volume corresponding to a minimum stable bridge width d can be calculated using the Surface Evolver model in version (v2) for the minimal bridge width configuration. Details can be found in sections 5.3 and 3.3.

The software Free Surface 3D (FS3D) used for numerical simulations is a finite volume solver, i.e., the mesh consists of many finitely small volume elements, and the free surface is modeled by exploiting the Volume-of-Fluid (VOF) method [128]. Surface Evolver, on the other hand, is a tool that accounts for a triangulated, two-dimensional mesh within a three-dimensional space. After the initial geometry for the VOF simulations, calculated with Surface Evolver, is stored as a standard triangulated language (stl) file (which is possible with a Surface Evolver internal script), this surface is transformed into a volume mesh using a tool called Surface-Cell Mesh Intersection (SMCI) algorithm. Details on this transformation can be found elsewhere [114, 129].

As mentioned above, FS3D uses the VOF-method. I.e., besides momentum, and mass, an additional variable ψ is transported in an Eulerian grid consisting of the volume elements mentioned above. ψ may have values between 0 and 1, while each phase (here it is liquid and gas) is assigned to one of these values. The phase boundary is located in those cells, where a value between 0 and 1 is calculated with a fraction of phase 1 specified by ψ . Each contact angle is kept constant during the whole simulation on each stripe, the hydrophilic, and the hydrophobic one. The Boundary Youngs interface reconstruction algorithm [130] was adapted to three dimensions, and a modification of the Navier-Slip boundary condition was introduced ("staggered slip") to dampen spurious currents. The continuum mechanical standard model (two-phase Navier-Stokes equations with Navier slip at the solid boundary, and continuum equation) was solved within the CFD calculations with transmission conditions at the phase boundary between liquid and gas. However, evaporation was neglected due to the discussion in section 6.2.1. The computational domain was the same as used within Surface Evolver calculations, i.e., a quarter droplet was calculated. Besides the Navier-Slip boundary condition, walls were assumed to be impermeable. Since the numerical simulations were not performed by the author of the present work, the reader is referred to the dissertation by Mathis Fricke [125] who performed the simulations in our joint work [114] for more detailed information.

Table 6.1: Contact angles and wetted length on the hydrophilic stripe as observed in the experiments and used in the Surface Evolver calculations.

α (—)	Θ_{phil} (°)	Θ_{phob} (°)	l_{phil} (μm)
0.5	21	102	1966
1	28	102	2638
1.5	31	102	2936

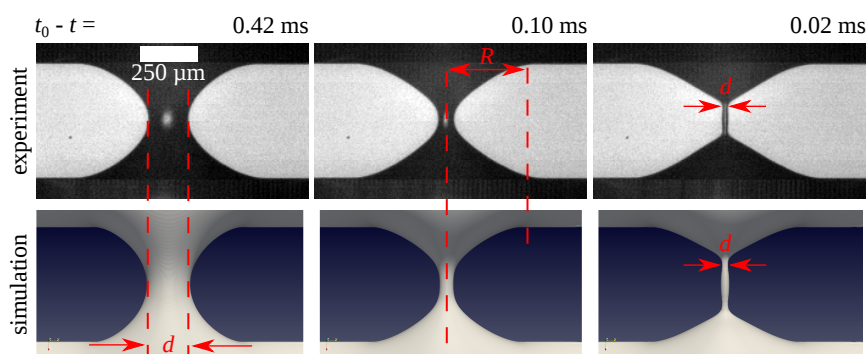


Figure 6.2: Qualitative comparison between experiment and simulation for $w_{\text{phil}} = 500 \mu\text{m}$ and $\alpha = 1$ at the same instants in time before breakup. The scale bar is valid for both experiment and simulation. Adapted from [114].

6.4 Results

The breakup of the capillary bridge is depicted in figure 6.2 at three different instants in time t before breakup at t_0 for both experiment and simulation. All images show the process in top view representation with the stripe orientation in a horizontal direction, i.e., from left to the right, and geometrical parameters $w_{\text{phil}} = 500 \mu\text{m}$ and $\alpha = 1$. In the case of experimental pictures, the black colored regions represent the liquid, while the gray ones show the substrate. Note that the contrast is increased to make the picture easier accessible for the reader. In the case of images from the simulation, the blue color represents the substrate, while the light gray color represents the liquid. Besides the hydrophobic stripe, both rows do show a small part of the liquid covering the hydrophilic stripes.

At $t_0 - t = 0.42 \text{ ms}$, the minimum width d of the catenoid-like liquid bridge lies in the middle of the hydrophobic stripe. This is also true when the bridge has evolved towards smaller d . The bridge width d agrees well between experiment and simulation (a quantitative comparison is performed in a subsequent paragraph). However, the curvature in the plane parallel to the substrate is higher in the case of experiments, which can be seen for the images at 0.10 ms before the breakup. In the final instants before pinch-off, as shown for $t_0 - t = 0.02 \text{ ms}$, the minimum of the liquid bridge moves away symmetrically from the middle of the hydrophobic stripe towards both hydrophilic stripes, right after an elongated thread (a cylindrical shape cut by the substrate at some plane along its axis) has formed between two cones which are connected to the liquid above the hydrophilic stripe. This leads to a bulge at the position where the minimum is located for larger times $t_0 - t$. In the subsequent sections, the described process is discussed in more detail. From the images at $t_0 - t = 0.02 \text{ ms}$, it can be seen that the thread length, as well as the width of the forming bulge and the minimum bridge width d , differs between the experiment and the simulation at the last instances before the detachment of the liquid bridge at the pinch-off points above and below the bulge. Different aspects emerging from the experiment and the simulation may be the reason for that. As discussed in section 4.2.4, unavoidable, surface-active contaminations may lead to significant smaller contact angles. Since the critical bridge width is about $200 \mu\text{m}$, this effect can neither be excluded from the consideration, nor captured by the Surface Evolver and the VOF-simulation. The aspects can also be a reason for the diverging curvatures in the parallel plane of the substrate, as well as the absolute value of the maximum radius of the capillary bridge, denoted with parameter R in figure 6.2 that differs slightly between the used methods, though it stays constant in both. Moreover, chemical or topological surface heterogeneities on

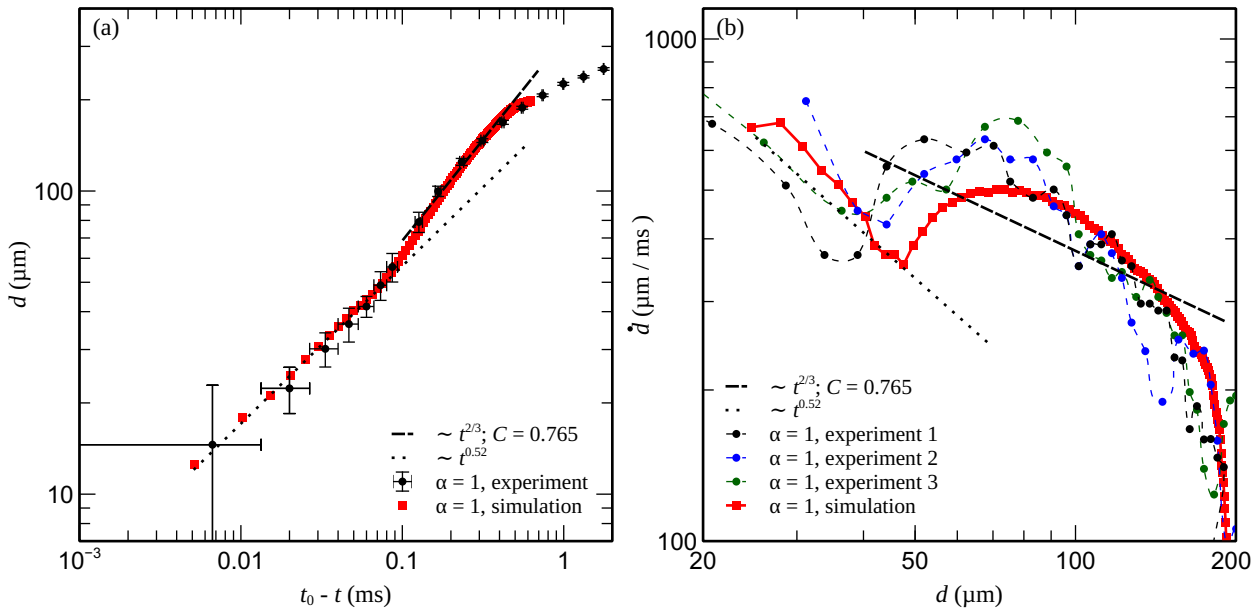


Figure 6.3: Breakup behavior of the capillary bridge for $\alpha = 1$. (a) shows the dynamics for the numerical data and the averaged experimental data. In (b), the same numerical data as in part (a) is compared to three individual experiments in the phase space that shows the speed of breakup versus the minimal bridge width. Adapted from [114].

the sub-micrometer scale can become predominant, especially in the case of the thread, leading to contact line pinning, and therefore, contact angles appear to be below the measured receding angle. On this small length scale, also numerical issues, originating from the VOF-method, are relevant. Due to mesh resolution of approximately $4 \mu\text{m}$, the bridge is under-resolved for small values of d in the order of a few μm . This is shortly before the actual pinch-off process happens, as it is shown in the inlets of figure 6.1. Though there is a good qualitative agreement between the experiment and the simulation in all relevant aspects of the bridge breakup, the actual pinch-off event can not be observed in a correct quantitative manner using the VOF-method and therefore is only investigated experimentally in section 6.4.2. However, a quantitative comparison between simulation and experiment can be made in case of the breakup dynamics before pinch-off of the capillary bridge, i.e. in the time evolution of the minimum bridge width.

6.4.1 Breakup Dynamics

$\alpha = 1$: For a quantitative analysis of the breakup dynamics, the focus is first directed to the case $\alpha = 1$. As described in section 6.2.2, besides the standard evaluation in a d - t -diagram, it also is performed within the phase space, as shown in figures 6.3(a) and 6.3(b), respectively. Since for very small bridge widths in the order of a few μm the bridge is under-resolved in the numerical simulation, the real point of the breakup cannot be extracted directly from the numerics. Instead, the data is transformed into the phase space, which gives a picture of the situation independent of the real breakup time. Then the final slope of the data is fitted with equation (6.5), as shown in figure 6.3(b). The function can be transformed back into the d - t -space, and the numerical data is adopted to this function, and it can be compared to the experimental data, see part (a) of figure 6.3.

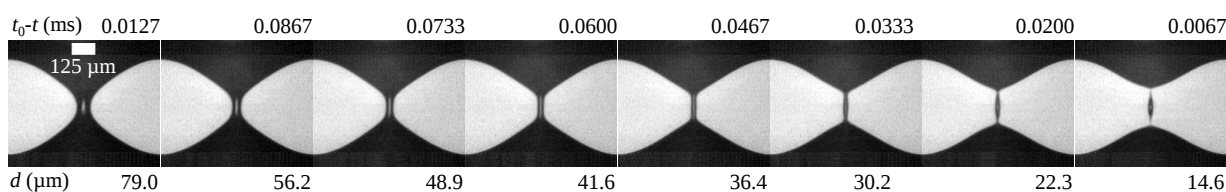


Figure 6.4: Image sequence corresponding to the last eight experimental data points in figure 6.3(a), taken from experiment 1 as shown in figure 6.3(b).

It can be seen that when the liquid bridge becomes unstable in the experiments, i.e., when the numerical data has its maximum in bridge width at about $200 \mu\text{m}$, the bridge width decreases for decreasing $t_0 - t$. During this initial phase of breakup, the bridge has a catenoid-like shape (see figure 6.2 at $t_0 - t = 0.42 \text{ ms}$). The dynamics approximately follows the relation $d \sim t^{2/3}$, indicating that initial- and capillary forces govern the breakup during this phase. The pre-factor C from equation (6.1) is found to be approximately 0.765. This general behavior is also known from a breaking up soap film spanned up between two circular rings, as investigated by Chen and Steen [116]. The authors of [116] call this phase of breakup that approximately lasts for about one decade, *role-off*, though it is stated that the $d \sim t^{2/3}$ -relation is not a real scaling, but an apparent scaling, since a real length scale is missing. This statement is supported by the data plotted in phase space in figure 6.3(b). No real scaling relation of the breakup can be found during the roll-off phase between $t_0 - t \approx 0.1 \text{ ms} - 1 \text{ ms}$. At $t_0 - t \approx 1 \text{ ms}$, the slope of the curves in figure 6.3(a) becomes more gentle, corresponding to a decreasing velocity for capillary widths between approximately $50 \mu\text{m}$ and $70 \mu\text{m}$ in figure part (b). After the velocity has reached a local minimum, at $d \approx 50 \mu\text{m}$, it increases again with a constant slope in the log-log scaled phase space. The slope corresponds to a $d \sim t^{0.52}$ -scaling, which lasts for more than one decade. This is what from now on is also called the second breakup regime.

To clarify what happens within the second breakup regime, eight images (taken from experiment 1) corresponding to the last eight data points depicted in figure 6.3 are shown in figure 6.4. Note that, except for the time between the first and the second image, Δt corresponds to the used frame rate (75,000 fps). The contrast of the images has been increased. The first image approximately reflects the capillary bridge in the state corresponding to the local maximum in breakup speed at $d \approx 79 \mu\text{m}$. The shape of the bridge is still catenoid-like, but then a thread starts to form, in the middle of the hydrophobic stripe, when the slope in figure 6.3(a) starts to change at the onset of the second breakup regime at $t_0 - t \approx 0.1 \text{ ms}$. While the width of the thread decreases, its length further increases until it simultaneously pinches-off at two constriction points. During the pinch-off process, depicted in the last four images of figure 6.4, the location of the minimum width moves from the middle of the hydrophobic stripe towards the final pinch-off points. According to the made observations, the second breakup regime, therefore, is set in motion with a shape change towards a liquid thread, and the pinch-off process follows $d \sim t^{0.52}$ -scaling. However, note that this scaling does not agree with the $d \sim t^{2/5}$ -scaling for a free soap film bridge found in [116]. On the other hand, numerical simulations with different viscosity, surface tension, and contact angles were performed. All of these do not influence the general breakup behavior, i.e., the scaling exponent, but only the constant C of the inviscid scaling in the case of varying the surface tension. The pinch-off process itself is discussed in more detail in section 6.4.2.

$\alpha = 0.5$: When the stripe width of the hydrophobic area w_{phob} is decreased by a factor 2, i.e., $\alpha = 0.5$, the critical width decreases, as discussed in chapter 5. Therefore, the maximum width in the simulation is smaller than for the case $\alpha = 1$. After a short initial phase, in which the capillary bridge in numerics stays almost constant before it becomes unstable, the agreement between this data and the experiments is

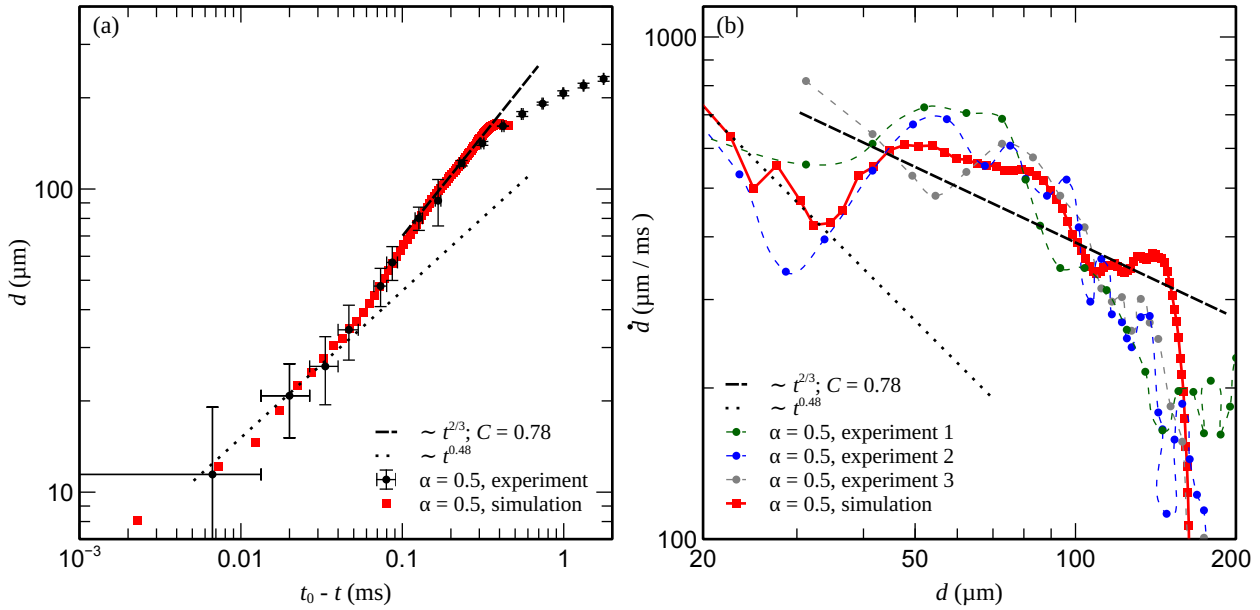


Figure 6.5: Breakup behavior of the capillary bridge for $\alpha = 0.5$. (a) shows the dynamics and (b) the phase space. Adapted from [114].

quantitatively good. The apparent $d \sim t^{2/3}$ -scaling is also investigated for the present case with the constant $C = 0.78$. Also, the second breakup regime can be found for $\alpha = 0.5$. However, the scaling exponent within this regime is determined to be ≈ 0.48 , which is slightly lower than in the previous case.

$\alpha = 1.5$: For $\alpha = 1.5$, the data points of the simulation and the experiments in the initial phase differ significantly from each other. As described in section 6.3, Surface Evolver is used to calculate the initial condition for the CFD-simulations. Surface Evolver usually is employed to calculate static capillary shapes. Since the initial condition of the simulation is very close to the point of instability, it is not calculated consistently with the experiments. However, after the initial phase, the experiments and the numerics agree well, and the data can be compared. As for $\alpha = 0.5$ and 1, the roll-off phase is governed by capillary and inertia forces with $C = 0.75$. The exponent of the second dynamic regime is determined to be slightly smaller than for the other cases. The scaling is found to be $d \sim t^{0.54}$.

6.4.2 Rayleigh-Plateau Instability

Four pictures of the unstable capillary bridge at four different instances in time are shown in figure 6.7. From a catenoid-type structure, as depicted in part (a), a liquid thread forms with a thread width of d_{thread} , which more precisely, is a liquid cylinder cut by the substrate in a plane along its axis, as shown in figure 6.7(b). This thread forms between two cones that look like triangles with unique opening angles β in the images from the top perspective. The distance between the two cone tips is denoted as λ . At these tips, this thread first gets pinched (figure 6.7(c)), before the capillary bridge finally breaks up right there, as can be seen in figure 6.7(d), leaving a larger primary satellite droplet in the middle of the hydrophobic stripe. Some smaller secondary satellite droplets can be seen between the receding liquid of the two former cones and the large droplet, which have their origin in a self-similar breakup process. This behavior can

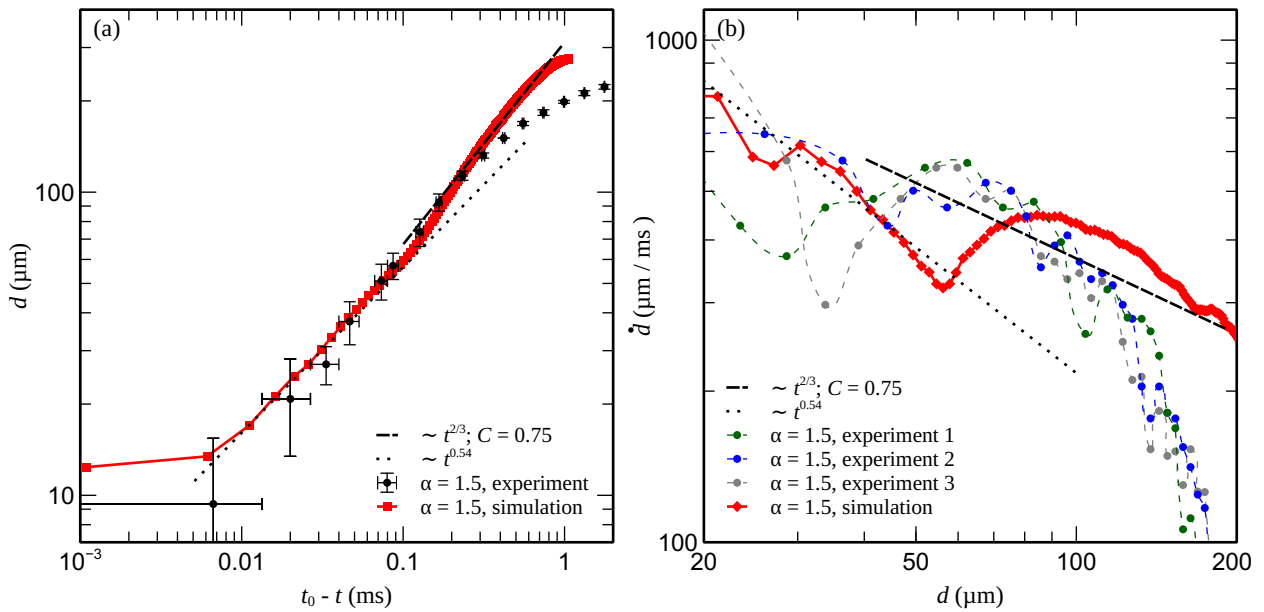


Figure 6.6: Breakup behavior of the capillary bridge for $\alpha = 1.5$. (a) shows the dynamics and (b) the phase space. Adapted from [114].

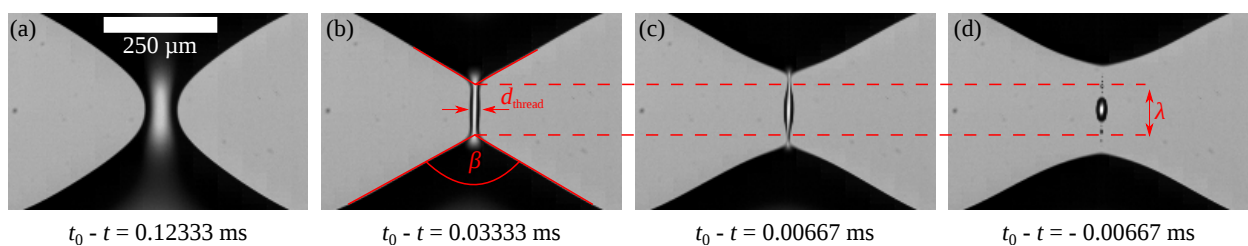


Figure 6.7: Qualitative analysis of the final breakup behavior of the capillary bridge. From a catenoid type structure in (a), the bridge has evolved to a liquid thread between two cones in (b). The final breakup happens at two pinch-off points (c), leaving behind a primary droplet with smaller secondary droplets in the middle of the hydrophobic stripe (d). The scale bar in (a) is valid for all images. Adapted from [114].

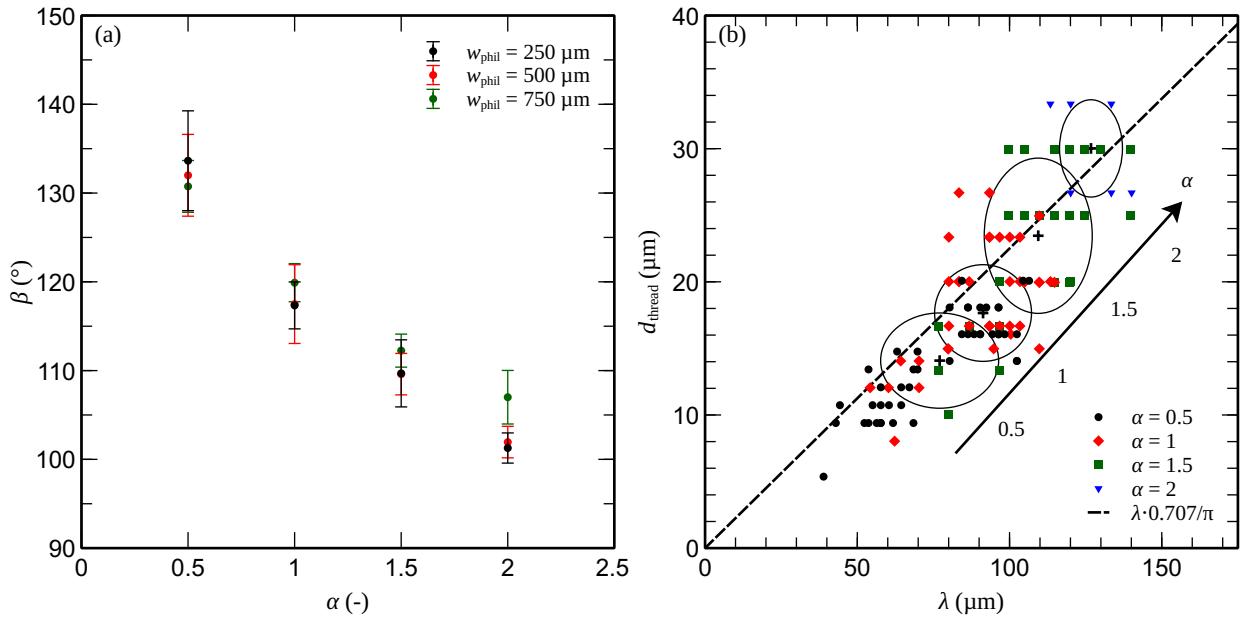


Figure 6.8: Quantitative analysis of the final breakup behavior. For a definition of the parameters see figure 6.7. In (a), the opening angles β of the cones are evaluated for different α 's and hydrophilic stripe widths. In (b), the diameter d_{thread} of the cylindrical segment is plotted versus the measured wavelength λ for $w_{\text{phil}} = 500 \mu\text{m}$ and different α . Each point represents one experiment. These are condensed in the ellipses, representing the standard deviation around the mean value for each α . The dashed line corresponds to equation (6.7). Adapted from [114].

also be observed when a soap film between two circular rings breaks up, as investigated by Chen and Steen [116]. In the following part, this process is analyzed more quantitatively.

As can be seen from figure 6.7(b), two events happen almost simultaneously and can be observed for all values of α . I.e., two cones and a liquid thread between the tips of the cones are formed in each experiment. In the case of the cones, it can be observed that for each value of α these have unique opening angles β , as plotted in figure 6.8(a). The angles are highly reproducible for different experiments and independent of the hydrophilic stripe width w_{phil} , which can be explained by geometrical symmetry considerations (discussed in chapter 5). The second feature, the liquid thread, breaks up in a self-similar process. In figure 6.8b, the width of the thread d_{thread} is plotted versus the distance λ between the two tips of the cones for all experiments performed with $w_{\text{phil}} = 500 \mu\text{m}$ and $\alpha = 0.5 - 2$. Each point represents one experiment, and different values for α are plotted in different colors. In order to compare the trend for different α 's, data points are condensed to black crosses with ellipses around them, representing the mean value and the standard deviations for λ and d_{thread} for each ratio of the hydrophobic and the hydrophilic stripe width, respectively. The experimental data are compared with the classical Rayleigh-Plateau instability, according to which a cylindrical liquid jet disintegrates into droplets due to the tendency of a system to minimize its energy. Following this classical theory, d_{thread} is connected to λ , which is the critical wavelength that belongs to the most unstable mode, by

$$d_{\text{thread}} = \frac{\lambda}{\pi\sqrt{2}}. \quad (6.7)$$

The reader is referred to section 2.1.2 for more information.

According to figure 6.8(b), the final breakup process follows the classical Rayleigh-Plateau instability within the experimental error. This can be explained by the receding contact angle to be $\Theta_{\text{rec}} = 102^\circ$, which is slightly higher than 90° . In case of a contact angle of 90° and an unpinned contact line, a cylindrical liquid jet in contact with a substrate breaks up following the classical Rayleigh-Plateau result, which is formally calculated in, e.g., [113], but can be also be deduced from symmetry consideration. A remarkable finding is that the distance between the tips of the cones corresponds to the critical wavelength of the classical Rayleigh-Plateau instability, which is also indicated by the distance of the secondary satellite droplets. The reasonable agreement with the classical Rayleigh-Plateau theory, which is based on an inviscid fluid, also indicates that the influence of viscous stresses that may show up in the final stages of the breakup process, is not significant for the decay of the thread. The scattering of the data points within each group of experiments might be a result of the uncertainty in contact angles but also to roughness effects. The roughness, as well as chemical defects do become important on the order of a few μm . This is already discussed in section 4.2.4. Moreover, the equally distanced data points in the direction of d_{thread} directly result from the spatial resolution of the optical setup and increase with increasing α since the used magnification decreases with increasing α to capture most of the liquid bridge. Due to the small time scale of the breakup process and the limited amount of light delivered by the used light source, image acquisition is limited to the given pixel resolution. However, d_{thread} and λ increase with increasing α . This again is consistent with decreasing β for increasing α (see figure 6.7).

6.5 Summary and Conclusion

In the present chapter, the breakup dynamics of a capillary bridge that forms on a hydrophobic stripe during evaporation of a water droplet wetting a chemically striped pattern surface in the order hydrophilic-hydrophobic-hydrophilic, is studied numerically and experimentally. Different stripe width ratios α between the hydrophobic and the hydrophilic stripe are considered, i.e., $\alpha = 0.5, 1, \text{ and } 1.5$. Experiments were performed with two synchronized high-speed cameras. One camera was used to record the breakup dynamics. The other one was employed to record the wetting behavior on the hydrophilic stripe by means of the wetted length and the contact angle at the moment when the bridge becomes unstable. These latter two parameters were used to calculate physically realistic initial conditions with the Surface Evolver for the employed simulation tool Free Surface 3D (FS3D). The data transfer from the surface mesh emerging from Surface Evolver into the volume fraction field needed for solving the three-dimensional two-phase Navier Stokes equations employing the Volume-of-Fluid method was achieved using the Surface-Cell Mesh Intersection algorithm [129].

A detailed picture of the breakup dynamics could be attained by transforming the breakup data into the phase space, which, in particular, allows to remove the choice of breakup time t_0 that may have a significant influence on the evaluation of the breakup process. I.e., the phase space allows us to obtain the scaling exponents systematically. After the bridge becomes unstable, an initial regime, the roll-off regime, can be observed lasting for about one decade. This initial regime follows approximately the inviscid theory $d(t_0 - t) \sim C(\sigma(t_0 - t)^2/\rho)^{1/3}$, which is also known from the breakup of a free capillary bridge. In the present case, C is found to be $0.75 - 0.78$ in both experiments and simulations. Approximately one decade after the bridge has become unstable, a transition towards the second breakup regime can be observed. In experiments, this transition is manifested by a shape conversion from a catenoid-like liquid bridge towards an elongated thread. Within the phase space picture, it can be seen for both the experiments and the simulations that during this shape adjustment, the velocity of breakup significantly decreases until a local minimum in the breakup speed is reached, marking the start of the second regime. For approximately

one decade, the second breakup regime follows a different scaling with an exponent found by fitting the numerical data. I.e., the scaling relation that is extracted is $d(t_0 - t) \sim (t_0 - t)^\nu$ with ν ranging between 0.48 and 0.54. A good quantitative agreement between simulations and experiments down to a bridge width of approximately $10 - 20 \mu\text{m}$ is established.

In experiments as well as in the numerics, a pinch-off process can be observed during the second dynamic regime. In particular, this is when a liquid thread (a cylinder cut by a plane) has formed between two cones. This process was studied in more detail using the data obtained from experiments. It is found that the cones have well-defined opening angles that decrease with an increasing α . The final liquid thread breaks up in a Rayleigh-Plateau type instability. Remarkably, the critical wavelength of the breakup corresponds to the distance between the tips of the cones.

7 Surface Taylor-Cones

The content of this chapter represents work in progress and is not published elsewhere at the submission date of the present dissertation. It can be understood as a preliminary study. Frank Plückebaum performed most of the experiments presented below, and Lukas Weimar helped to evaluate the primary data. Michael Heinz programmed DENIISE [30], with which the contact line and contact angle dynamics could be evaluated with some minor modifications. Steffen Hardt gave valuable input during the discussion of the results.

7.1 Introduction

In chapters 5 and 6, some effects that can happen after droplets have been jetted onto structured substrates are investigated. Besides inkjet printing, another way to apply some material onto a substrate is electrospinning. This technique can be used to produce fiber mats [131], tissue implantats [132], or scaffolds [133], among others. Xue et al. [134] wrote an extensive review about electrospinning. Between a needle and a substrate, an electric potential U is applied (in the order of about $U = 10$ kV). When some liquid is transported through the needle with a constant volume flow, a thin thread is generated that is jetted onto the substrate. When the focus is directed onto the needle tip, a liquid cone can be observed [135] that is consequently called Taylor-Cone, named after G. I. Taylor, who was the first person to analytically describe this shape [28]. It results from the balance of Maxwell stresses and surface tension and is stable at a critical potential U_{crit} , i.e. no liquid jet does emerge from the tip of the cone. Taylor found that the cone's opening angle β has a unique value of 98.6° .

The same governing forces, as in electro-spinning, do act between two oppositely charged droplets attached to two needles that are positioned opposite each other. Bird et al. [27] observed that the water droplets attract each other and two cones form at each droplet. The authors could show that these two droplets do merge or recoil depending on the critical opening angle of the cones (note that Bird et al. denoted their critical angle as $\pi/2 - \beta$). Liu et al. [136] used the same setup but with oil between two water droplets and ramped up the DC field. The authors showed that the droplets do merge upon a critical voltage depending on surfactant concentration within the water, among others. With this knowledge, they can measure a threshold in the disjoining pressure and make conclusions on emulsion stability. Parameters that lead to non-coalescence were also investigated for free suspended droplets within a homogeneous electric field between two plates of a capacitor [137], or a sessile droplet and a pendant droplet [138].

When it comes to electrically driven coalescence between two oppositely charged sessile droplets with the electric field being directed parallel with the surface, the literature is sparse. To the best knowledge of the author, only two publications do exist that deal with this topic. In [139], Xie et al. observed the merging of two droplets with a subsequent flashover, on which the focus is directed in that publication. Ndoumbe et

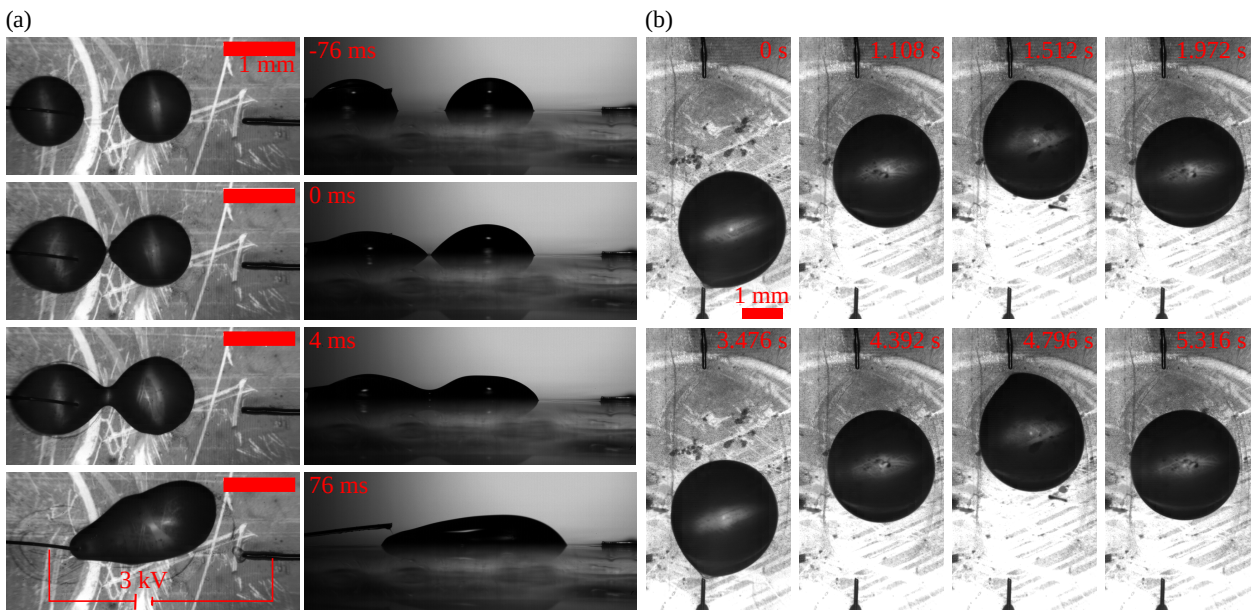


Figure 7.1: Droplets merging at the three-phase contact line and droplet "Ping-Pong". In (a), an uncharged $2.5 \mu\text{l}$ DI water sessile droplet merges with a charged one at 0 ms. A conical shape can be observed. The left hand-side shows top, and the right hand side of (a) side view images. A cone-like deformation of the droplet is also seen in (b) where a $5 \mu\text{l}$ droplet of 1 mol/l NaCl in DI water gets repelled from the bottom electrode, and then is pulled by the top electrode. After a charge transfer has happened, the movement is directed in the opposite direction. Note that the droplet does not touch the electrode. In both experiments, substrates with a hydrolyzed silicon oil layer were used. The potential difference was 3 kV.

al. [140] performed a joined numerical and experimental study on the parameters leading to the merging of two sessile droplets. However, the authors used hydrophobic surfaces.

In the ongoing work presented in the present chapter, initially, an attempt was made to study the influence of the contact line on the merging behavior of sessile droplets. Therefore, initial, provisionally experiments were performed with two electric copper wires. The ends of the wires were located close to the surface. As a substrate, the hydroxy-terminated PDMS surface [88] was used, as already mentioned in section 4.3. The result can be seen in figure 7.1(a) in the top (left) and side view (right). It can be observed that after an electric potential has been applied, the droplets are attracted to each other and do initially touch each other at the three-phase contact line after a cone shape has developed at $t = 0$ ms. Then the droplets merge. Note that the droplet between the electrodes is initially uncharged, but di-electrophoretic effects lead to a local accumulation of charge on the left and right side of the droplet. However, before proceeding with the droplet merging, we wanted to characterize the structure of the liquid, i.e., the cone structure, between one charged droplet and an electrode. Therefore, the same setup was used, but only one droplet was placed so that it was in contact with one electrode. When the voltage was switched on, the droplet was pulled towards the electrode on the opposite side. Then the liquid came close to the electrode but did not touch it and was repelled to take the inverse direction. This indicates that there is some charge transfer through the hydrolyzed silicon oil. Then the process was repeated several times until the droplet came to rest. The droplet ping-pong is, for sure, a process that is worth being investigated separately. However, this chapter is about an improved setup to study the cone formation, and the cone characterization itself. For that purpose, the cone is compared to the original Taylor-Cone. Since at the rear part of a sessile droplet

sliding down an inclined surface, a similar structure can be observed (see, e.g., [141, 142, 143]), this example is taken for comparison, as well.

7.2 Methods

In contrast to the chapters that deal with the wetting states of water droplets on micro-patterned surfaces, the Surface Taylor-Cones were studied in experiments only.

7.2.1 Samples and Setup

In order to study the electrostatically triggered formation of a liquid bridge between a droplet and an electrode on a substrate, samples need to be produced, which must fulfill specific requirements. Note that in all considerations, it must be ensured that the substrate has a defined wettability. The requirements that must be fulfilled are:

1. Hydrophilic surface with small contact angle hysteresis, ideally transparent and non-conductive.
2. Defined shape of the electrode for comparable electric fields.
3. Defined length scale between the initial distance of the sessile droplet and the electrode.
4. Defined fluid supply in terms of electric charge and flow rate.
5. Optical access from two sides, to allow simultaneous observations in side view and top or bottom view.

As a carrier substrate, a microscopy glass slide (Carl Roth, 76 x 26 mm) is used on which the sol-gel layer (main components PEG-M (Evonik, Germany, Dynasylan 4148) and TEOS (abcr, Germany, CAS:48-10-4)) is applied via spin coating, based on the idea of Kaneko et al. [90]. Silicon substrates cannot be used due to their small but present conductivity leading to observable electrolysis. A detailed description of the substrate preparation, as well as its characterization, can be found in section 4.3. The surface-modified substrate serves as the basis for all other fluid and electrical connections, as it is sketched in figure 7.2.

To have a comparable electric field while simultaneously using the lowest possible electric voltage, the shape and type of the electrode are also of importance. First experiments with a flat electrode, i.e., a vertical stripe of copper tape spanning over the total width of the substrate, were performed. The electric fields were too small so that the bridge forms at a small distance before the electrode, and therefore, its dimensions were too small to have a sufficient spatial resolution at higher frame rates. Instead of a straight electrode, a triangular electrode shape is preferred with one tip pointing towards the fluid outlet of a piece of Polydimethylsiloxane (PDMS). The opening angle of the electrode is approximately 15° . Tests with sputtered electrodes prior to the coating of the sol-gel layer and electrodes made out of copper tape applied onto the substrate after the coating process was performed. Both setups can be used to investigate the forming of capillary bridges. However, for every single experiment, a new substrate must be fabricated since after the contact of the liquid with the electrode (a), the wetting behavior close to the electrode has changed to an almost entirely wetting substrate, and (b), the sputtered material is removed by an electric discharge. Since sputtering is performed externally, it was decided to choose the electrode setup with the triangular copper tape on top of the coating, though the repeatability of the shape is not as good as when the electrode is sputtered.

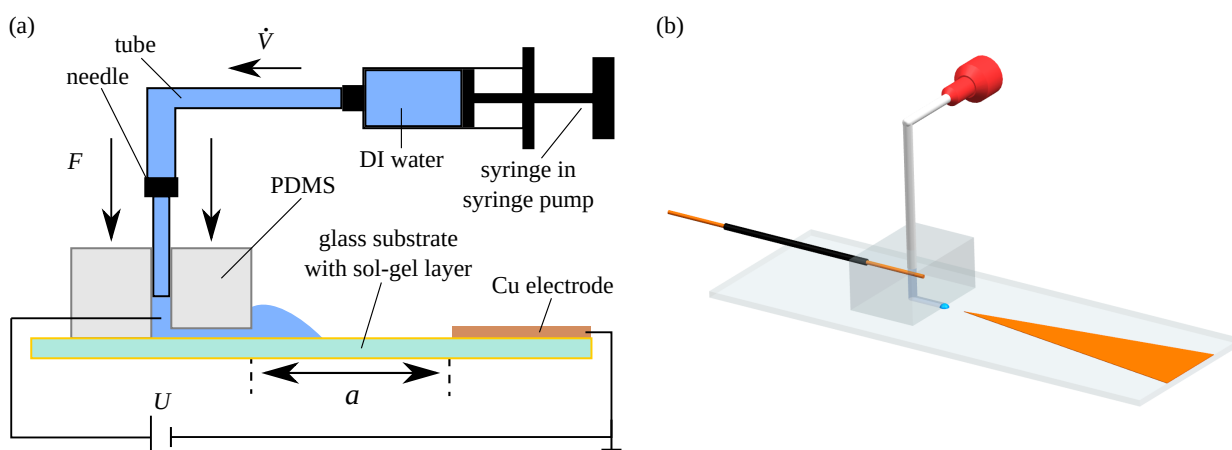


Figure 7.2: (a) Schematics of the experimental setup. To ensure a tight connection, the block of PDMS is clamped onto the substrate (indicated here) by an applied force F . (b) shows the fluid and electrical connections in more detail.

The droplet application was performed via a prepared piece of PDMS that was clamped onto the substrate after the preparation of the sol-gel layer and the copper electrode. Usually, PDMS is bonded onto glass by a plasma-bonding process. This step is not practicable in the present case since, on the one hand, the plasma treatment of the already coated surface leads to its destruction. On the other hand, bonding before spin coating cannot be performed since the PDMS piece would act as a barrier for the fluid, and, hence, it would not be possible to apply a homogeneous fluid layer during spin coating. Therefore, the PDMS piece was simply clamped onto the coated substrate to ensure a tight connection and prevent leakage. Prior to clamping, the PDMS piece was prepared by cutting it into a cuboid-like shape of about 2 cm in length and 1 cm in width and height each. A hole was pierced along the height dimension through the middle of the cuboid using a dosing needle. With a scalpel, a triangular channel with sides in the order of 1 mm was cut from the outlet of the hole towards one end of the cuboid along the width direction. The shape and the dimensions of the channel are not relevant as long as the channel outlet is small compared to the final droplet diameter. Details are shown in figure 7.2(b). The PDMS piece was then clamped onto the substrate with the outlet facing the tip of the electrode at a distance a .

The fluid connection was established by sticking the end of a flexible dosing needle (VIEWEG, Germany, flexible dosing needle 1 1/2 inch, inner diameter 0.81 mm) into the inlet of the PDMS piece at the top of the cuboid. The needle tip is made out of polypropylene instead of some metal to minimize its influence on the electric field. Via Luer Lock connections and an FEP-tube, the needle was connected to a 10 ml gastight glass syringe (model 1010 Gastight, Hamilton, USA) spanned inside a syringe pump (KD Scientific, USA, Legato 100). This assures the application of a defined flow rate \dot{V} .

A voltage U between the droplet and the electrode can be applied using a high-voltage source (Heinzinger, Germany, PNC 6000-100 ump). The copper (Cu) electrode is grounded while the droplet and the complete fluid reservoir (the liquid inside the syringe and the tubing) is electrically connected to the voltage source via a Cu-wire stitched through the PDMS piece until the tip penetrates the walls of the channel as sketched in figures 7.2(a) and (b).

7.2.2 Experimental Procedure

The prepared substrate was set onto the x - y - z -table of the benchmark configuration described in section 3.1. Then, the fluid- and electrical connections were attached, as described above. Before dosing the liquid, a constant voltage U was applied. For safety reasons, the maximum amount of current is limited to 3 mA (3 % of the maximum current of the used high voltage source). Afterward, the fluid supply was switched on by actuating the syringe pump. The flow rate was set to 0.05 $\mu\text{l/s}$, which is small enough that the volume increase can be neglected during formation of the bridge between electrode and droplet, and that the contact angle is the advancing contact angle Θ_{adv} , if no voltage is applied. Deionized (DI) water (Milli-Q, 18.2 $\text{M}\Omega\cdot\text{cm}$) was used as the fluid. The whole process was recorded by two synchronized high-speed cameras (Photron SA1.1 and SA-X2) in end-trigger mode at a frame rate of 10,000 fps. It was taken care of that the recorded image section contains the fluid outlet of the PDMS piece and the tip of the electrode for both the top and the side view. The cameras were triggered after the droplet got in (visible) contact with the electrode what can also be noticed by the experimenter as an acoustic signal. The voltage source was switched off as soon as possible afterward. Then the images were stored to the hard drive, and the next substrate was set onto the table and was readily connected.

The process is investigated for two different parameters. In particular, experiments were performed for different values of the distance between the outlet of the PDMS-piece and the electrode tip a and the applied voltage U . Experiments were performed at least five times for each set of parameters. To ensure comparability between experiments, substrates with a defined wettability were used, i.e., the substrates were produced using a molar ratio of $[\text{PEG-M}]/[\text{TEOS}] = 0.15$, as described in the protocol in section 4.3.1 that originates from [90]. Though the substrates were already characterized, the advancing and receding contact angles were measured separately for each substrate using the DSA 100 (Krüss, Germany) to perform goniometric measurements with a flow rate of 0.25 $\mu\text{l/s}$ and a maximum volume of 2.5 μl .

7.2.3 Data Evaluation

For characterization of the liquid structure that forms between the liquid outlet and the electrode, the focus lies in comparing this process between the formation of ordinary Taylor-Cones and a droplet sliding down an inclined surface. The relevant parameters are, therefore, the opening angle of the forming cone, the tips curvature, and the contact angle evolution of the droplet of the process. Therefore, side view images, as well as top view images, had to be evaluated.

Side view In the side view image evaluation, DENIISE was employed to evaluate the time series data. As input data, it takes images of droplets in contact with a substrate and extracts, among others, the contact line, i.e., the wetting radius and the contact angle (see [30] for more information). However, this software can only handle images in which the left and right side of the contact line of the two-dimensional projection of a sessile droplet does appear. Due to the nature of the experimental setup, this situation can never happen (see, e.g., the droplet sketched in figure 7.2(a), or the pictures from the experiment in figure 7.4). As a workaround, the side view images have been mirrored to imitate the left and right contact points (in 2D). Before evaluation of the images, the region of interest (ROI) can be chosen within DENIISE. By doing that in such a way that the ROI of the resulting mirrored image reaches from the tip of the electrode to the mirrored tip, the distance between the contact point and the electrode tip, denoted as b , was extracted

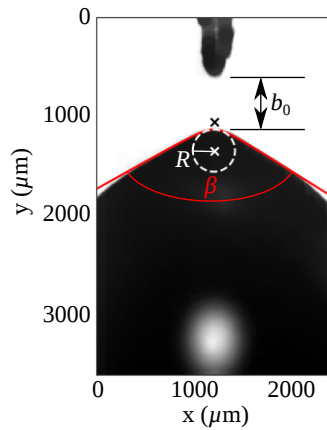


Figure 7.3: To the droplet shape fitted hyperbola and the resulting tip radius R in the moment the surface Taylor-Cone with opening angle β has formed at a distance b_0 from the electrode.

by subtracting the pseudo contact length from the image width. In addition, the contact angle Θ was calculated by DENIISE for each image of the image series for each experiment.

Top view When evaluating the top view image sequences, a manual pre-selection must be performed. Therefore, the image in which the conical shape has formed was selected by the experimenter. Since the behavior of the wetting droplet within an electric field is compared to the classical Taylor-Cone, the sign of the curvature was chosen as the selection criterion. In particular, the last image in which a convex shape in the 2D-projection of the droplet can be observed is taken as the point in time when the Surface Taylor-Cone has formed, before the curvature changes to become concave and a liquid jet emerges from the cone tip, subsequently. Initially, the opening angle of the cone β was measured manually. However, for a comparison with the shape of a sessile droplet sliding down an inclined surface, a similar evaluation of the data as in Peters et al. [143] had to be performed. In the first step of this procedure, tiny spots are removed from the images. Then, the image section in which only the cone can be seen is extracted manually. Subsequently, the contact line of the droplet and its coordinates are extracted from the image, as described in section 3.2. Then, a hyperbola is fitted to the coordinates using the least-squares method implemented in SciPy [127]. The result of one experiment can be seen in figure 7.3. From the hyperbola coefficients, the opening angle β and its tip radius R can be extracted. Since the opening angles have already been measured manually, these were taken to check the quality of the described fitting procedure. The maximum absolute derivation from the data was approximately 5° .

7.3 Results and Characterization

Figure 7.4 shows the typical behavior of a DI water droplet within the experiment. Note that not the entire process, starting from the point when the first amount of liquid leaves the PDMS piece, is captured by the cameras since these have only a limited amount of storage. However, from the first image at -1.25 s before the time when the cone is formed, from the top view, it can be seen that the droplet is almost spherical. This is also the first impression from side view images. However, a close observation of the three-phase contact line reveals a slight deviation from the spherical shape at this location. This observation fits with

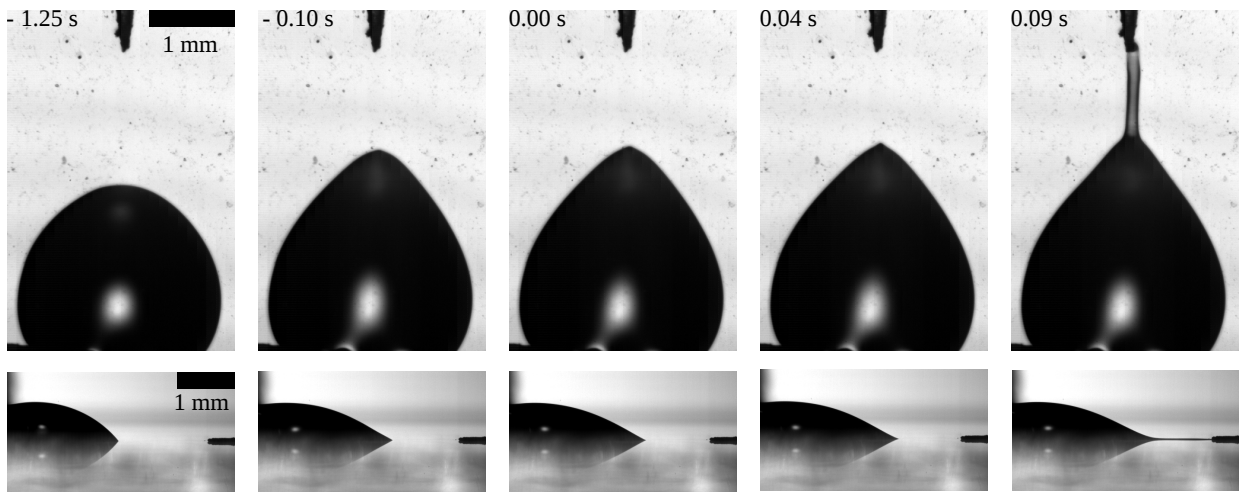


Figure 7.4: Typical evolution of the liquid surface in an electric field on a low contact angle hysteresis substrate. Here, the applied voltage $U = 3$ kV, and the distance between the fluid outlet and the electrode tip is $a = 3.5$ mm. From an initial, approximately spherical shape, a cone appears as the contact line approaches the electrode. From the tip of the cone, a liquid jet emerges towards the electrode. The moment when the cone appears is set to $t_0 = 0$ s.

the contact angle measurements showing that this state is already influenced by the Maxwell stresses due to the static electric field. Some more details about the contact angle can be found in section 7.3.2. Emerging from this state, the front part of the droplet, i.e., the part located next to the electrode tip, accelerates, and a liquid tongue forms that has a convex tip shape (-0.10 s). This convex shape changes to a concave one as presented at 0.04 s. Inbetween this shape change, a state can be observed that shows a conical shape of the tip of the tongue, at 0.00 s. Due to the similarities between ordinary Taylor-Cones and the shape evolution within the present problem, and in view of the equal governing forces that lead to the conical shape, this cone is denoted as the Surface Taylor-Cone (STC) in the present work. A detailed comparison between the opening angles in the present experiments and the unique opening angle of the Taylor-Cone is presented in section 7.3.1. However, note that this conical shape can also be observed at the rear part of a droplet sliding down an inclined surface. A comparison between this process and the experiments is made in section 7.3.3. The visual contact angle at the moment when the STC appears is smaller

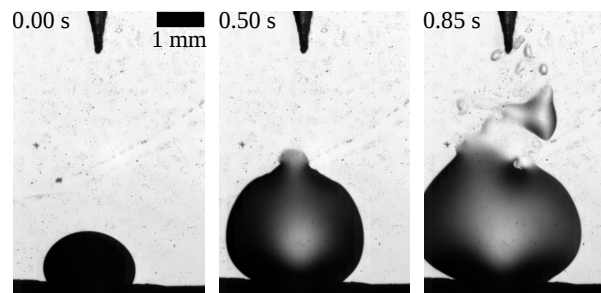


Figure 7.5: Typical evolution of the liquid surface in an electric field on an untreated glass surface. Since no definite time t_0 can be defined, the time starts with the first image. Experimental properties were $U = 4$ kV, and $a = 4.5$ mm.

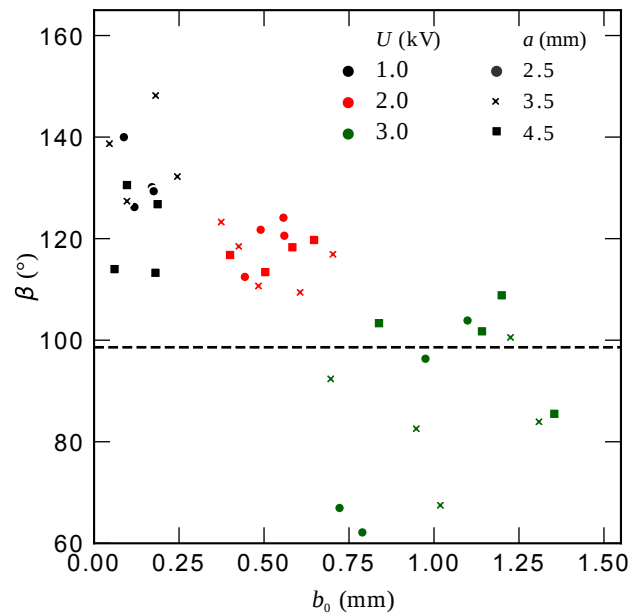


Figure 7.6: Opening angles β of the STC as a function of the distance b_0 between the tip of the cone and the electrode for different applied voltages U and distances a between the PDMS outlet and electrode tip. Each dot represents one experiment. The dashed line is the unique Taylor-Cone angle, as calculated by G.I. Taylor (98.6°) [28] in the absence of a three-phase contact line.

than the initially measurable one, at -1.25 s. After the cone has formed, a liquid jet emerges from the tip of the cone towards the electrode and gets in contact with it (0.09 s). This is when the experiment is stopped.

In contrast to the substrate with low contact angle hysteresis of figure 7.4, figure 7.5 shows experimental images when the uncoated glass is used with a contact angle hysteresis that is about four times larger. Also here, the liquid accelerates towards the electrode and a typical tongue forms. However, no cone can be observed. Instead, something that looks like a liquid film can be observed with some parts being pinched off from the liquid main body. Note that this experiment had to be performed at $U = 4$ kV to see any relevant effects that are remotely similar to those of the STC-forming in figure 7.5.

7.3.1 Opening Angles

In order to characterize the Surface Taylor-Cones, the opening angles of the STCs are compared with the one from the classical Taylor-Cone as it originates from theoretical considerations by G. I. Taylor [28]. If a droplet is located at a conical needle tip and an electrostatic force acts on the droplet, then this droplet forms a conical shape at a specific applied voltage between the electrode and the droplet, whose opening angle is 98.6° . The opening angles β originating from the STC's are plotted in figure 7.6 against the distance b_0 between the tip of the cone and the electrode. Different applied voltages U , and distances a between the electrode and the fluid outlet of the PDMS-piece are considered. It can be seen that the scattering of data is relatively high. However, clusters within the chosen space can be observed that are unambiguously disjunct from each other and depend on the applied voltage. The opening angles decrease, and the distance b_0 increases for increased potential differences U . According to our measurements, the parameter a does not influence the opening angle and the distance b_0 . Therefore, it can be concluded

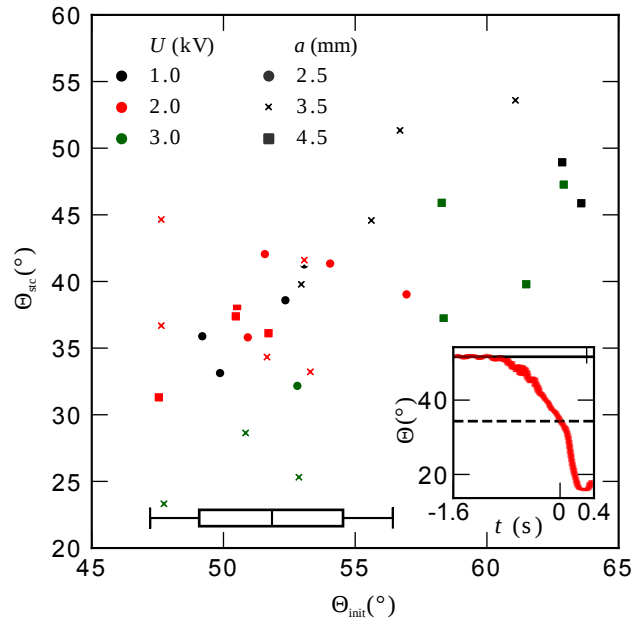


Figure 7.7: Contact angle Θ_{STC} at the moment of the appearance of the STC over the initially measured contact angle Θ_{init} for different applied voltages U and distances a between the PDMS outlet and electrode tip. Each dot represents one experiment. As a reference, the receding contact angle, as measured in goniometric experiments is shown as a box plot (vertical line: mean value - box: standard deviation - error bars: absolute error (symmetric)). The inset shows a typical evolution of the contact angle Θ as a function of time. In it, the solid line marks the extracted Θ_{init} and the dashed line the Θ_{STC} .

that the droplet size at the moment the cone forms does not influence β . When the measured values of the opening angles are compared to the one of the regular Taylor-Cone, it can be seen that for an applied voltage of 1 kV and 2 kV, β is larger than 98.6° . For $U = 3\text{ kV}$, β scatters around the theoretical value for the Taylor-Cone. However, the scattering is large, and therefore, no definite conclusion concerning this matter can be drawn.

7.3.2 Contact Angles

Figure 7.7 shows the contact angle Θ_{STC} of the droplet at the moment the STC has formed as a function of the initial contact angle Θ_{init} . These are determined from the data as depicted in the inset that shows a typical evolution of the front contact angle as a function of time. Initially, between approximately 1.5 s and 1 s before the STC appears, the contact angle is constant, and can be determined as Θ_{init} . Since the frame when the STC appears is known from the top view recordings, the contact angle Θ_{STC} can be extracted directly by comparing the relevant frame from the side view images with the one from the top view (the image sequences in top- and side view are synchronized). The advancing and receding contact angles Θ_{adv} and Θ_{rec} were determined in separate experiments for each substrate using the DSA 100 (Krüss, Germany). Θ_{adv} was determined to be $63.4^\circ \pm 2.2^\circ$, while Θ_{rec} was measured to be $51.8^\circ \pm 2.8^\circ$. These values agree well with the ones obtained in section 4.3.1. The mean receding contact angle is also depicted in figure 7.7 as a vertical solid line within a box, while the width of the box represents the standard deviation and the error bars the maximum symmetric error in the contact angle measurement experiments. It is obvious

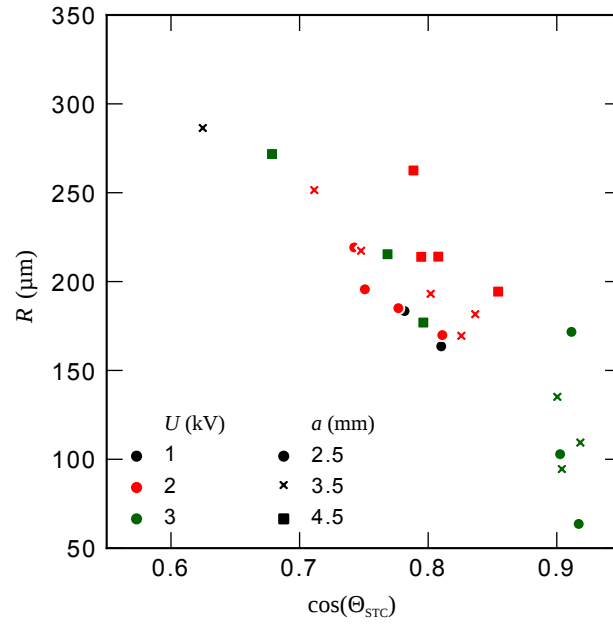


Figure 7.8: Evaluation of the tip radius of the STC. The radius is compared with the stresses resulting from the electric field taking $\cos(\Theta_{\text{STC}})$ as a measure for it.

that, though the contact line is in an advancing state when the initial contact angle is measured in the STC experiments, it does not adopt the advancing contact angle Θ_{adv} . In fact, the contact angles scatter between Θ_{adv} and Θ_{rec} . This indicates that the electric field already influences the droplet before the liquid tongue accelerates towards the electrode. From electrowetting, it is known that the contact angle is decreased when an external electric field is applied in the normal direction to the substrate (see, e.g., [26]). Though the field is directed horizontally to the substrate surface in the present case, some similar effects might play a role here. On the other hand, preliminary, accompanying simulations by Maximilian Schür indicate that it is possible that a liquid film forms between the droplet and the electrode. However, this film has a thickness below the resolution limit of the used optics and, hence, can not be verified with the present setup. Nevertheless, this can also be a reason for a decreased contact angle and may fit into the precursor film framework [144]. The determined values of Θ_{STC} are all below Θ_{rec} . From our measurements, a trend can be derived that Θ_{STC} increases for increased Θ_{init} . However, there seems to be no influence of the applied voltage nor the droplet size.

7.3.3 Tip Radius

Another essential property of a cone is its tip radius R , which is plotted over $\cos(\Theta_{\text{STC}})$ in figure 7.8(a). The contact angle of the droplet in its equilibrium shape is described by Young's equation (2.21). If σ_s is increased, then $\cos(\Theta_{\text{STC}})$ decreases, assuming that all other parameters stay constant. The same effect can be observed when an external tension is applied. Therefore, $\cos(\Theta_{\text{STC}})$ is chosen since it can be interpreted as a measure of the force due to the electric field acting on the three-phase contact line, though it has a non-negligible velocity. It can be seen that R decreases with increasing $\cos(\Theta_{\text{STC}})$, and therefore increasing external tensions. However, the tip radius of the cone seems to be independent of the applied voltage, as well as on the parameter a . At a first glance, this is not intuitive as the force on the droplet should scale linearly with U since the electric field does so, too. However, no definitive statement on the electric field can

be made since the electrode tip shape is difficult to reproduce with the copper tape, though it was taken care off that it was always cut with a defined angle (for an example compare the electrodes in figures 7.4 and 7.5).

An analogous droplet shape as the conical one from the Surface Taylor-Cones can also be observed in the case of droplets sliding down an inclined surface [142]. At the rear part of these droplets, a cone-like liquid shape forms similar to those observed in the present experiments. The tip radius R of the cone, and, therefore, the curvature $1/R$ assigned to it, depends on the droplet velocity and, hence, the viscous stresses. These stresses could be understood as an analogous tension due to the electric stresses that are assumed to be located almost entirely at the three-phase contact line due to corner effects [16]. The latter assumption is supported by the experimental observations shown in the side view images in figure 7.4 where the Maxwell stresses seem to be pre-dominant at the three-phase contact line. The appropriate dimensionless number, in the case of droplets sliding down an inclined surface, is the capillary number Ca , which compares viscous and surface tensions, i.e., $Ca = u\eta/\sigma$, with velocity u and viscosity η . According to Cox and Voinov [145], the capillary number in the case of spreading droplets can be calculated as

$$Ca = \frac{\Theta_e^3 - \Theta^3}{9 \ln\left(\frac{l_{\text{mac}}}{l_e}\right)}, \quad (7.1)$$

with $\ln\left(\frac{l_{\text{mac}}}{l_e}\right)$ being a parameter that compares two length scales at the contact line and is usually taken as a fitting parameter. Θ_e is the equilibrium contact angle and Θ being the contact angle that actually can be measured during the spreading process. Peters et al. [143] exploit equation (7.1) by assuming that Θ_e is the receding contact angle Θ_{rec} at the rear part of the droplet since it is sliding down an inclined surface. The authors found that the tip radius of the hyperbola they fitted to the cone shape at the receding side of a sliding droplet can be calculated as

$$R = l_{\text{mic}} \exp\left(\frac{\Theta_e^3}{9Ca}\right), \quad (7.2)$$

with l_{mic} being another length on the molecular scale that is taken as an additional fitting parameter, as suggested by Peters et al. [143], and Ca being calculated with equation (7.1).

In the situation when the STC appears in the present case, the contact line is advancing. The equilibrium contact angle in equation (7.1) is, therefore, assumed to be the advancing contact angle, $\Theta_e = \Theta_{\text{adv}}$, in order to compare the above model with the present case. Θ is the contact angle at the particular moment when the STC appears, i.e. $\Theta = \Theta_{\text{STC}}$. Subsequently, by combining equations (7.1) and (7.2), R can be expressed as a function of Θ_{STC} . Since both parameters can be measured for each experiment (see data in figure 7.8), the model can be fitted to the experimental data using the least-squares method. The best fit to the data and the data itself is presented in figure 7.9(a) as the solid line. Note that in this case the capillary number Ca of the data points can be read from the bottom axis. It is calculated with equation (7.1) with the parameters found in the best fit, which are summarized in table 7.1 (Peters et al.).

From a comparison of these data and figure 7.9(a), it can be seen that the present problem cannot be described in this relatively simple framework, and the analogon between viscous and Maxwell stresses does not hold. By modifying equation (7.2) by adding an additional fitting parameter o that simply is an offset, i.e.,

$$\frac{1}{R} = \frac{1}{l_{\text{mic}} \exp\left(\frac{\Theta_e^3}{9Ca}\right)} + o, \quad (7.3)$$

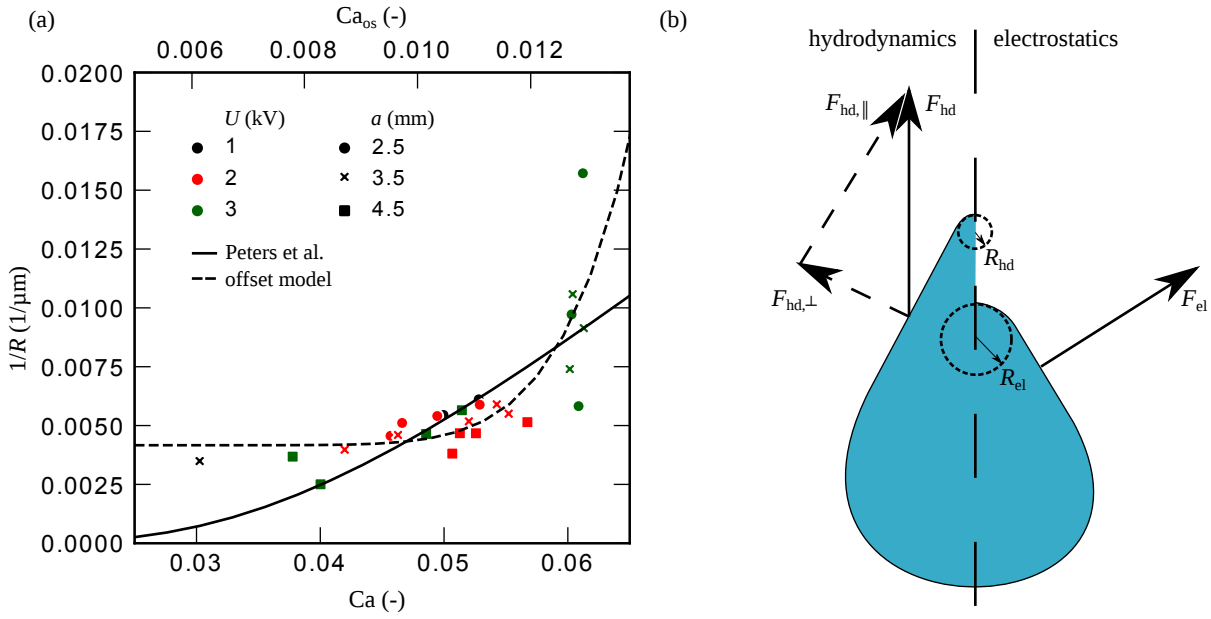


Figure 7.9: Comparison of the experimental data to the model of Peters et al. [143] (solid line, bottom axis) and the offset model (dashed line, top axis) in (a). (b) shows a sketch of the differences of the governing forces in the STC-problem F_{el} and the hydrodynamic force (F_{hd}) acting in case of the model by Peters et al. that might lead to different tip radii R_{el} and R_{hd} , respectively.

the experimental data can be fitted well, as depicted with the dashed line in figure 7.9(a). The corresponding capillary number Ca_{0s} can be read from the top axis in that case and the fitting parameters are presented in table 7.1 (offset model). However, this would mean that for $Ca \rightarrow 0$, and, therefore, for a negligible contact line velocity, a cone like tip would exist with a measurable inverse radius, which is not the case. On the other hand, this offset may be a hint for the influence of the electric field, prior electric stresses lead to an acceleration of the liquid. This influence is measurable in the contact angle (see section 7.3.2). Nevertheless, then the above described model can unlikely be used for describing the process. Moreover, though the assumption that the Maxwell stress is located almost entirely at the three-phase contact line is reasonable, there is one difference between this kind of stresses and the viscous ones (see figure 7.9(b)). While Maxwell stresses are directed normal to the surface, and therefore normal to the three-phase contact line in the substrate plane, viscous stresses do also have a tangential part at every location of the contact line that does not move in the parallel direction to the droplets velocity vector. In particular, this is every point that is not located at the center axis of the droplet. This might also lead to differences for the tip radius R . Moreover, in the STC problem, the force acting against the Maxwell stress (not depicted in figure 7.9(b)) is the viscous force itself while in the sliding drop problem, the force acting against the viscous force is the

Table 7.1: Fitting parameters from the model by Peters et al. [143], an extended one (offset model), and their reference values.

	Peters et al.	offset model	reference value	source
$\ln \left(\frac{l_{mac}}{l_{\Theta}} \right)$	2.33	11.1	$\ln 10^4$	[146]
l_{mic} (μm)	9.38	0.0014	0.01	[143]
o (1/μm)	-	0.00416	-	-

gravity. The latter one is a volume force, while all other forces are surface forces. Finally, the contact line is in an advancing state in the STC problem, while it recedes in the sliding droplet problem.

7.4 Conclusion and Outlook

An experimental setup was developed with which it was possible to show the existence of Surface Taylor Cones (STC). To the best knowledge of the author, this has been described for the first time. In particular, Taylor-Cones in contact with a substrate do appear due to the interplay between the surface tension of the liquid and a horizontal electric field between the electrode and the droplet. Throughout all the experiments, DI water was used as a liquid. Hydrophilic substrates with a defined advancing and receding contact angle, and a contact angle hysteresis of about 10° were fabricated for that purpose. The STCs could only be produced reliably on these kinds of substrates. On substrates with larger hysteresis, in particular ordinary, pristine glass surfaces, no STCs could be observed, though the presence of the electric field led to a deformation of the capillary surface. To characterize these surfaces, cone properties, i.e., its opening angle, tip radius, and contact angle, as well as contact angle information before and after the cone developed, were extracted from the top- and side view image data. It could be shown that the opening angle of the cone is not unique, like the one from the classical Taylor Cone, but depends on the applied voltage, and *not* on the droplet size. The contact angle evolution at the three-phase contact line reveals that the electric field already influences the wetting behavior of the droplet before the liquid accelerates towards the electrode. However, the applied voltage and the droplet size have no influence on the contact angle at the moment when the STC appears. An attempt was made to compare the cone with the one that appears at a rear part of a droplet sliding down an inclined surface. However, this comparison shows that the forces due to viscous stresses and because of an electric field could not be brought entirely into accordance. However, the data reveals a correlation between the tip radius and the STC's contact angle.

Further experiments are needed to reduce the scattering of the data points and to extract additional information. First of all, the electrode design must be improved, and better repeatability must be achieved together with fast availability and high throughput. Due to the latter two points, photolithography with subsequent sputtering is not the right choice. However, electrically conductive adhesives could be used in combination with a mask. This assures a more repeatable electrode design. It must be tested if it is possible to apply the adhesive onto the sol-gel layer. In order to test whether a liquid film of small thickness below the resolution limit of the optical setup appears prior to the contact of the liquid with the electrode (as suggested by preliminary simulation results), the conductivity between the electrode and the droplet must be measured. This measurement must be synchronized with the image sampling. Finally, it could be tested how the absolute contact angle influences the behavior of the cone. By mixing the main components of the coating solution at a different ratio, this is possible without significantly changing the contact angle hysteresis (see section 4.3.1).

8 Concluding Remarks

In the present work, the wetting behavior of droplets on chemically striped pattern surfaces and in an electric field was studied experimentally, numerically, and based on models. For experiments, an experimental setup was planned and constructed that allows the simultaneous observation of wetting processes from two sides, in particular, from the top and bottom perspective. The optical setup allows a spatial resolution in the micrometer range and temporal resolutions in the order of a few 10,000 fps. The observed process may optionally but not necessarily occur within a humidified atmosphere that can be set within a climate chamber. Since it also serves as a central benchmark configuration within the Collaborative Research Centre 1194, the setup was constructed to be equipped with different apparatus, e.g., a droplet dosing unit, to allow maximum flexibility for experiments that can be performed within the benchmark configuration. Moreover, it was taken care of that individual units can be used within other setups.

To obtain the desired wetting behavior, different surface modification techniques were applied. In the case of the patterned surface, an apparatus, i.e., a low-pressure chemical vapor deposition chamber, was designed that allows the deposition of the silanes from the vapor phase at defined conditions [58]. These silanes chemically bond to the silicon and glass surfaces and lower the surface energy on the regions where they are deposited. By using this technique, repeatable wetting conditions were achieved on the hydrophobic regions reliably. When neighboring substrate regions are covered, these are protected from the vapor atmosphere and keep their original wetting behavior (hydrophilic). This allowed producing chemically patterned surfaces with striped regions of different wettability. Besides these substrates, hydrophilic surfaces with low contact angle hysteresis were produced by applying the protocol by Kaneko et al. [90] This modification technique seems to be the only one that allows water contact angles on solid surfaces well below 90° and, at the same time, small contact angle hysteresis in the order of 10° . Both techniques were tested by characterizing the resulting substrates in their relevant surface properties. In particular, the surface wettability was tested with water, and in the case of the silane, the monolayer quality was verified. For the silanes, the wettability was measured as it is known from the literature, and the monolayer thickness was determined to be in the order of a molecule length of the respective silane. Both indicate that the silanization within the self-build CVD-chamber works reliably. In the case of the hydrophilic surfaces with low contact angle hysteresis, it was found that the contact angle values from Kaneko et al. [90] could only be measured on the modified silicon wafers. However, using microscopy glass slides as carrier substrates, substrates with repeatable advancing and receding contact angle could be produced with a contact angle hysteresis of about 10° .

On a striped pattern surface with a droplet wetting a width much larger than the stripe width, a breakup of the evaporating droplet could be observed while it evaporates. To the best knowledge of the author, this was the first evident experimental proof of the instability of an evaporating sessile droplet on a substrate due to its chemical inhomogeneity. To further investigate the instability criteria, the stripe width was increased so that the droplet wetted three stripes in the order hydrophilic-hydrophobic-hydrophilic. A Surface Evolver model was set up, including an automatic routine that accompanied the experimental

investigations. These numerical calculations made it possible to identify two wetting contrast regimes. In particular, a stable and unstable regime within the wetting space of the hydrophilic and hydrophobic contact angle was found. This was confirmed from experiments for all accomplishable contact angle contrasts. Further experiments of evaporating droplets on an alternating stripe pattern with different absolute stripe widths and stripe width ratios were performed within the unstable branch. These droplets form an H-shape with the capillary bridge spanning (and being in contact with) the hydrophobic stripe, which is located between the two liquid fingers sitting on the two adjacent hydrophilic stripes. During evaporation, the capillary bridge width decreases until it becomes unstable at a certain width. To further investigate the stability limits of this setup, the experiments were accompanied by a numerical study with the Surface Evolver and a simple scaling model that compares the pressures within the capillary bridge and the liquid above the hydrophilic stripe. The application of the scaling model revealed that the bridge is stable, as long as its width is above a critical value, below which the Laplace equation does not have a solution anymore. In an energetic sense, this means that below the critical bridge width, it is more favorable for the droplet to wet two disjoint hydrophilic stripes instead of some additional parts of the hydrophobic one. This was confirmed by the Surface Evolver, which validates the model results. Both, the model and Surface Evolver simulations confirm the experimental measurements quantitatively. The obtained results can be used to improve multi-layer inkjet printing processes or printing onto pre-patterned surfaces, among others. In particular, the numerically calculated and experimentally validated border between a wetting contrast region leading to breakup of the evaporating droplets, and one leading to no breakup, allows to choose material combinations that enable to produce a clean printed surface or to precisely guide ink to its desired location. Furthermore, the scaling model allows a fast estimation of the stability limits within the unstable regime. Since ink has more complex fluid properties than water, in future works it could be investigated how evaporating fluid mixtures behave on the striped pattern. Possible suppression of the breakup might occur due to Marangoni-effects. Moreover, phase-separation of complex fluids might lead to a split-up.

The breakup behavior of the capillary bridge was investigated in more detail. For that purpose, the experiments were accompanied by VOF-simulations. This was the first-ever detailed investigation of the breakup dynamics of a capillary bridge in contact with a rigid substrate oriented along the bridge axis, as far as the author knows. In particular, the breakup process was studied applying the phase space analysis, which removes the uncertainty of the choice of the exact breakup time. It was found that capillary and inertial forces govern the overall dynamics within the chosen set of parameters. After a short initial phase after the capillary bridge becomes unstable, the breakup can be roughly described by the well-known $d \sim t^{2/3}$ -scaling, indicating that viscous forces do not play any role. After a regime transition, a $d \sim t^{0.48}$ - $d \sim t^{0.54}$ -scaling could be found, depending on the observed parameter. The regime transition is accompanied by a shape change of the capillary bridge from a catenoid-like shape towards a liquid thread between two conical liquid shapes. In the phase space analysis, the transition can be identified in a local minimum of the breakup speed. It was found that the final liquid thread breaks up in a Rayleigh-Plateau-type instability leaving behind some satellite droplets in the middle of the hydrophobic stripe.

The hydrophilic surfaces with low contact angle hysteresis were used to demonstrate the existence of Surface Taylor-Cones (STC), i.e., Taylor-Cones in contact with a solid substrate. It was shown that these can only be formed between a droplet and an electrode at different electric potentials when the difference between the advancing and receding contact angle is small enough. The opening angle of the cone depends on the applied voltage but not on the droplet size. No unique opening angle, like the one calculated by G. I. Taylor for the free Taylor-Cone, could be observed. By measuring the contact angle over the whole process, it could be revealed that the electric field already influences the contact angle before the three-phase contact line and the liquid is accelerated towards the electrode due to the applied electric

field. A further attempt was made to explain the cone by comparing it with the cone shape that appears at the rear part of a droplet sliding down an inclined surface for which a model exists [143]. It could be shown that only a poor comparison with this model is possible. However, when an offset in the curvature of the cone tip is introduced, the fitting parameters suite reasonably with values from the literature. It was hypothesized that the difference may be due to tangential forces at the three-phase contact line present in the case of the droplet sliding down an inclined surface, but not in the STC case, where only normal forces are pre-dominant. Nevertheless, it is worth investigating the STC extensively, since it could open the way for performing two-dimensional electrospinning in an easy manner. Future works may also include the influence of the wettability of the substrate on the structure of the STC. The used hydrophilic coating is suited well for these experiments since it was shown that the mean water contact angle can be changed, but the contact angle hysteresis stays constant for different ratios of the main components of the coating solution on the microscopy slides. Moreover, the conductivity between the two electrodes can be measured simultaneously with the image recording. This would allow gaining information on liquid transport processes that occur on a length scale that cannot be captured by the currently used optical setup. Finally, the influence of the three-phase contact line on the merging or recoiling of two sessile droplets at different potential could be investigated.

Bibliography

- [1] Fischer, S. R., *A History of Writing*, Globalitie; Reaktion Books: London, 2004.
- [2] Kim, J.; Moon, M.-W.; Lee, K.-R.; Mahadevan, L.; Kim, H.-Y. Hydrodynamics of Writing with Ink. *Physical Review Letters* **2011**, *107*, 264501, DOI: 10.1103/PhysRevLett.107.264501.
- [3] Kang, B.; Lee, W. H.; Cho, K. Recent Advances in Organic Transistor Printing Processes. *ACS Applied Materials & Interfaces* **2013**, *5*, 2302–2315, DOI: 10.1021/am302796z.
- [4] Kumar, S. Liquid Transfer in Printing Processes: Liquid Bridges with Moving Contact Lines. *Annual Review of Fluid Mechanics* **2015**, *47*, 67–94, DOI: 10.1146/annurev-fluid-010814-014620.
- [5] Calvert, P. Inkjet Printing for Materials and Devices. *Chemistry of Materials* **2001**, *13*, 3299–3305, DOI: 10.1021/cm0101632.
- [6] Bower, C. L.; Simister, E. A.; Bonnist, E.; Paul, K.; Pightling, N.; Blake, T. D. Continuous coating of discrete areas of a flexible web. *AIChE Journal* **2007**, *53*, 1644–1657, DOI: 10.1002/aic.11215.
- [7] Zhang, L.; Wu, J.; Hedhili, M. N.; Yang, X.; Wang, P. Inkjet printing for direct micropatterning of a superhydrophobic surface: toward biomimetic fog harvesting surfaces. *Journal of Materials Chemistry A* **2015**, *3*, 2844–2852, DOI: 10.1039/C4TA05862C.
- [8] Hamilton, W. J.; Seely, M. K. Fog basking by the Namib Desert beetle, *Onymacris unguicularis*. *Nature* **1976**, *262*, 284–285, DOI: 10.1038/262284a0.
- [9] Parker, A. R.; Lawrence, C. R. Water capture by a desert beetle. *Nature* **2001**, *414*, 33–34, DOI: 10.1038/35102108.
- [10] Edalatpour, M.; Liu, L.; Jacobi, A.; Eid, K.; Sommers, A. Managing water on heat transfer surfaces: A critical review of techniques to modify surface wettability for applications with condensation or evaporation. *Applied Energy* **2018**, *222*, 967–992, DOI: 10.1016/j.apenergy.2018.03.178.
- [11] Zeng, X.; Qian, L.; Yuan, X.; Zhou, C.; Li, Z.; Cheng, J.; Xu, S.; Wang, S.; Pi, P.; Wen, X. Inspired by *Stenocara* Beetles: From Water Collection to High-Efficiency Water-in-Oil Emulsion Separation. *ACS Nano* **2017**, *11*, 760–769, DOI: 10.1021/acsnano.6b07182.
- [12] Beyazkılıç, P.; Tuvshindorj, U.; Yildirim, A.; Elbuken, C.; Bayindir, M. Robust superhydrophilic patterning of superhydrophobic ormosil surfaces for high-throughput on-chip screening applications. *RSC Advances* **2016**, *6*, 80049–80054, DOI: 10.1039/C6RA19669A.
- [13] De Gennes, P.-G.; Brochard-Wyart, F.; Quéré, D., *Capillarity and Wetting Phenomena*; Springer New York: New York, NY, 2004, DOI: 10.1007/978-0-387-21656-0.
- [14] Butt, H.-J.; Graf, K.; Kappl, M., *Physics and Chemistry of Interfaces*; Wiley: Weinheim, 2003, DOI: 10.1002/3527602313.
- [15] Láng, G. G. Basic interfacial thermodynamics and related mathematical background. *ChemTexts* **2015**, *1*, 16, DOI: 10.1007/s40828-015-0015-z.

- [16] Mugele, F.; Heikenfeld, J., *Electrowetting*; Wiley-VCH Verlag GmbH & Co. KGaA: Weinheim, Germany, 2018, DOI: 10.1002/9783527412396.
- [17] Gibbs, J. W. *The collected works of J. Willard Gibbs*. Tech. rep.; Yale Univ. Press, 1948.
- [18] Berthier, J.; Brakke, K. A., *The Physics of Microdroplets*; John Wiley & Sons, Inc.: Hoboken, NJ, USA, 2012, DOI: 10.1002/9781118401323.
- [19] Bruus, H., *Theoretical Microfluidics*; Oxford University Press: Oxford, Toronto, 2009.
- [20] Plateau, J., *Statique expérimentale et théorique des liquides soumis aux seules forces moléculaires*; Gauthier-Villars: 1873; Vol. 2.
- [21] Rayleigh, L. On The Instability Of Jets. *Proceedings of the London Mathematical Society* **1878**, *s1-10*, 4–13, DOI: 10.1112/plms/s1-10.1.4.
- [22] Tabeling, P.; Suelin, C., *Introduction to microfluidics*; Oxford University Press: New York, 2005.
- [23] Drazin, P. G., *Introduction to Hydrodynamic Stability*; Cambridge University Press: 2002, DOI: 10.1017/CB09780511809064.
- [24] Gao, N.; Geyer, F.; Pilat, D. W.; Wooh, S.; Vollmer, D.; Butt, H.-J.; Berger, R. How drops start sliding over solid surfaces. *Nature Physics* **2018**, *14*, 191–196, DOI: 10.1038/nphys4305.
- [25] Style, R. W.; Boltyskiy, R.; Che, Y.; Wettlaufer, J. S.; Wilen, L. A.; Dufresne, E. R. Universal Deformation of Soft Substrates Near a Contact Line and the Direct Measurement of Solid Surface Stresses. *Physical Review Letters* **2013**, *110*, 066103, DOI: 10.1103/PhysRevLett.110.066103.
- [26] Mugele, F.; Baret, J.-C. Electrowetting: from basics to applications. *Journal of Physics: Condensed Matter* **2005**, *17*, R705–R774, DOI: 10.1088/0953-8984/17/28/R01.
- [27] Bird, J. C.; Ristenpart, W. D.; Belmonte, A.; Stone, H. A. Critical angle for electrically driven coalescence of two conical droplets. *Physical Review Letters* **2009**, *103*, 1–4, DOI: 10.1103/PhysRevLett.103.164502.
- [28] Taylor, G. Disintegration of water drops in an electric field. *Proceedings of the Royal Society of London. Series A. Mathematical and Physical Sciences* **1964**, *280*, 383–397, DOI: 10.1098/rspa.1964.0151.
- [29] Zeleny, J. Instability of Electrified Liquid Surfaces. *Physical Review* **1917**, *10*, 1–6, DOI: 10.1103/PhysRev.10.1.
- [30] Heinz, M.; Stephan, P.; Gambaryan-Roisman, T. Influence of nanofiber coating thickness and drop volume on spreading, imbibition and evaporation. *in preparation* **2020**.
- [31] Demtröder, W., *Experimentalphysik 2*; Springer-Lehrbuch; Springer Berlin Heidelberg: Berlin, Heidelberg, 2013, DOI: 10.1007/978-3-642-29944-5.
- [32] Navitar 12X Zoom Performance Specifications, Navitar, technical sheet, 2020.
- [33] Schindelin, J. et al. Fiji: an open-source platform for biological-image analysis. *Nature Methods* **2012**, *9*, 676–682, DOI: 10.1038/nmeth.2019.
- [34] Schneider, C. A.; Rasband, W. S.; Eliceiri, K. W. NIH Image to ImageJ: 25 years of image analysis. *Nature Methods* **2012**, *9*, 671–675, DOI: 10.1038/nmeth.2089.
- [35] Rueden, C. T.; Schindelin, J.; Hiner, M. C.; DeZonia, B. E.; Walter, A. E.; Arena, E. T.; Eliceiri, K. W. ImageJ2: ImageJ for the next generation of scientific image data. *BMC Bioinformatics* **2017**, *18*, 529, DOI: 10.1186/s12859-017-1934-z.

- [36] Ríos-López, I.; Karamaoynas, P.; Zabulis, X.; Kostoglou, M.; Karapantsios, T. D. Image analysis of axisymmetric droplets in wetting experiments: A new tool for the study of 3D droplet geometry and droplet shape reconstruction. *Colloids and Surfaces A: Physicochemical and Engineering Aspects* **2018**, *553*, 660–671, DOI: 10.1016/j.colsurfa.2018.05.098.
- [37] Van der Walt, S.; Schönberger, J. L.; Nunez-Iglesias, J.; Boulogne, F.; Warner, J. D.; Yager, N.; Gouillart, E.; Yu, T. scikit-image: image processing in Python. *PeerJ* **2014**, *2*, e453, DOI: 10.7717/peerj.453.
- [38] Canny, J. A Computational Approach to Edge Detection. *IEEE Transactions on Pattern Analysis and Machine Intelligence* **1986**, *PAMI-8*, 679–698, DOI: 10.1109/TPAMI.1986.4767851.
- [39] Chityala, R., *Image Processing and Acquisition using Python*; Chapman and Hall/CRC: New York, 2014, pp 1–351, DOI: 10.1201/b16533.
- [40] Sobel, I. History and definition of the so-called "sobel operator", more appropriately named the sobel-feldman operator. Sobel, I., Feldman, G., "A 3x3 isotropic gradient operator for image processing", presented at the stanford artificial intelligence project (SAIL) in 1968 **2015**.
- [41] Brakke, K. A. The Surface Evolver. *Experimental Mathematics* **1992**, *1*, 141–165, DOI: 10.1080/10586458.1992.10504253.
- [42] Chen, Y.; Schaffer, B.; Weislogel, M.; Zimmerli, G. In *49th AIAA Aerospace Sciences Meeting including the New Horizons Forum and Aerospace Exposition*, American Institute of Aeronautics and Astronautics: Reston, Virginia, 2011, DOI: 10.2514/6.2011-1319.
- [43] Bai, H.; Ju, J.; Zheng, Y.; Jiang, L. Functional Fibers with Unique Wettability Inspired by Spider Silks. *Advanced Materials* **2012**, *24*, 2786–2791, DOI: 10.1002/adma.201200289.
- [44] Chen, H.; Ran, T.; Gan, Y.; Zhou, J.; Zhang, Y.; Zhang, L.; Zhang, D.; Jiang, L. Ultrafast water harvesting and transport in hierarchical microchannels. *Nature Materials* **2018**, *17*, 935–942, DOI: 10.1038/s41563-018-0171-9.
- [45] Barthlott, W.; Neinhuis, C. Purity of the sacred lotus, or escape from contamination in biological surfaces. *Planta* **1997**, *202*, 1–8, DOI: 10.1007/s004250050096.
- [46] Bliznyuk, O.; Vereshchagina, E.; Kooij, E. S.; Poelsema, B. Scaling of anisotropic droplet shapes on chemically stripe-patterned surfaces. *Physical Review E* **2009**, *79*, 041601, DOI: 10.1103/PhysRevE.79.041601.
- [47] Bliznyuk, O.; Jansen, H. P.; Kooij, E. S.; Poelsema, B. Initial Spreading Kinetics of High-Viscosity Droplets on Anisotropic Surfaces. *Langmuir* **2010**, *26*, 6328–6334, DOI: 10.1021/la903205e.
- [48] Bliznyuk, O.; Jansen, H. P.; Kooij, E. S.; Zandvliet, H. J. W.; Poelsema, B. Smart Design of Stripe-Patterned Gradient Surfaces to Control Droplet Motion. *Langmuir* **2011**, *27*, 11238–11245, DOI: 10.1021/la201671w.
- [49] Kooij, E.; Jansen, H.; Bliznyuk, O.; Poelsema, B.; Zandvliet, H. Directional wetting on chemically patterned substrates. *Colloids and Surfaces A: Physicochemical and Engineering Aspects* **2012**, *413*, 328–333, DOI: 10.1016/j.colsurfa.2011.12.075.
- [50] Jansen, H. P.; Sotthewes, K.; Ganser, C.; Zandvliet, H. J. W.; Teichert, C.; Kooij, E. S. Shape of Picoliter Droplets on Chemically Striped Patterned Substrates. *Langmuir* **2014**, *30*, 11574–11581, DOI: 10.1021/la502212f.
- [51] Jansen, H. P.; Zandvliet, H. J.; Kooij, E. S. Evaporation of elongated droplets on chemically stripe-patterned surfaces. *International Journal of Heat and Mass Transfer* **2015**, *82*, 537–544, DOI: 10.1016/j.ijheatmasstransfer.2014.11.028.

- [52] Eifert, A.; Petit, J.; Baier, T.; Bonaccorso, E.; Hardt, S. Inscribing wettability gradients onto polymer substrates with different stiffness using corona discharge in point-to-plane geometry. *Applied Surface Science* **2015**, *330*, 104–110, DOI: 10.1016/j.apsusc.2014.12.169.
- [53] Qin, D.; Xia, Y.; Whitesides, G. M. Soft lithography for micro- and nanoscale patterning. *Nature Protocols* **2010**, *5*, 491–502, DOI: 10.1038/nprot.2009.234.
- [54] Lee, S. H.; Rho, W. Y.; Park, S. J.; Kim, J.; Kwon, O. S.; Jun, B. H. Multifunctional self-assembled monolayers via microcontact printing and degas-driven flow guided patterning. *Scientific Reports* **2018**, *8*, 1–8, DOI: 10.1038/s41598-018-35195-9.
- [55] Sagiv, J. Organized monolayers by adsorption. 1. Formation and structure of oleophobic mixed monolayers on solid surfaces. *Journal of the American Chemical Society* **1980**, *102*, 92–98, DOI: 10.1021/ja00521a016.
- [56] Brasjen, B.; van Cuijk, A.; Darhuber, A. Dip-coating of chemically patterned surfaces. *Chemical Engineering and Processing: Process Intensification* **2011**, *50*, 565–568, DOI: 10.1016/j.cep.2010.09.021.
- [57] Lessel, M.; Bäumchen, O.; Klos, M.; Hähl, H.; Fetzer, R.; Paulus, M.; Seemann, R.; Jacobs, K. Self-assembled silane monolayers: an efficient step-by-step recipe for high-quality, low energy surfaces. *Surface and Interface Analysis* **2015**, *47*, 557–564, DOI: 10.1002/sia.5729.
- [58] Mayer, T. M.; de Boer, M. P.; Shinn, N. D.; Clews, P. J.; Michalske, T. a. Chemical vapor deposition of fluoroalkylsilane monolayer films for adhesion control in microelectromechanical systems. *Journal of Vacuum Science & Technology B: Microelectronics and Nanometer Structures* **2000**, *18*, 2433, DOI: 10.1116/1.1288200.
- [59] Psarski, M.; Celichowski, G.; Bystrzycka, E.; Pawlak, D.; Grobelny, J.; Cichomski, M. Vapor phase deposition of fluoroalkyl trichlorosilanes on silicon and glass: Influence of deposition conditions and chain length on wettability and adhesion forces. *Materials Chemistry and Physics* **2018**, *204*, 305–314, DOI: 10.1016/j.matchemphys.2017.10.037.
- [60] Völklein, F.; Zetterer, T., *Praxiswissen Mikrosystemtechnik*; Vieweg+Teubner: Wiesbaden, 2006, DOI: 10.1007/978-3-8348-9105-1.
- [61] Bigelow, W.; Pickett, D.; Zisman, W. Oleophobic monolayers: I. Films adsorbed from solution in non-polar liquids. *Journal of Colloid Science* **1946**, *1*, 513–538, DOI: 10.1016/0095-8522(46)90059-1.
- [62] Zisman, W. A. Surface Chemistry of Plastics Reinforced by Strong Fibers. *Industrial & Engineering Chemistry Product Research and Development* **1969**, *8*, 98–111, DOI: 10.1021/i360030a002.
- [63] Lee, L.-H. Wettability and conformation of reactive polysiloxanes. *Journal of Colloid and Interface Science* **1968**, *27*, 751–760, DOI: 10.1016/0021-9797(68)90109-4.
- [64] Kahn, F.; Taylor, G.; Schonhorn, H. Surface-produced alignment of liquid crystals. *Proceedings of the IEEE* **1973**, *61*, 823–828, DOI: 10.1109/PROC.1973.9171.
- [65] Tada, H.; Nagayama, H. Chemical Vapor Surface Modification of Porous Glass with Fluoroalkyl-Functional Silanes. 1. Characterization of the Molecular Layer. *Langmuir* **1994**, *10*, 1472–1476, DOI: 10.1021/la00017a025.
- [66] Tada, H.; Nagayama, H. Chemical Vapor Surface Modification of Porous Glass with Fluoroalkyl-Functionalized Silanes. 2. Resistance to Water. *Langmuir* **1995**, *11*, 136–142, DOI: 10.1021/la00001a025.

- [67] Fadeev, A. Y.; McCarthy, T. J. Self-Assembly Is Not the Only Reaction Possible between Alkyltrichlorosilanes and Surfaces: Monomolecular and Oligomeric Covalently Attached Layers of Dichloro- and Trichloroalkylsilanes on Silicon. *Langmuir* **2000**, *16*, 7268–7274, DOI: 10.1021/1a000471z.
- [68] Kobrin, B.; Zhang, T.; Grimes, M. T.; Chong, K.; Wanebo, M.; Chinn, J.; Nowak, R. An Improved Chemical Resistance and Mechanical Durability of Hydrophobic FDTS Coatings. *Journal of Physics: Conference Series* **2006**, *34*, 454–457, DOI: 10.1088/1742-6596/34/1/074.
- [69] Bhushan, B.; Cichomski, M. Nanotribological characterization of vapor phase deposited fluorosilane self-assembled monolayers deposited on polydimethylsiloxane surfaces for biomedical micro-/nanodevices. *Journal of Vacuum Science & Technology A: Vacuum, Surfaces, and Films* **2007**, *25*, 1285–1293, DOI: 10.1116/1.2426979.
- [70] Wang, Y.; Lieberman, M. Growth of Ultrasooth Octadecyltrichlorosilane Self-Assembled Monolayers on SiO₂. *Langmuir* **2003**, *19*, 1159–1167, DOI: 10.1021/1a020697x.
- [71] *Handbook of Ellipsometry*; Tompkins, H. G., Irene, E. A., Eds.; William Andrew Publishing: Norwich, NY, 2005, DOI: 10.1016/B978-0-8155-1499-2.50016-2.
- [72] ThermoFisher Product Specification Sheet 1H,1H,2H,2H-Perfluorodecyltrichlorosilane, 2020.
- [73] Schlesinger, I.; Sivan, U. New Information on the Hydrophobic Interaction Revealed by Frequency Modulation AFM. *Langmuir* **2017**, *33*, 2485–2496, DOI: 10.1021/acs.langmuir.6b03574.
- [74] Maboudian, R.; Ashurst, W.; Carraro, C. Self-assembled monolayers as anti-stiction coatings for MEMS: characteristics and recent developments. *Sensors and Actuators A: Physical* **2000**, *82*, 219–223, DOI: 10.1016/S0924-4247(99)00337-4.
- [75] Hartmann, M.; Hardt, S. Stability of Evaporating Droplets on Chemically Patterned Surfaces. *Langmuir* **2019**, *35*, 4868–4875, DOI: 10.1021/acs.langmuir.9b00172.
- [76] Bourges-Monnier, C.; Shanahan, M. E. R. Influence of Evaporation on Contact Angle. *Langmuir* **1995**, *11*, 2820–2829, DOI: 10.1021/1a00007a076.
- [77] Kim, J. H.; Ahn, S. I.; Kim, J. H.; Zin, W. C. Evaporation of water droplets on polymer surfaces. *Langmuir* **2007**, *23*, 6163–6169, DOI: 10.1021/1a0636309.
- [78] Bormashenko, E.; Bormashenko, Y.; Whyman, G.; Pogreb, R.; Musin, A.; Jager, R.; Barkay, Z. Contact Angle Hysteresis on Polymer Substrates Established with Various Experimental Techniques, Its Interpretation, and Quantitative Characterization. *Langmuir* **2008**, *24*, 4020–4025, DOI: 10.1021/1a703875b.
- [79] Cazabat, A.-M.; Guéna, G. Evaporation of macroscopic sessile droplets. *Soft Matter* **2010**, *6*, 2591–2612, DOI: 10.1039/b924477h.
- [80] Park, J. K.; Ryu, J.; Koo, B. C.; Lee, S.; Kang, K. H. How the change of contact angle occurs for an evaporating droplet: effect of impurity and attached water films. *Soft Matter* **2012**, *8*, 11889, DOI: 10.1039/c2sm26559a.
- [81] Zhang, X.; Shi, F.; Niu, J.; Jiang, Y.; Wang, Z. Superhydrophobic surfaces: from structural control to functional application. *J. Mater. Chem.* **2008**, *18*, 621–633, DOI: 10.1039/B711226B.
- [82] Simpson, J. T.; Hunter, S. R.; Aytug, T. Superhydrophobic materials and coatings: A review. *Reports on Progress in Physics* **2015**, *78*, DOI: 10.1088/0034-4885/78/8/086501.
- [83] Wong, T.-S.; Kang, S. H.; Tang, S. K. Y.; Smythe, E. J.; Hatton, B. D.; Grinthal, A.; Aizenberg, J. Bioinspired self-repairing slippery surfaces with pressure-stable omniphobicity. *Nature* **2011**, *477*, 443–447, DOI: 10.1038/nature10447.

- [84] Smith, J. D.; Dhiman, R.; Anand, S.; Reza-Garduno, E.; Cohen, R. E.; McKinley, G. H.; Varanasi, K. K. Droplet mobility on lubricant-impregnated surfaces. *Soft Matter* **2013**, *9*, 1772–1780, DOI: 10.1039/C2SM27032C.
- [85] Li, J.; Ueda, E.; Paulssen, D.; Levkin, P. A. Slippery Lubricant-Infused Surfaces: Properties and Emerging Applications. *Advanced Functional Materials* **2019**, *29*, 1802317, DOI: 10.1002/adfm.201802317.
- [86] Eifert, A.; Paulssen, D.; Varanakkottu, S. N.; Baier, T.; Hardt, S. Simple Fabrication of Robust Water-Repellent Surfaces with Low Contact-Angle Hysteresis Based on Impregnation. *Advanced Materials Interfaces* **2014**, *1*, 1–5, DOI: 10.1002/admi.201300138.
- [87] Dai, X.; Sun, N.; Nielsen, S. O.; Stogin, B. B.; Wang, J.; Yang, S.; Wong, T.-S. Hydrophilic directional slippery rough surfaces for water harvesting. *Science Advances* **2018**, *4*, eaaq0919, DOI: 10.1126/sciadv.aaq0919.
- [88] Guo, L.; Tang, G. H. Dropwise condensation on bioinspired hydrophilic-slippery surface. *RSC Advances* **2018**, *8*, 39341–39351, DOI: 10.1039/C8RA08190E.
- [89] Günay, A. A.; Sett, S.; Ge, Q.; Zhang, T.; Miljkovic, N. Cloaking Dynamics on Lubricant-Infused Surfaces. *Advanced Materials Interfaces* **2020**, *7*, 2000983, DOI: 10.1002/admi.202000983.
- [90] Kaneko, S.; Urata, C.; Sato, T.; Hönes, R.; Hozumi, A. Smooth and Transparent Films Showing Paradoxical Surface Properties: The Lower the Static Contact Angle, the Better the Water Sliding Performance. *Langmuir* **2019**, *35*, 6822–6829, DOI: 10.1021/acs.langmuir.9b00206.
- [91] Song, D.; Song, B.; Hu, H.; Du, X.; Zhou, F. Selectively splitting a droplet using superhydrophobic stripes on hydrophilic surfaces. *Physical Chemistry Chemical Physics* **2015**, *17*, 13800–13803, DOI: 10.1039/C5CP01530H.
- [92] Zou, L.; Wang, H.; Zhu, X.; Ding, Y.; Chen, R.; Liao, Q. Droplet splitting on chemically striped surface. *Colloids and Surfaces A: Physicochemical and Engineering Aspects* **2018**, *537*, 139–148, DOI: 10.1016/j.colsurfa.2017.09.052.
- [93] Wang, Y.; Jian, M.; Liu, H.; Zhang, X. Anisotropic Wetting of Droplets on Stripe-Patterned Chemically Heterogeneous Surfaces: Effect of Length Ratio and Deposition Position. *Langmuir* **2019**, *35*, 4387–4396, DOI: 10.1021/acs.langmuir.8b02491.
- [94] Kuang, M.; Wang, L.; Song, Y. Controllable Printing Droplets for High-Resolution Patterns. *Advanced Materials* **2014**, *26*, 6950–6958, DOI: 10.1002/adma.201305416.
- [95] Ko, S. H.; Chung, J.; Pan, H.; Grigoropoulos, C. P.; Poulikakos, D. Fabrication of multilayer passive and active electric components on polymer using inkjet printing and low temperature laser processing. *Sensors and Actuators, A: Physical* **2007**, *134*, 161–168, DOI: 10.1016/j.sna.2006.04.036.
- [96] McKerricher, G.; Vaseem, M.; Shamim, A. Fully inkjet-printed microwave passive electronics. *Microsystems & Nanoengineering* **2017**, *3*, 16075, DOI: 10.1038/micronano.2016.75.
- [97] Correia, V.; Mitra, K.; Castro, H.; Rocha, J.; Sowade, E.; Baumann, R.; Lanceros-Mendez, S. Design and fabrication of multilayer inkjet-printed passive components for printed electronics circuit development. *Journal of Manufacturing Processes* **2018**, *31*, 364–371, DOI: 10.1016/j.jmapro.2017.11.016.
- [98] Jung, S.; Sou, A.; Banger, K.; Ko, D.-H.; Chow, P. C. Y.; McNeill, C. R.; Siringhaus, H. All-Inkjet-Printed, All-Air-Processed Solar Cells. *Advanced Energy Materials* **2014**, *4*, 1400432, DOI: 10.1002/aenm.201400432.

- [99] Sukeshini, M. A.; Cummins, R.; Reitz, T. L.; Miller, R. M. Ink-jet printing: A versatile method for multilayer solid oxide fuel cells fabrication. *Journal of the American Ceramic Society* **2009**, *92*, 2913–2919, DOI: 10.1111/j.1551-2916.2009.03349.x.
- [100] Xia, D.; Johnson, L. M.; López, G. P. Anisotropic Wetting Surfaces with One-Dimensional and Directional Structures: Fabrication Approaches, Wetting Properties and Potential Applications. *Advanced Materials* **2012**, *24*, 1287–1302, DOI: 10.1002/adma.201104618.
- [101] Cassie, A. B. D.; Baxter, S. Wettability of porous surfaces. *Transactions of the Faraday Society* **1944**, *40*, 546–551, DOI: 10.1039/tf9444000546.
- [102] Jansen, H. P.; Sotthewes, K.; van Swigchem, J.; Zandvliet, H. J. W.; Kooij, E. S. Lattice Boltzmann modeling of directional wetting: Comparing simulations to experiments. *Physical Review E* **2013**, *88*, 013008, DOI: 10.1103/PhysRevE.88.013008.
- [103] Zhang, J.; Müller-Plathe, F.; Leroy, F. Pinning of the Contact Line during Evaporation on Heterogeneous Surfaces: Slowdown or Temporary Immobilization? Insights from a Nanoscale Study. *Langmuir* **2015**, *31*, 7544–7552, DOI: 10.1021/acs.langmuir.5b01097.
- [104] Ledesma-Aguilar, R.; Vella, D.; Yeomans, J. M. Lattice-Boltzmann simulations of droplet evaporation. *Soft Matter* **2014**, *10*, 8267–8275, DOI: 10.1039/C4SM01291G.
- [105] Li, Q.; Zhou, P.; Yan, H. J. Pinning–Depinning Mechanism of the Contact Line during Evaporation on Chemically Patterned Surfaces: A Lattice Boltzmann Study. *Langmuir* **2016**, *32*, 9389–9396, DOI: 10.1021/acs.langmuir.6b01490.
- [106] Patrick Jansen, H.; Sotthewes, K.; Zandvliet, H. J.; Kooij, E. S. Potential of lattice Boltzmann to model droplets on chemically stripe-patterned substrates. *Applied Surface Science* **2016**, *361*, 122–132, DOI: 10.1016/j.apsusc.2015.11.120.
- [107] Yu, Y.; Li, Q.; Zhou, C. Q.; Zhou, P.; Yan, H. Investigation of droplet evaporation on heterogeneous surfaces using a three-dimensional thermal multiphase lattice Boltzmann model. *Applied Thermal Engineering* **2017**, *127*, 1346–1354, DOI: 10.1016/j.applthermaleng.2017.08.158.
- [108] He, L.; Sui, X.; Liang, W.; Wang, Z.; Akbarzadeh, A. Numerical analysis of anisotropic wetting of chemically striped surfaces. *RSC Advances* **2018**, *8*, 31735–31744, DOI: 10.1039/C8RA06626D.
- [109] Léopoldès, J.; Dupuis, A.; Bucknall, D. G.; Yeomans, J. M. Jetting Micron-Scale Droplets onto Chemically Heterogeneous Surfaces. *Langmuir* **2003**, *19*, 9818–9822, DOI: 10.1021/la0353069.
- [110] Quéré, D. Rough ideas on wetting. *Physica A: Statistical Mechanics and its Applications* **2002**, *313*, 32–46, DOI: 10.1016/S0378-4371(02)01033-6.
- [111] Shafrin, E. G.; Zisman, W. A. In *Contact Angle, Wettability, and Adhesion*, Fowkes, F. M., Ed., Advances in American Chemical Society: 1964; Chapter 9, pp 145–157, DOI: 10.1021/ba-1964-0043.ch009.
- [112] Langbein, D.; Ruschak, K., *Capillary Surfaces*; Langbein, D., Ed.; Springer Tracts in Modern Physics 1, Vol. 178; Springer Berlin Heidelberg: Berlin, Heidelberg, 2002, DOI: 10.1007/3-540-45267-2.
- [113] Bostwick, J.; Steen, P. Stability of Constrained Capillary Surfaces. *Annual Review of Fluid Mechanics* **2015**, *47*, 539–568, DOI: 10.1146/annurev-fluid-010814-013626.
- [114] Hartmann, M.; Fricke, M.; Weimar, L.; Gründing, D.; Marić, T.; Bothe, D.; Hardt, S. Breakup Dynamics of Capillary Bridges on Hydrophobic Stripes. *arXiv* **2020**, Eprint: <http://arxiv.org/abs/1910.01887v2>.
- [115] Li, Y.; Sprittles, J. E. Capillary breakup of a liquid bridge: identifying regimes and transitions. *Journal of Fluid Mechanics* **2016**, *797*, 29–59, DOI: 10.1017/jfm.2016.276.

- [116] CHEN, Y.-J.; STEEN, P. H. Dynamics of inviscid capillary breakup: collapse and pinchoff of a film bridge. *Journal of Fluid Mechanics* **1997**, *341*, 245–267, DOI: 10.1017/S002211209700548X.
- [117] Eggers, J.; Fontelos, M. A., *Singularities: Formation, Structure, and Propagation*; Cambridge University Press: Cambridge, 2015, DOI: 10.1017/CB09781316161692.
- [118] Deblais, A.; Herrada, M. A.; Hauner, I.; Velikov, K. P.; van Roon, T.; Kellay, H.; Eggers, J.; Bonn, D. Viscous Effects on Inertial Drop Formation. *Physical Review Letters* **2018**, *121*, 254501, DOI: 10.1103/PhysRevLett.121.254501.
- [119] Bostwick, J. B.; Steen, P. H. Static rivulet instabilities: Varicose and sinuous modes. *Journal of Fluid Mechanics* **2018**, *837*, 819–838, DOI: 10.1017/jfm.2017.876.
- [120] Davis, S. H. Moving contact lines and rivulet instabilities. Part 1. The static rivulet. *Journal of Fluid Mechanics* **1980**, *98*, 225–242, DOI: 10.1017/S0022112080000110.
- [121] Dzedzic, A.; Nakrani, M.; Ezra, B.; Syed, M.; Popinet, S.; Afkhami, S. Breakup of finite-size liquid filaments: Transition from no-breakup to breakup including substrate effects. *The European Physical Journal E* **2019**, *42*, 18, DOI: 10.1140/epje/i2019-11785-y.
- [122] Brinkmann, M.; Kierfeld, J.; Lipowsky, R. Stability of liquid channels or filaments in the presence of line tension. *Journal of Physics: Condensed Matter* **2005**, *17*, 2349–2364, DOI: 10.1088/0953-8984/17/15/008.
- [123] Speth, R. L.; Lauga, E. Capillary instability on a hydrophilic stripe. *New Journal of Physics* **2009**, *11*, DOI: 10.1088/1367-2630/11/7/075024.
- [124] Li, Y.; Lv, P.; Diddens, C.; Tan, H.; Wijshoff, H.; Versluis, M.; Lohse, D. Evaporation-Triggered Segregation of Sessile Binary Droplets. *Physical Review Letters* **2018**, *120*, 224501, DOI: 10.1103/PhysRevLett.120.224501.
- [125] Fricke, M. Mathematical modeling and Volume-of-Fluid based simulation of dynamic wetting, Ph.D. Thesis, TU Darmstadt, 2020, DOI: 10.12921/tuprints-00014274.
- [126] Savitzky, A.; Golay, M. J. E. Smoothing and Differentiation of Data by Simplified Least Squares Procedures. *Analytical Chemistry* **1964**, *36*, 1627–1639, DOI: 10.1021/ac60214a047.
- [127] Virtanen, P. et al. SciPy 1.0: fundamental algorithms for scientific computing in Python. *Nature Methods* **2020**, *17*, 261–272, DOI: 10.1038/s41592-019-0686-2.
- [128] Rieber, M., *Numerische Modellierung der Dynamik freier Grenzflächen in Zweiphasenströmungen*; Fortschritt-Berichte VDI: Reihe 7, Strömungstechnik; VDI-Verlag: 2004.
- [129] Tolle, T.; Marić, T.; Gründing, D.; Bothe, D. Computing volume fractions by intersecting unstructured meshes. *in preparation* **2020**.
- [130] Fricke, M.; Marić, T.; Bothe, D. Contact Line Advection using the Level Set Method. *PAMM* **2019**, *19*, 10–11, DOI: 10.1002/pamm.201900476.
- [131] Self, E. C.; Naguib, M.; Ruther, R. E.; McRen, E. C.; Wycisk, R.; Liu, G.; Nanda, J.; Pintauro, P. N. High Areal Capacity Si/LiCoO₂ Batteries from Electrospun Composite Fiber Mats. *ChemSusChem* **2017**, *10*, 1823–1831, DOI: 10.1002/cssc.201700096.
- [132] Du, J.; Wang, J.-H.; Yu, H.-Y.; Zhang, Y.-Y.; Pu, L.-H.; Wang, J.-C.; Lu, S.-Y.; Chen, S.-H.; Zhu, T.-H. Electrospun Poly(p-dioxanone)/Poly(ester-urethane)ureas Composite Nanofibers for Potential Heart Valve Tissue Reconstruction. *Chinese Journal of Polymer Science* **2019**, *37*, 560–569, DOI: 10.1007/s10118-019-2231-2.

- [133] Liu, W.; Thomopoulos, S.; Xia, Y. Electrospun Nanofibers for Regenerative Medicine. *Advanced Healthcare Materials* **2012**, *1*, 10–25, DOI: 10.1002/adhm.201100021.
- [134] Xue, J.; Wu, T.; Dai, Y.; Xia, Y. Electrospinning and electrospun nanofibers: Methods, materials, and applications. *Chemical Reviews* **2019**, *119*, 5298–5415, DOI: 10.1021/acs.chemrev.8b00593.
- [135] Yarin, A. L.; Koombhongse, S.; Reneker, D. H. Taylor cone and jetting from liquid droplets in electrospinning of nanofibers. *Journal of Applied Physics* **2001**, *90*, 4836–4846, DOI: 10.1063/1.1408260.
- [136] Liu, Z.; Chan, S. T.; Faizi, H. A.; Roberts, R. C.; Shum, H. C. Droplet-based electro-coalescence for probing threshold disjoining pressure. *Lab on a Chip* **2015**, *15*, 2018–2024, DOI: 10.1039/C5LC00177C.
- [137] Huang, X.; He, L.; Luo, X.; Xu, K.; Lü, Y.; Yang, D. Coalescence, Partial Coalescence, and Noncoalescence of Two Free Droplets Suspended in Low-Viscosity Oil under a DC Electric Field. *The Journal of Physical Chemistry B* **2020**, *124*, 7508–7517, DOI: 10.1021/acs.jpcc.0c05371.
- [138] Wang, J.; Wang, B.; Qiu, H. Coalescence and breakup of oppositely charged droplets. *Scientific reports* **2014**, *4*, 7123, DOI: 10.1038/srep07123.
- [139] Xie, G.; He, F.; Liu, X.; Si, L.; Guo, D. Sessile multidroplets and salt droplets under high tangential electric fields. *Scientific Reports* **2016**, *6*, 25002, DOI: 10.1038/srep25002.
- [140] Ndoumbe, J.; Beroual, A.; Imano, A. M. Simulation and analysis of coalescence of water droplets on composite insulating surface under DC electric field. *IEEE Transactions on Dielectrics and Electrical Insulation* **2015**, *22*, 2669–2675, DOI: 10.1109/TDEI.2015.004820.
- [141] Le Grand, N.; Daerr, A.; Limat, L. Shape and motion of drops sliding down an inclined plane. *Journal of Fluid Mechanics* **2005**, *541*, 293–315, DOI: 10.1017/S0022112005006105.
- [142] Podgorski, T.; Flesselles, J. M.; Limat, L. Corners, cusps, and pearls in running drops. *Physical Review Letters* **2001**, *87*, 036102, DOI: 10.1103/PhysRevLett.87.036102.
- [143] Peters, I.; Snoeijer, J. H.; Daerr, A.; Limat, L. Coexistence of Two Singularities in Dewetting Flows: Regularizing the Corner Tip. *Physical Review Letters* **2009**, *103*, 114501, DOI: 10.1103/PhysRevLett.103.114501.
- [144] Popescu, M. N.; Oshanin, G.; Dietrich, S.; Cazabat, A.-M. Precursor films in wetting phenomena. *Journal of Physics: Condensed Matter* **2012**, *24*, 243102, DOI: 10.1088/0953-8984/24/24/243102.
- [145] Voinov, O. V. Hydrodynamics of wetting. *Fluid Dynamics* **1976**, *11*, 714–721, DOI: 10.1007/BF01012963.
- [146] Bonn, D.; Eggers, J.; Indekeu, J.; Meunier, J. Wetting and spreading. *Reviews of Modern Physics* **2009**, *81*, 739, DOI: 10.1103/RevModPhys.81.739.

